Numerical Simulation of Reacting Flows under Laminar Conditions with Detailed Chemistry

Vom Fachbereich Maschinenbau
an der Technischen Universität Darmstadt
zur
Erlangung des Grades eines Doktor-Ingenieurs (Dr.-Ing.)
genehmigte

D i s s e r t a t i o n

vorgelegt von

Dipl.-Ing. Jesús Contreras Espada

aus Librilla (Spanien)

Berichterstatter:	Prof. Dr.–Ing. J. Janicka
Mitberichterstatter:	Prof. Dr. rer. nat. M. Schäfer
Tag der Einreichung:	3. November 2009
Tag der mündlichen Prüfung:	8. Dezember 2009

Darmstadt 2010
D 17

Acknowledgements

Many people have helped me in the course of my research in writing this book, and any merit in it is in large measure due to them. First and foremost, I gladly acknowledge my debt to Prof. Dr.-Ing. Johannes Janicka of the Technical University of Darmstadt who invited me to become a member of his team and who was my teacher and supervisor in this work. I thank him for his excellent and tireless guidance, encouragement and patience throughout the years of the study. I also want to thank Prof. Amsini Sadiki for providing me assistance and good advice during all my years in Darmstadt, and for helping shape papers and presentations in so many occasions. I thank Dr. Andreas Dreizler for his remarks and helpful discussions.

To my colleagues, who made our department an ideal place to work at and who gave me all the explanations, suggestions and encouragement that I required from them, and even more: Rajani Kumar Akula, Mouldi Chrigui, Dmitry Goryntsev, Alex Maltsev, Bernhard Wegner, Erich Wachter, Zdravko Stojanovic, Andreas Kempf, Michael Düsing, Jan Brübach, Bern Groh, Frederik Hahn, Clemens Olbrich, Desislava Dimitrova, Elena and Christoph Schneider, Martin Freitag, Michael Hage, Ying Huai, Thomas Kania, Benjamin Bohm, Marc Aurel Gregor, Sunil Omar, Ranga Reddy Kottam, Andreas Nauert, Felix Flemming, Florian Seffrin, Dirk Geyer and Markus Klein, who first invited me to EKT in the name of Prof. Janicka.

Thanks to Petra Knop and Elizabeth Zweyrohn for their everyday help. They made my work easier because I could concentrate on it while they were worrying about everything else.

And outside our institute, thanks to Takeshi Omori, Miklos Kanzamar, Kristjan Horvat, Christof Sodtke and Sanjin Saric for their friendship and encouragement. Thanks to Prof. Markov and Ricard Consul for helping fill my gaps in combustion modeling and numerical methods, and thanks to Ursula Kleinschmidt and Monika Thom who helped me with my language skills.

The thesis was mostly written within the framework of the Graduiertenkolleg 'Modellierung und numerische Beschreibung technischer Strömungen'. The graduate program was generously financed by the Deutsche Forschungsgemeinschaft.

And finally and most especially I would like to thank my parents, who made a great effort to provide me with advantages they never had, I offer my deepest appreciation and gratitude.

I declare that this thesis does not incorporate without acknowledgement any material previously submitted for a degree or diploma in any university and that to the best of my knowledge it does not contain any materials previously published or written by another person except where due reference is made in the text.

Jesus Contreras Espada Basel, 17 November 2010

Contents

Nomenclature

A	Area (m^2)
ϕ	Equivalence ratio (dimensionless)
Ω	Angular velocity; Ω_{ij}, Mean rate of rotation tensor (s^{-1})
$\vec{a}$	Acceleration (m/s^2)
a	Local speed of sound (m/s)
c	Concentration (mass/volume, moles/volume)
c_p, c_v	Heat capacity at constant pressure, volume (J/kg-K)
$\mathcal{D}_{ij}, D$	Mass diffusion coefficient (m^2/s)
E	Total energy, activation energy (J, kJ, cal)
$\vec{g}$	Gravitational acceleration (m/s^2)
H	Total enthalpy (energy/mass, energy/mole)
h	Heat transfer coefficient (W/m^2-K)
h	Species enthalpy (energy/mass, energy/mole)
h^0	Standard state enthalpy of formation (energy/mass, energy/mole)
J	Mass flux; diffusion flux (kg/m^2-s)
K	Equilibrium constant = forward rate constant/backward rate constant (units vary)
k	Reaction rate constant, e.g., k_1, k_{-1}, $k_{f,r}$, $k_{b,r}$ (units vary)
k_B	Boltzmann constant (1.38×10^{-23} J/molecule-K)
k, k_c	Mass transfer coefficient (units vary); also K, K_c
ℓ, l, L	Length scale (m)
Le	Lewis number
m	Mass (kg)
$\dot{m}$	Mass flow rate (kg/s)
M_w	Molecular weight (kg/kgmol)
M	Mach number
Nu	Nusselt number
p	Pressure (Pa)
Pe	Peclet number
Pr	Prandtl number
Q	Flow rate of enthalpy (W)
q	Heat flux (W/m^2)
R	Gas-law constant (8.31447×10^3 J/kgmol-K)
r	Radius (m)
r_f	Forward reaction rate (units vary)
r_r	Reverse reaction rate (units vary)
Ra	Rayleigh number
Re	Reynolds number
S	Total entropy (J/K, J/kgmol-K)
s	Species entropy; s^0, standard state entropy (J/kgmol-K)

Sc	Schmidt number
S_{ij}	Mean rate-of-strain tensor (s $^{-1}$)
T	Temperature (K)
t	Time (s)
u, v, w	Velocity magnitude (m/s)
V	Volume (m ^{3})
$\vec{v}$	Overall velocity vector (m/s)
X_k	Mole fraction
Y_k	Mass fraction

Greek letters

α	Thermal diffusivity (m ^{2}/s)
β	Coefficient of thermal expansion (K $^{-1}$)
γ	Ratio of specific heats, c $_p$/c $_v$
Δ	Change in variable, final $-$ initial
δ	Delta function (units vary)
ϵ	Lennard-Jones energy parameter (J/molecule)
ϵ	Turbulent dissipation rate (m ^{2}/s ^{3})
λ	Thermal conductivity (W/m-K)
μ	Dynamic viscosity (cP, Pa-s)
ν	Kinematic viscosity (m ^{2}/s)
ν', ν''	Stoichiometric coefficients for reactants, products
ρ	Density (kg/m ^{3})
σ	Stefan-Boltzmann constant (5.67×10^8 W/m ^{2}-K ^{4})
τ	Shear stress (Pa)
τ	Time scale

1. Introduction

1.1. Motivation and aim of the present work

Heterogeneous reactions are those in which two or more phases are involved. A large number of environmentally and technologically important processes are based on chemical reactions occurring at a surface. Heterogeneous catalysis, chemical vapor deposition, corrosion, adhesion, ozone depletion, electrochemistry: all of these phenomena have in common the fact that they require a chemically reactive surface and a flow that carries the reactants to the reacting zone. This flow corresponds, in many applications, to a gas mixture of different species.

For both economic and environmental reasons, constant improvement in design and optimization of processes has become more and more important over time. This improvement requires a detailed knowledge of the local flow behavior and the multiphase phenomena. Computational fluid dynamics and chemical kinetics can be interconnected to provide the required knowledge for the improvement of heterogeneous processes.

The aim of this project is the modelling and simulation of complex configurations presenting heterogeneous reactions. Due to the extensive scope of the subject, this work focuses on the chemical reactions in the gas phase. The implementation of a detailed chemistry algorithm in a 3D CFD-code has been achieved through the coupling of the CFD-code and a chemical kinetics solver, which provides the production/consumption rates of the species involved and the temperature changes in the control volumes, as well as some basic values in these types of simulations like transport coefficients or viscosity of the different species.

A Strang-like operator-splitting technique has been introduced in order to simplify the problem, reduce the computational time and avoid the drawbacks of source terms in the species and enthalpy equations. Two disadvantages, which are intrinsic to the method of operator-splitting, are the creation of discontinuities of the spatial concentration distribution at the beginning of each 'chemical' time step and splitting errors, which add up to the discretization errors and other errors due to the numerical solution method.

One of the biggest advantages of this procedure is, that it allows the simulation of any kind of reacting flow without having to perform big changes in the code. This high flexibility is achieved through the separation of the flow and chemistry solvers. In addition, it provides information about all involved species or, at least, those present in the input

chemical mechanism. Another advantage of this procedure is the possibility of applying it to turbulent flows, multiphase and many other more complex configurations.

1.2. Combustion research

Combustion is nowadays the most important form of energy conversion. It is used in numerous practical applications in order to generate heat (industrial and house burners), electricity (heat power plants, gas turbines), for transport purposes (motors, turbines, reactors) and the destruction of waste (incinerating plants). Combustion is characterized by the development of strongly exothermic irreversible chemical reactions between a fuel and a comburent according to the following global reaction:

$$Fuel + Oxidizer \rightarrow Products + Heat$$

The heat release takes place generally in a very thin zone called the *flame front* (typical values of this front are in the range of one millimeter or tenth of millimeter), which can introduce extremely high temperature and mass gradients and strong variations of the density in very small scales. In contrast to this, fuel cells convert the chemical energy of an oxidation process, known as "cold combustion" [29], directly into electrical energy with lower emissions and higher efficiency than internal combustion engines [76]. The maximum membrane temperature for a LTFC (low temperature fuel cell) is approximately $80°C$ [9]. A large variety of fuels, gas, liquid or solid, can be used: coal, wood, carbohydrates (methane, butane, propane, gasoline, gasoil, kerosene...), hydrogen, ... The oxidizer is generally air oxygen or, occasionally, pure oxygen (certain industrial furnaces, rocket motors) that allows higher temperatures and avoids the storage and manipulation of nitrogen.

Combustion is a combination of several complex, interconnected processes. The kinetic schemes determine the fuel consumption rate and the formation of products and pollutants. They are also important in the processes of ignition and extinction of the flames. The mass transfer of chemical species through molecular diffusion or convective transport is another very important element of the combustion process. The heat release due to chemical reactions introduces intense heat transfer through conduction, convection and radiation inside the flow where combustion takes place, but also in the environment (burner walls, etc...). This thermal energy must be immediately used either directly or after conversion into mechanical energy in gas turbines or piston engines. The description of the flow is required in gas combustion. In other systems there are additional processes that have to be taken into account: two (liquid fuel) or three (solid fuel particles) phases can be involved in the combustion process, phenomena like vaporization, drop combustion, etc. must be taken into account, soot formation is a very difficult problem which includes, generation, growth, aggregation of small carbon particles which are transported in the flow and consumed downstream.

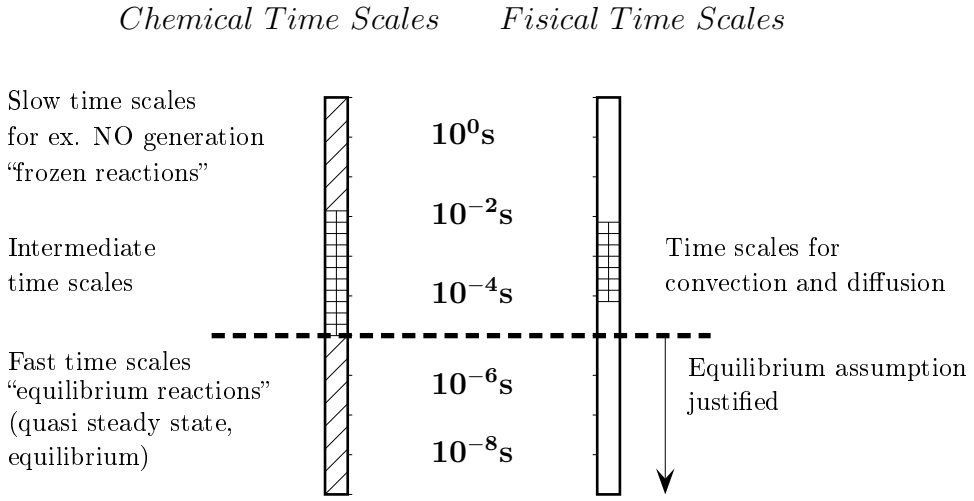

Figure 1.1.: (From Warnatz [98]) Comparison of chemical and mechanical scales involved in the combustion process

One of the main difficulties in the numerical simulation of combustion, apart from the complexity of the phenomena involved, lies in the big range of time and length scales corresponding to the different processes (see fig. 1.1). Certain chemical reactions can take place in very small domains (hundredths of millimeter) and very short periods of time (10^{-6} to 10^{-10} seconds) while the burner can be several meters long (industrial furnaces) and the residence times can be up to ten seconds or even longer. The prediction of pollutants requires the estimation of chemical species present in part per million (ppm), facing the main species (oxygen, nitrogen, fuel, water vapor, carbon dioxide...) where the concentration is more than thousand times higher.

The objective of research in combustion is to achieve a better understanding of the complex phenomena involved, in order to be able to model and reproduce these phenomena. One of the final goals is the numerical simulation of industrial systems or real configurations. The development costs associated with a new prototype can be reduced if numerical simulation can be used to optimize the burner before its construction. This optimization can be done according to different criteria: efficiency, pollutants, etc. It can also help to avoid instabilities in the combustion. In addition to better understanding of the mechanisms, these calculations allow the formation of databases used as models for turbulent flows.

Numerous studies are related to the reduction of reaction schemes by identification (by hand or through sensibility analysis) of the limiting stages. The goal is the generation of schemes which can be used in practical applications or in turbulent flows. The accurate validation of these schemes requires a comparison with the detailed ones. The automatic reduction of chemical mechanisms is nowadays a growing field of research.

Detailed simulations describe as precisely as possible the complexity of the kinetic schemes and transport phenomena. The combustion of common carbohydrates in air comprises many hundreds of species and some thousand elemental chemical reactions. The first step is to identify these reactions and the corresponding reaction rates. These schemes (chemical mechanisms) are incorporated in the simulation of reacting flows by means of chemical pre-processors. The reaction rates introduce numerical stiffness and highly non-linearity as they follow the Arrhenius law, which includes an exponential factor.

Although the speed and storage capacity of modern computers increases continuously, these detailed schemes are not yet suitable in most cases for turbulent flows because of their computational cost and the complexity of modelling the turbulence-chemistry interaction. This is the reason why these simulations are usually performed for laminar flows in simple configurations.

1.3. Literature overview

Multiple studies in the past few decades have been presented concerning detailed experimental and numerical analysis of laminar flames in simple configurations. In particular, the analysis of co-flow laminar flames has motivated a great interest due to their wide application in household and industrial heating systems. More recently these studies have been extended to partially premixed flames ([62] and [6]) due to their practical and fundamental importance. Because of their stability, partially premixed flames are used in Bunsen burners, furnaces, gas-turbine combustor flames, gas-fired domestic appliances, and other common combustion devices. Recent studies suggest that optimum operating conditions exist, which minimise the pollutant emissions and, thus, enhance the design of cleaner burning combustors.

With increases in computational power, improvement of numerical methods and use of more accurate experimental techniques, knowledge of the combustion phenomenon taking place in these flames has been considerably increased.

Experimental studies have provided measurements of temperature, major species, radicals, nitrogen oxides and soot. Mass spectrometry, Raman and LIF techniques have been employed to study co-flow flames under different geometrical configurations, equivalence ratios, and pressure-conditions ([62] and [85]).

Concerning numerical studies, from one of the first multidimensional simulations of co-flow methane-air laminar flames carried out by Mitchell et al [56], a considerable improvement of the accuracy of the mathematical models employed for the simulations has been achieved. Detailed numerical simulations with fully elliptic equations, complex transport formulation and detailed chemistry have been reported. C1 and C2 chemical mechanisms are mainly employed and compared [44], molecular transport is modelized under different assumptions [45], soot formation is sometimes modelled [84], and radiation transfer, if considered, is

usually evaluated with simplified models [7].

1.4. Codes used in this work

1.4.1. The FASTEST-3D code

The numerical simulations presented in this thesis have been performed with the code FASTEST-3D (Flow Analysis by Solving Transport Equation Simulating Turbulence) [20], a CFD tool developed by the Institute for Fluid Mechanics, University of Erlangen and the Department of Numerical Methods in Mechanical Engineering at Darmstadt University of Technology. The numerical scheme adopted in FASTEST to solve the incompressible Navier Stokes equations formulated in cartesian coordinates is based on a procedure described by Perić [20], consisting of a fully conservative second-order finite volume space discretization with a collocated arrangement of variables on structural, non-orthogonal, multiblock grids. A pressure correction method of the SIMPLE algorithm with Rhie and Chow [80] pressure-weighted interpolation for the iterative coupling of velocity and pressure is used, as well as an iterative ILU decomposition method by Stone for the solution of the sparse linear systems for velocity components, pressure correction and temperature. All these features will be explained in the following sections.

1.4.2. The CHEMKIN-Package

1.4.2.1. CHEMKIN (Kee, Rupley and Miller, 1989)

CHEMKIN [46] is a software package whose purpose is to facilitate the formation, solution, and interpretation of problems involving elementary gas-phase chemical kinetics. It constitutes an especially flexible and powerful tool for incorporating complex chemical kinetics into simulations of fluid dynamics. The package consists of two major software components: an Interpreter and a Gas-Phase Subroutine Library. The Interpreter is a program that reads a symbolic description of an elementary, user-specified chemical reaction mechanism. One output from the Interpreter is a data file that forms a link to the Gas-Phase Subroutine Library. This library is a collection of about one hundred highly modular Fortran subroutines that may be called to return information on equation of state, thermodynamic properties, and chemical production rates.

1.4.2.2. SENKIN (Lutz, Kee and Miller, 1988)

SENKIN [50] is a Fortran computer program that calculates the temporal evolution of a homogeneous reacting gas mixture in a closed system. The model accounts for finite-rate

elementary chemical reactions, and performs kinetic sensitivity analysis with respect to the reaction rates. The program considers five problem types:

1. Adiabatic system with constant pressure
2. Adiabatic system with constant volume
3. Adiabatic system where the volume is a specified function of time
4. System where the pressure and temperature are constant
5. System where the pressure is constant and the temperature is a specified function of time.

The program uses the differential equation system solver DASSAC ([10] and [11]) to solve both the nonlinear ordinary differential equations that describe the temperature and species mass fractions and the set of linear differential equations that describe the first-order sensitivity coefficients of temperature and species composition with respect to the individual reaction rates. The program runs in conjunction with the CHEMKIN package, which provides the coefficients and source terms for the equation system and serves as the user interface.

1.4.2.3. PSR (Glarborg et al., 1986)

PSR [32] is a Fortran computer program that predicts the steady-state temperature and species composition in a perfectly stirred reactor (PSR). These reactors are characterized by a reactor volume, residence time or mass flow rate, heat loss or temperature, and the incoming temperature and mixing composition. The model accounts for finite-rate elementary chemical reactions. The governing equations are a system of nonlinear algebraic equations. The program solves these equations using a hybrid Newton/time-integration method. In cases where the Newton method has convergence difficulties, a time integration of the related transient problem helps to bring the trial solution into Newton's domain of convergence. The program runs in conjunction with the CHEMKIN package, which handles the chemical reaction mechanism.

Basic inputs to the SENKIN and the PSR computer programs for the cases under study are fuel composition, temperature, residence time and pressure. The PSR configurations are treated as a system where enthalpy and pressure remain constant during the combustion process. Since a set of algebraic equations is solved for the PSR, starting estimates for the solution must be given. Included in the PSR program is an option to use a modified version of the STANJAN subroutine package [78] to provide equilibrium compositions as initial solution estimates, or to use previously calculated results as initial solution estimates.

In this work we have considered an adiabatic system with constant pressure (problem type 1). The reacting mixture is treated as a closed system with no mass crossing the

boundary, so that the total mass of the mixture is constant. In the adiabatic case, since the temperature is known, the energy equation is unnecessary and the problem is completely defined by the mass conservation equations. The SENKIN tool is able to treat one case at a time and all input must be introduced manually.

The SENKIN and PSR tools treat ideal flow models in combination with chemical kinetics. The calculation process itself does not introduce significant error sources. However, the assumption of ideal flow models, the choice of thermodynamic and kinetic data and the fuel composition used, may all influence the discrepancy between calculated and experimental results. The use of ideal flow models is necessary due to limitations in the processing capacity of today's computers. Thermodynamic and kinetic data used are as up-to-date as possible. The fuel composition used is based on the examples found in the literature and experimental conditions.

1.4.3. The FLUENT code

FLUENT is one of the many commercial packages available for CFD. It is also the most widely used general-purpose CFD software to perform fluid flow and heat transfer analysis of real industrial processes. It uses the finite-volume method to solve the governing equations of the flow. It provides the capability to use different physical models such as incompressible or compressible, inviscid or viscous, laminar or turbulent, etc. Supported mesh types include 2D triangular/quadrilateral, 3D tetrahedral/hexahedral/pyramid/wedge, and mixed (hybrid) meshes. Of interest in the present study is the capability of FLUENT to simulate chemically reacting flows under laminar conditions using a stiff chemistry solver and a CHEMKIN mechanisms as input. The combustion models available in the code include:

- The generalized finite rate chemistry for N reactions (forward/backward) with:
  - Arrhenius model
  - Eddy-breakup (EBU) model
  - Combined Arrhenius/eddy-breakup model
  - Eddy dissipation concept (EDC)
- Conserved scalar
- Probability density function (PDF) based formulation for diffusion-controlled (non-premixed) reactions (one or two mixture fractions) using:
  - Mixed-is-burned model
  - Chemical equilibrium
  - Laminar flamelet model

- A turbulent premixed combustion model based on a turbulent flame speed closure model
- A partially premixed turbulent combustion model
- Subgrid scale combustion models for large eddy simulations (LES),
- Laminar stiff chemistry option for coupled solver (used in the present work)
- Combustion submodels for coal, liquid, gas, and mixed fuel types
- Pollutant formation models (NO_X, Soot,...)
- Multi-step surface reactions with multiple sites and site species
- User-defined access to reaction rates and source/sink terms
- Import of reaction mechanisms in Chemkin format
- Several radiation models

Chemical mechanisms in CHEMKIN format can be read in FLUENT and used to determine the chemical source terms of the different species reacting in the flow. After reading the mechanism and, eventually, the transport and thermodynamic properties files in FLUENT, the user must select the species transport model and the volumetric reactions option. The 6.2 version of FLUENT has been expanded with a very efficient laminar stiff chemistry solver which applies a fractional step algorithm. In the first fractional step, the chemistry in each cell is computed for reaction at constant pressure for the flow time-step, using the ISAT integrator. In the second fractional step, the convection and diffusion terms are treated just as in a non-reacting simulation.

1.5. Content description

This thesis is divided into five chapters. The first of them is a brief introduction of the work, the state of the art and the tools involved. The second chapter deals with the physical and chemical fundamentals. The basic flow equations for reactive mixtures and transport properties for multi-component mixtures will be introduced, followed by a brief presentation of some general aspects of chemical reactions and numerical methods. The operator-splitting technique is explained as well in this chapter. Chapter 3 shows the results of the one-dimensional simulations for the CFD-solver and the chemical kinetics package for different mechanisms and parameters like grid-spacing, *Courant* number or temporal discretization. Chapter 4 deals with two dimensional simulations for the simpler case of constant density. Several configurations have been computed in order to achieve qualitative information about

the combustion process. The simulation of one case of laminar flame with variable density is presented at the end of this chapter. The verification of the results has been done by means of the CFD-Code FLUENT. In chapter 5, finally, a general discussion of the results and a short conclusion of this work is given.

2. Fundamentals

2.1. The Navier-Stokes equations

To find out the solution of the velocity field and for computation of the convective and diffusive flows, the Navier-Stokes equations are solved in FASTEST. The Navier-Stokes equations are a set of vectorial, nonlinear, partial differential equations which, in the index notation according to the Einstein summation convention, present the following aspect:

$$\frac{\partial \rho}{\partial t} + \frac{\partial \rho U_j}{\partial x_j} = 0 \tag{2.1}$$

$$\frac{\partial (\rho U_i)}{\partial t} + \frac{\partial (\rho U_i U_j)}{\partial x_j} = -\frac{\partial P}{\partial x_i} - \frac{\partial \tau_{ij}}{\partial x_j} + \rho g_i \tag{2.2}$$

where:

$$\tau_{ij} = -\mu \left(\frac{\partial U_i}{\partial x_j} - \frac{\partial U_j}{\partial x_i} \right) \tag{2.3}$$

is the stress tensor. The second term in the right hand side of equation 2.2 describes the diffusive transport of momentum due to inner friction and the third term corresponds to the gravity force.

2.2. The energy equation

The equation that provides the temperature field is formulated in FASTEST as an enthalpy equation in the form:

$$\frac{\partial (\rho c_p T)}{\partial t} + \frac{\partial (\rho c_p U_i T)}{\partial x_i} = -\frac{\partial q_i}{\partial x_i} - \tau_{ij} \frac{\partial U_i}{\partial x_j} \tag{2.4}$$

The indexes i and j take the value of the three spatial directions $i = 1, 2, 3$ and of the components of the velocity vector $j = 1, 2, 3$ respectively.

The closure of the conservation equations is completed through two state equations, the caloric equation of state:

$$h = \sum_{i=1}^{N_s} Y_i h_i, \quad \text{with} \quad h_i = h_i^{ref} + \int_{T^{ref}}^{T} c_{pi}(T') dT' \tag{2.5}$$

where the enthalpy is defined as a function of the temperature T and species mass fractions, and the thermal equation of state, given by the ideal-gas-law:

$$p_k = \rho_k \frac{R}{W_k} T \tag{2.6}$$

where T is the temperature of the mixture, $R = 8.314 J/(moleK)$ is the perfect gas constant and where $\rho_k = \rho Y_k$, and W_k are the density and the atomic weight of species k respectively. For a mixture of N perfect gases, the total pressure is the sum of partial pressures:

$$p = \sum_{k=1}^{N} p_k \tag{2.7}$$

Since the density ρ of the mixture is $\rho = \sum_{k=1}^{N} \rho_k$ equation 2.6 can be written:

$$p = \rho \frac{R}{W} T \tag{2.8}$$

where W is the mean molecular weight of the mixture given by

$$\frac{1}{W} = \sum_{k=1}^{N} \frac{Y_k}{W_k} \tag{2.9}$$

The approximation of ideal gas can be used in most combustion problems as the mixture behaves like an ideal gas and the error introduced by this equation is negligible.

In equation 2.5 the reference enthalpies h_i^{ref} are obtained from thermodynamic tables. The enthalpy of the mixture can also be obtained from:

$$h = h^{ref} + \int_{T^{ref}}^{T} c_p(T')dT' \tag{2.10}$$

where h^{ref} is the enthalpy of the mixture at the reference temperature:

$$h^{ref} = \sum_{k=1}^{K} Y_k {h^{ref}}_k \tag{2.11}$$

and c_p is the mean specific heat of the mixture:

$$c_p = \sum_{k=1}^{K} Y_k c_{pk} \tag{2.12}$$

2.3. The species transport equations

The conservation of the chemical species is given by the transport equation for the mass fraction $Y_k = \rho_k/\rho$, where ρ_k represents the density of the species k:

$$\frac{\partial(\rho Y_k)}{\partial t} + \frac{\partial(\rho U_i Y_k)}{\partial x_i} = -\frac{\partial(\rho V_{ki} Y_k)}{\partial x_i} + \dot{\omega_k} \tag{2.13}$$

V_{ki} is the i-component of the diffusion velocity of species k and $\dot{\omega_k}$ is the chemical source term, defined as the mass of species k which is produced or consumed per unit volume and time. Because of the mass conservation it can be demonstrated:

$$\sum_{k=1}^{N} \dot{\omega_k} = 0 \tag{2.14}$$

and through the definition of mass fraction:

$$\sum_{k=1}^{N} \rho_k = 1 \tag{2.15}$$

The diffusion velocities are obtained by solving the system:

$$\nabla X_k = \sum_{j=1}^{N} \frac{X_k X_j}{D_{kj}}(V_j - V_k) + (Y_k - X_k)\frac{\nabla p}{p} + \frac{\rho}{p}\sum_{j=1}^{N} Y_k Y_j (f_k - f_j) \quad \text{for} \quad p = 1, N \tag{2.16}$$

where f_k is the magnitude of the volumetric force acting on species k, $D_{kj} = D_{jk}$ is the binary diffusion coefficient of species j into species k and where the Soret effect has been neglected for the sake of simplicity.

This computation represents a linear system of size N^2 which must be solved in each direction, each point and instant for unsteady flows. This task is difficult and computationally very costly and, in most cases, Fick's law is used instead:

$$V_{ki} Y_k = -D_k \frac{\partial Y_k}{\partial x_i} \tag{2.17}$$

Equation 2.17 offers a convenient approximation for combustion processes, where Lewis numbers of individual species vary in small amounts in the flame front. The Lewis number represents the ratio between the thermal diffusion and the molecular diffusion of species k. This number is commonly used to characterize the diffusion coefficients. It can be expressed in the form:

$$Le_k = \frac{\lambda}{\rho C_p D_k} = \frac{D_{th}}{D_k} \tag{2.18}$$

The Lewis number is a local quantity but, in most gases, it changes very little from one

point of the flame to another. From the kinetic theory of gases [34] we know that λ changes roughly like $T^{0.7}$, ρ like T^{-1} and D_k like $T^{1.7}$ so that Le_k is changing only by a few percents in a flame.

2.4. An introduction to chemical kinetics

In a system of N species reacting through M reactions in the form:

$$\sum_{k=1}^{N} \nu'_{kj}\chi_k \rightleftharpoons \sum_{k=1}^{N} \nu''_{kj}\chi_k \quad \text{for} \quad j = 1, M \tag{2.19}$$

where χ_k represents the symbol and ν'_{kj}, ν''_{kj} are the molar stoichiometric coefficients as reactant and product respectively of species k in the j reaction, the amount of species j produced or consumed per unit time and volume is then:

$$\dot{\omega_k} = W_k \sum_{j=1}^{M} (\nu''_{jk} - \nu'_{jk}) r_j \tag{2.20}$$

where r_j represents the reaction rate of the j-th reaction. The phenomenological law of mass action states that the reaction rate is proportional to the product of the concentrations. For an equilibrium reaction like 2.19, the net reaction rate is the difference between the forward and the reverse reaction rates and can be expressed in the form:

$$r = k_f \prod_{k=1}^{N} [\chi_k]^{\nu'_k} - k_r \prod_{k=1}^{N} [\chi_k]^{\upsilon''_k} \tag{2.21}$$

where $[\chi_k]$ represent the molar concentration of the species involved in the reaction.

The forward rate constant for the j-th reaction is generally assumed to have the following Arrhenius temperature dependence:

$$k_{f_j} = A_j T^{\beta_j} exp(\frac{-E_j}{RT}) \tag{2.22}$$

In this equation A_j, β_j and E_j represent the pre-exponential factor, the temperature exponent and the activation energy respectively. These values are characteristic for each reaction and do not depend on the temperature. The reverse reaction rate is related to the forward reaction rate through the equilibrium constant by:

$$k_r = \frac{k_f}{K_{eq}} \tag{2.23}$$

The equilibrium constant for the reaction j can be obtained through the relationship:

$$K_{eq_j} = exp\left(\frac{\Delta S_j^0}{R} - \frac{\Delta H_j^0}{RT}\right)\left(\frac{p_{atm}}{RT}\right)^{\sum_{k=1}^{N}\nu_{kj}} \tag{2.24}$$

The use of equilibrium constants for reactions involving electrons is not appropriate. In the case of combustion reactions this approximation is valid and will be used throughout this work.

2.4.1. Chemical Mechanisms

Mathematically, a chemical mechanism is a set of coupled and often stiff, first-order differential equations. There are many software packages available that efficiently and simply solve these equations to obtain species concentrations as a function of time. Such software can be applied to a wide range of complex chemical systems such as multi-phase CVD-reactions, combustion, catalysis and many other applications. A mechanism includes a list of all primary, secondary, and intermediate reactions which give certain, essentially qualitative, information about the fate of a species.

In combustion systems, kinetic models have thousands of elementary reactions and a large number of reactive intermediates. For example there are 3662 reactions involving 470 chemical species considered in the simulations of n-hexane combustion by Glaude et al [26] and 479206 reactions and 19052 chemical species in simulation of tetra-decane combustion performed by De Witt et al [18]. Gri-Mech is a compilation of 325 elementary chemical reactions and associated rate coefficient expressions and thermochemical parameters for the 53 species involved in them. Such mechanisms like the ones mentioned above are too computationally expensive and, in most cases, cannot be used in the simulation of a full scale combustion chamber. Many reduction techniques have been developed in the last years, that allow the generatation of simple mechanisms from the detailed ones without losing critical information about the main features of the chemical process. Some of the most common reduction techniques can be found below.

The chemical mechanisms used to simulate methane and hydrogen combustion in the present work are the ones from Kee et al. [46] for hydrogen and Ern and Smooke [24] for methane combustion. The species involved in these mechanisms, as well as the chemical reactions with their corresponding Arrhenius coefficients can be seen in Appendix A.

2.4.2. Mechanism reduction methods

2.4.2.1. Equilibrium Chemistry

A chemical reaction is in equilibrium when the species concentrations remain constant in time. Such equilibrium states can be determined through minimization of Gibbs free en-

ergy or through integration for $t \rightarrow infinity$ of the following differential equations for a homogeneous time-dependent system:

$$\frac{dY_k}{dt} = W_k, \ k = 1, ..., N \text{ where } W_k = \dot{\omega}_k/\rho \tag{2.25}$$

For laminar flames the equilibrium hypothesis is inexact in most cases because intermediate species cannot be determined and the species concentrations are only valid very far away from the flame front. The method for mechanism reduction through partial equilibrium is based on the assumption that the fastest reactions are in equilibrium. This is only true when the reaction rates for the forward and backward reactions are very close. One can solve these elementary reactions through algebraic relationships and the computation of the Jacobi matrix can be avoided. The justification of the classification in fast and slow scales takes place through comparison with flow time scales. This means that an analysis of each reaction's Damköhler number must be done. Some studies have shown that the strategy of the partial equilibrium is limited to high-temperature, mixing controlled diffusion flames involving rapidly reacting components.

2.4.2.2. Quasi Steady State Assumption

For explanation of this method let's consider the following reaction:

$$A \rightarrow B \rightarrow C \tag{2.26}$$

The evolution of the concentration rates for species A, B and C can be described by the following differential equations:

$$\frac{d[A]}{dt} = -k_{12}[A], \ \frac{d[B]}{dt} = k_{12}[A] - k_{23}[B], \ \frac{d[C]}{dt} = k_{23}[B] \tag{2.27}$$

The solution of the first equation can be found easily:

$$[A] = [A]_0 exp(-k_{12}t) \tag{2.28}$$

If the reaction velocities have different orders of magnitude, for example $k_{12} \ll k_{23}$, the concentration of species B in the mixture will be very small. The velocity at which B is consumed is almost as high as the generation velocity and therefore there is an equilibrium:

$$\frac{d[B]}{dt} = k_{12}[A] - k_{23}[B]. \tag{2.29}$$

This is the quasi-steadiness principle (see [98]), according to this assumption the concentration of B can be considered to be steady in time. When we observe the concentration

of species C we obtain the following expression:

$$\frac{d[C]}{dt} = k_{23}[B] \tag{2.30}$$

By using the quasi-steadiness assumption, the concentration of C can be expressed in terms of the concentration of A:

$$\frac{d[C]}{dt} = k_{12}[A] = k_{12}[A]_0 exp(-k_{12}t) \tag{2.31}$$

Integrating this expression one obtains:

$$[C] = [A]_0(1 - exp(-k_{12}t)) \tag{2.32}$$

The quasi-steadiness assumption has the advantage of decoupling the differential equations 2.27, which reduces the stiffness of the Jacobi matrix and, this way, the complexity of the computation. The species having short periods of existence are not eliminated from the mechanism but can be evaluated through simple algebraic expressions.

2.4.2.3. ILDM-Model

The Intrinsic Low-Dimensional Manifold method introduced by Mass and Pope [51] identifies the fast processes by using an eigenvalue analysis of the local Jacobian of the chemical source terms. By omitting the convection and diffusion terms in the species equation we obtain the time-dependent differential equation system 2.25.

Writing the equation in vector notation one obtains: $d\mathbf{Y}/dt = \mathbf{W}$, with $\mathbf{Y} = (Y_1, Y_2, ..., Y_N)^T$ and $\mathbf{W} = (W_1, W_2, ..., W_N)^T$. This vector notation is used to describe the mixture as a N-dimensional space called the composition space. Formally p, and h are needed to describe the complete composition of the mixture but, since they are constant in this case, they have not been introduced in this vector notation. To identify the fast and slow chemical processes, the chemical source term $\mathbf{W}$ is linearized around the reference composition $\mathbf{Y^0}$:

$$\frac{d\mathbf{Y}}{dt} \approx W(\mathbf{Y^0}) + J(\mathbf{Y^0})(\mathbf{Y} - \mathbf{Y^0}) \tag{2.33}$$

where $\mathbf{J}(\mathbf{Y^0})$ is the $N \times N$ Jacobian matrix with elements $J_{ij} = \partial W_j / \partial Y_i \mid_{Y^0}$. The local characteristics of the system can be examined by transforming 2.33 into the basis of eigenvectors of the Jacobian matrix. The Jacobian matrix is therefore diagonalized as follows:

$$\mathbf{J} = \mathbf{SLS}^{-1} \tag{2.34}$$

where $\mathbf{L}$ is a diagonal matrix with the eigenvalues λ_k. The columns of the matrix $\mathbf{S}$ are the right eigenvectors $\mathbf{s_K}$ of the jacobian matrix. By using the transformation $\mathbf{Y} = \mathbf{S}[\hat{\mathbf{Y}}]$ the eq.

2.33 can be written in the basis of eigenvectors:

$$\frac{d\hat{\mathbf{Y}}}{dt} = \hat{\mathbf{W}}^0 + \mathbf{L}(\hat{\mathbf{Y}} - \hat{\mathbf{Y}}^{\mathbf{0}}) \tag{2.35}$$

with $\hat{\mathbf{W}}^{\mathbf{0}} = \mathbf{S}^{-1}\mathbf{W}(\mathbf{Y}^{\mathbf{0}})$. As a result of this transformation, the differential equations in 2.25 are decoupled and the evolution of each mode $\hat{Y}_k$ is described by:

$$\frac{d\hat{Y}_k}{dt} = \hat{W}_K^0 + \lambda_K(\hat{Y}_K - \hat{Y}_K^0). \tag{2.36}$$

This equation gives us the basis for a time-scale analysis of the different modes. When the absolute value of the eigenvalue λ_K is small, the typical time scale of the corresponding mode is given by $(\hat{W}_K^0)^{-1}$. On the other hand, if the absolute value of the real part of the eigenvalue is large, the time scale is given by λ_K^{-1}. If the magnitude of λ_K is large, movements in the direction of the associated eigenvector will proceed fast. Modes with a positive real part of the eigenvalue will grow exponentially in time. For negative real parts the corresponding processes will relax towards a steady state. Modes with $\lambda = 0$ correspond to conserved quantities such as element mass fractions.

It can be concluded that the introduction of steady-state equations is most suitable for modes corresponding to eigenvalues with large negative real parts. If the modes are ordered in such a way that the eigenvalues with the lowest index correspond to the fastest damping processes, the steady-state equations may be written as:

$$s_k^L \mathbf{W} = 0, \ k = 1, ..., N_{st} \tag{2.37}$$

where $\mathbf{s_K^L}$ are the left eigenvectors of the Jacobian matrix. Since the analysis is based on the local Jacobian matrix, the combination of species in steady state changes in composition space. The collection of all points in composition space satisfying 2.37 forms an $(N - N_{st})$-dimensional subspace: the intrinsic low-dimensional manifold. In the reduced model, the fast chemical processes are assumed in steady state and only movements within the manifold are allowed. Conservation equations have to be solved for these slowly changing variables only, which reduces the computational cost.

2.5. Combustion Theory

The basic concepts regarding hydrocarbon combustion will be summarized here. We will restrict ourselves to methane and hydrogen combustion, since these are the fuels that take part in the numerical simulations present in this thesis.

Air is basically a mixture of nitrogen (N_2) and oxygen (O_2). Any other components are neglected in this work (Argon, CO_2,...) because they are present in very small amounts

and do not play a relevant role in methane or hydrogen combustion. Let β be the ratio between the number of moles of nitrogen and oxygen. The value 3.764 has been used for this parameter in the present work.

Methane combustion in presence of air can be roughly described by one reaction with the following balance of products and reactants:

$$CH_4 + 2(O_2 + \beta N_2) \rightarrow CO_2 + 2H_2O + 2\beta N_2 \tag{2.38}$$

In the case of hydrogen combustion, the balance is as follows:

$$H_2 + \frac{1}{2}(O_2 + \beta N_2) \rightarrow H_2O + \frac{1}{2}\beta N_2 \tag{2.39}$$

In this simple model nitrogen does not react and its only role is that of a solvent for the other species. Methane and oxygen are transformed in carbon dioxide and water vapor while hydrogen combustion leads to the generation of water vapor as the only product. This model constitutes a very rough approximation of what happens in real combustion and won't be used in later computations.

2.5.1. Nitrogen reactions

Actually, the nitrogen present in the air does not remain "untransformed" during the combustion process. In fact, a part of the nitrogen is converted into nitrogen oxides. These products are pollutants and their emissions must be controlled following a very strict regulation. The consideration of the reactions involving nitrogen is thus often required.

A very common procedure consists of decoupling the simulation of the combustion and the prediction of the nitrogen oxides. Following this approach, the flame is simulated without considering the chemistry of the nitrogen. After this, when all other species are determined in the flame, the reactions involving nitrogen are reproduced. This procedure is only an approximation, but it is justified by the very long characteristic times of nitrogen reactions in comparison with other chemical reactions taking place in the combustion process.

In the following study we will make use of the assumption that nitrogen does not react during the combustion process.

2.5.2. Excess air and air factor

One kilogram of fuel requires a certain minimum of ambient air to be fully combusted. We call this minimum amount of air the stoichiometric air or theoretical air to combust the fuel. The stoichiometric air will completely combust the fuel to carbon dioxide (CO_2), water (H_2O) and sulfur dioxide (SO_2), if sulfur is present. If the fuel does not get enough air for combustion it will generate smoke and a potentially unhealthy mixture of stack gas products.

In addition, energy is wasted. The same applies if too much excess air is used for combustion. A less trivial issue in combustion technology is therefore to ensure the proper amount of air that minimizes environmental impact and fuel consumption.

For convenience we define the stoichiometric air as the air to fuel ratio, AF (kg air/kg fuel), and the excess air factor as:

$$\lambda = \frac{Mass\ of\ air\ (Kg)\ to\ combust\ one\ Kg\ of\ fuel}{Stoichiometric\ air\ (AF)} \tag{2.40}$$

λ values greater than 1.0 indicate excess air and are called lean mixtures. λ values less than 1.0 indicate excess fuel for complete combustion, and are called rich mixtures.

The air to fuel ratio (AF) is a property of a fuel that can be calculated from its composition. Table 2.1 shows the AF ratio and maximum wet CO_2 corresponding to some fuels of general interest.

Table 2.1.: Air to Fuel ratio for various Fuels

Fuel	Phase	AF	$CO_{2\ max}\ wet$
Very light fuel oil	liquid	14.27	13.56
Light fuel oil	liquid	14.06	13.72
Medium heavy fuel oil	liquid	13.79	14.00
Heavy fuel oil	liquid	13.46	14.14
Bunker C	liquid	12.63	16.23
Generic Biomass (maf)	solid	5.88	17.91
Coal A	solid	6.97	16.09
LPG (90 P : 10 B)	gas	15.55	11.65
Carbon solid	solid	11.44	21.00

The AF ratio has nothing to do with the furnace design or combustion process, while λ is a parameter that tells us how efficiently a fuel was combusted. The closer λ is to one, the more efficient is the furnace or burner design and operation. Operating very close to the minimal amount of air (= stoichiometric air) has the inherent danger of smoke, CO generation and high temperatures leading to the formation of thermal NO_X (Zeldovich-mechanism [33]).

2.5.3. Low Mach number combustion

The low Mach number approach has been used in this study. More detailed information can be found in [77]. The approach is based on the fact that, for low Mach numbers, pressure variations along the flame are very small, typically in the range of some pascals. These vari-

ations are situated many orders of magnitude below the atmospheric pressure (the burner is supposed to be in thermodynamic equilibrium with the surrounding atmosphere). Considering this, specific equations can be established similar to those used for incompressible flows but allowing variations in the density which are essential for combustion.

The pressure can be decomposed in the summation of two terms, the surrounding atmospheric pressure, which is relevant for the thermodynamic state of the fluid and a variable hydrodynamic pressure. The first term is constant while the second is a function of time and space:

$$p(\vec{x},t) = p_{atm} + \tilde{p}(\vec{x},t),\ \tilde{p}(\vec{x},t) \ll p_{atm} \tag{2.41}$$

When regarding the flow pressure p, one can assume that it is equal to the atmospheric pressure by neglecting the hydrodynamic component. If we are interested in the pressure fluctuations, it is the hydrodynamic pressure that has to be taken into account since p_{atm} remains constant in time and space.

For all calculations performed in the present work and presented in the following chapters, the surrounding atmospheric pressure has been considered equal to the atmospheric pressure (101325 Pa).

2.6. Numerical Methods

The Navier-Stokes equations cannot be solved analytically except for a few simple flow types under certain assumptions. The system of partial differential equations must be discretized and solved through iterative methods. In this section some of the numerical methods used for the resolution of this equations system are enumerated and explained. Some of these methods were already available in the CFD-Code FASTEST-3D and some have been implemented as a part of the present work.

2.6.1. The finite-volume method

Let us consider the generic conservation equation for a quantity ϕ:

$$\int_S \rho\phi\mathbf{v}\cdot\mathbf{n}dS = \int_S \Gamma\mathbf{grad}\phi\cdot\mathbf{n}dS + \int_\Omega q_\phi d\Omega \tag{2.42}$$

and assume that the velocity field and all fluid properties are known. The domain is divided in a finite number of small control volumes. The conservation equation 2.42 is applied to each control volume as well as to the solution domain as a whole. If we sum equations for all control volumes we obtain the global conservation equation (surface integrals over inner faces cancel out).

2.6.1.1. Surface integrals

The surface of the control volume can be decomposed in four (2D) or six (3D) faces denoted by e, w, n, s, t and b corresponding to their direction. The flux through the boundary of our control volume is:

$$\int_S f dS = \sum_k f dS \tag{2.43}$$

where f is the component of the convective ($\rho\phi\mathbf{v}\cdot\mathbf{n}$) or diffusive ($\Gamma\mathbf{grad}\phi\cdot\mathbf{n}$) vector in the direction normal to the face.

To calculate the surface integral two levels of approximation are used. The integral is approximated in terms of the variable values at one or more locations on the cell face or in terms of the values at the center of the control volumes. If the integral is approximated as a product of the integrand at the face center and the face area we obtain a second-order approximation. The mean value of the flux through the e face f_e is then calculated by interpolation of the values of f at the adjacent nodes. This can be done by substituting the integral:

$$\int_{S_e} f dS = f_e S_e \tag{2.44}$$

Other higher order approximations can be achieved by considering the values of f at more locations on the face e.

The approximations to the integrals require the values of variables at locations other than the computational nodes. The integrand denoted by f, involves the product of several variables and/or variable gradients at those locations: $f = \rho\phi\mathbf{v}\cdot\mathbf{n}$ for the convective flux and $f = \Gamma\mathbf{grad}\phi\cdot\mathbf{n}$ for the diffusive flux. The interpolation techniques used to approximate the value of ϕ and its derivative are:

- Upwind Interpolation: the value of ϕ is approximated by it is upstream value:

$$\phi_e = \begin{cases} \phi_P & \text{if} \quad (\mathbf{v}\cdot\mathbf{n})_e > 0 \\ \phi_E & \text{if} \quad (\mathbf{v}\cdot\mathbf{n})_e < 0 \end{cases} \tag{2.45}$$

- Central Difference Scheme: the value ϕ_e can be approximated by the linear expression

$$\phi_e = \phi_E\lambda_e + \phi_P(1-\lambda_e) \tag{2.46}$$

  where $\lambda_e = \frac{x_e - x_P}{x_E - x_P}$.

  Using the Taylor series expansion of ϕ_E about the point x_P the first derivative disappears from the equation for ϕ_e and the error is proportional to $\partial^2\phi/\partial x^2$, this is, proportional to the square of the grid spacing. Assuming a linear profile between P

and E offers a very simple expression for the gradient, needed for evaluation of diffusive fluxes:

$$\frac{\partial \phi}{\partial x} \approx \frac{\phi_E - \phi_P}{x_E - x_P} \tag{2.47}$$

2.6.1.2. Volume integrals

Volume integrals are approximated by the product of the cell volume and the mean value of f in the cell:

$$Q_P = \int_\Omega q d\Omega = \overline{q} \Delta\Omega \approx q_P \Delta\Omega \tag{2.48}$$

where q_p is the value of q at the center of the control volume. This is a first-order approximation, the solution is exact if the variation of q is linear in space. An approximation of higher order requires values of q at more locations in the cell.

2.6.1.3. Deferred correction

High order flux approximations can be calculated explicitly by using values from the previous iteration. This approximation can be combined with an implicit lower-order approximation which uses only values at nearest neighbors:

$$F_e = F_e^L + (F_e^H - F_e^L)^{old} \tag{2.49}$$

The term in brackets may be multiplied by a factor β, thus blending the two schemes.

A high order approximation provides a more accurate solution when the grid is fine enough to capture the essential details of the solution.

2.6.2. The SIMPLE algorithm

The SIMPLE algorithm for the velocity-pressure coupling has been used in this work. It was developed by Patankar and Spalding [66] and has since then been refined by a number of authors.

Variants rejoicing in the names of SIMPLEC [94], [79], SIMPLEX [79], SIMPLEN [92], SIMPLER [66] and PISO [39] aim to improve the coupling of the momentum and pressure equations via minor modifications of the SIMPLE algorithm.

The scheme is a predictor-corrector method, with an initial estimate for the velocity field from the Navier-Stokes equations being corrected with the continuity equation to force the conservation of mass. The prediction and correction operations are enclosed in an iterative loop which converges to give a solution that satisfies all the equations in the system.

The initial scheme by Patankar and Spalding was for a staggered Cartesian mesh, with the velocity values being located at the faces of finite volume cells, and the pressure, temperature and other scalar variables being located at the cell centers. Rhie and Chow [80] extended the method to use collocated grids, where the velocities and the other variables are all located at the cell centers, and this has been further developed by Perić and other authors ([71], [28]). Such a grid allows an easier conversion to non-Cartesian meshes. Here it will be described for Cartesian meshes.

The first stage of the calculation process is the resolution of the discretized versions of the momentum equations 2.2 using the current estimate of the pressure field, and using a cell face mass flux that is interpolated from the current estimate of the velocity field (this interpolation procedure is discussed in more detail in Section 2.6.4). The momentum equations 2.2 are in the same general form as the generic transport equation. For a given mass flux field and pressure field they can be discretized into equations of the form:

$$\begin{aligned} a_P u_P^* + \sum_{n=nb} a_n u_n^* &= S_x + A_x \frac{dp}{dx} \\ a_P v_P^* + \sum_{n=nb} a_n v_n^* &= S_y + A_y \frac{dp}{dy} \\ a_P w_P^* + \sum_{n=nb} a_n w_n^* &= S_z + A_z \frac{dp}{dz} \end{aligned} \tag{2.50}$$

where u_p^*, v_p^* and w_p^* are the new estimates of velocity in the x, y and z. axis, and nb refers to the neighboring cells. A_x, A_y and A_z represent the areas of the cell faces normal to the x, y and z axis. The pressure gradient can be found by interpolating the pressure field at the cell faces using a linear interpolation, and then approximating the gradient across the cell with a centered difference as:

$$\begin{aligned} \frac{dp}{dx} &\approx \frac{p_e - p_w}{\Delta x}, \\ \frac{dp}{dy} &\approx \frac{p_n - p_s}{\Delta y}, \\ \frac{dp}{dz} &\approx \frac{p_t - p_b}{\Delta z}, \end{aligned} \tag{2.51}$$

for a regular mesh where Δx, Δy and Δz are the cell dimensions.

After the calculation of the velocity field estimates, the cell face velocities can be interpolated from their values at the cell centers, and the cell face mass fluxes can be calculated. For the eastern face of a cell the velocity normal to the face is u_e, whilst the face has an area A_e. The mass flow across the face is:

$$m_e = \rho A_e u_e \tag{2.52}$$

In general this interpolated velocity field will not be mass conserving (i.e., it will not have a discrete divergence of zero), and so will not satisfy the discretized version of the continuity equation:

$$m_e - m_w + m_n - m_s + m_t - m_b = 0, \tag{2.53}$$

which can be written for the face velocities on a Cartesian meshes as:

$$\rho A_e u_e - \rho A_w u_w + \rho A_n v_n - \rho A_s v_s + \rho A_t w_t - \rho A_b w_b = 0, \tag{2.54}$$

We therefore wish to calculate a corrected velocity field u^{**}, $v^{**}$and w^{**}that is mass conserving, together with a corresponding pressure field p^{**}. We do so by adding a velocity and pressure correction to the original estimation of the velocity and pressure fields:

$$\begin{aligned} u^{**} &= u^* + u', \\ v^{**} &= v^* + v', \\ w^{**} &= w^* + w', \\ p^{**} &= p + p', \end{aligned} \tag{2.55}$$

where a dash $'$ signifies the correction field.

The expressions in equation 2.55 are substituted into the u equation in equation 2.50

$$a_P(u_P^* + u_P') + \sum_{n=nb} a_n(u_n^* + u_n') = S_x + A_x \frac{d}{d_x}(p + p'), \tag{2.56}$$

and the sum of the neighboring velocity terms approximated by:

$$\sum_{n=nb} a_n(u_n^* + u_n') \approx A_x \frac{dp'}{dx} \tag{2.57}$$

which should be valid as $p' \to 0$ and $u' \to 0$. Subtracting the momentum equation gives an expression relating the correction pressure and velocity field to each other,

$$a_P u_P' \approx A_x \frac{dp'}{dx}, \tag{2.58}$$

or

$$\begin{aligned} u_P' &= \frac{A_x}{a_P}\frac{dp'}{dx}, \\ v_P' &= \frac{A_y}{a_P}\frac{dp'}{dy}, \end{aligned} \tag{2.59}$$

$$w'_P = \frac{A_z}{a_P}\frac{dp'}{dz},$$

where similar approximations have been made for the x, y and z components of velocity. By interpolating the expressions in equation 2.59 to the faces of the cell, the corrected cell face velocities normal to the face are given by:

$$\begin{aligned} u'_e &= \frac{A_{xe}}{a_{P_e}}\frac{p'_E - p'_P}{\delta x_e}, \\ v'_n &= \frac{A_{yn}}{a_{P_n}}\frac{p'_N - p'_P}{\delta y_n}, \\ w'_t &= \frac{A_{zt}}{a_{P_t}}\frac{p'_T - p'_P}{\delta z_n}, \end{aligned} \tag{2.60}$$

with the a_P terms being approximated at the faces by a linear interpolation

$$\begin{aligned} a_{P_e} &= \frac{a_{P_P} + a_{P_E}}{2}, \\ a_{P_n} &= \frac{a_{P_P} + a_{P_N}}{2}, \\ a_{P_t} &= \frac{a_{P_P} + a_{P_T}}{2}, \end{aligned} \tag{2.61}$$

In this interpolation a_{P_P} is the a_P term in the equation for the cell P, whilst a_{P_E} is the a_P term in the equation for cell E. Substituting the equations in 2.55 into the discretized continuity equation 2.54 yields

$$\begin{aligned} A_e(u^*_e - u'_e) - A_w(u^*_w + u'_w) + A_n(u^*_n + u'_n) \\ -A_s(u^*_s + u'_s) + A_t(u^*_t + u'_t) - A_b(u^*_b + u'_b) = 0 \end{aligned} \tag{2.62}$$

Using the expressions for u' from equation 2.60 and factorizing yields following equation for the pressure correction:

$$b_P p'_P + b_E p'_E + b_W p'_W + b_N p'_N + b_S p'_S + b_T p'_T + b_B p'_B = c \tag{2.63}$$

where

$$\begin{gathered} b_E = \tfrac{A_e^2}{a_{P_e}},\ b_W = \tfrac{A_w^2}{a_{P_w}},\ b_N = \tfrac{A_n^2}{a_{P_n}},\ b_S = \tfrac{A_s^2}{a_{P_s}},\ b_T = \tfrac{A_t^2}{a_{P_t}},\ b_B = \tfrac{A_b^2}{a_{P_b}} \\ b_P = -(b_E + b_W + b_N + b_S + b_T + b_B) \\ c = \tfrac{1}{\rho}(m_w - m_e + m_n - m_s + m_t - m_b) \end{gathered}$$

This can be solved for the pressure correction p', which is then used to update the cell

center and cell face velocities using equations 2.60 and 2.55, the resulting face velocities satisfying the continuity equation. The pressure field is updated using equation 2.55 and then the process is repeated, with the new velocity and pressure field being used to calculate the u^* velocities.

The SIMPLE algorithm is summarized in Figure 2.1 for the solution of a thermally driven three dimensional flow. To obtain the velocity, pressure and temperature fields, an estimate of the velocity field u^*, v^* and w^* is calculated through equation 2.50. The cell face velocities are then interpolated from the velocity field and the cell face mass fluxes calculated m^*. The pressure correction equation 2.63 is solved for p', and the velocity, mass flux, and pressure fields are updated using equation 2.55. The resulting mass conserving velocity field is then used to solve any transport equations for auxiliary scalar fields, such as temperature and species concentration.

- set initial fields for u^*, v^* w^*, p and T
- interpolate to find cell face mass fluxes F .

  repeat
  - solve Equation 2.50 for u^*, v^*, w^*
  - interpolate to find cell face mass fluxes m^*
  - calculate pressure correction p' from equation 2.63
  - update u, v, w, p and m using equation 2.55.
  - calculate T and any other scalar fields.
  - check for convergence. If converged, halt.

Figure 2.1.: The SIMPLE velocity-pressure coupling algorithm

The divergence of the m^* mass flux field (calculated as the source term in equation 2.63) is usually used as a convergence criteria. The system at this stage satisfies the momentum equations (they having just been solved) whilst a divergence free m^* mass flux field signifies that the solution also satisfies the continuity equation. After the update of the m fields with the pressure correction p', the divergence should be equal to zero, a non-zero divergence signifying an incorrectly solved pressure correction equation. However, the corrections to the velocity fields means that the momentum equations may no longer be satisfied, and so the algorithm repeats. To aid the convergence of the method, the velocity, pressure and scalar field updates can be underrelaxed using some relaxation parameter. There are two obvious methods of under-relaxation, either by relaxing the update:

$$\begin{aligned} u &= u^* + \alpha_u u', \\ v &= v^* + \alpha_v v', \\ w &= w^* + \alpha_w w', \\ p &= p^* + \alpha_p p', \end{aligned} \tag{2.64}$$

where α_u, α_v, α_w and α_p are the relaxation parameters for the velocity and pressure fields respectively, or by relaxing the diagonal coefficient of the linear system for each variable, for example the u velocity equation 2.50 being modified to:

$$\frac{a_P}{\alpha_u} u_P^* + \sum_{n=nb} a_n u_n = S_x + A_x \frac{dp}{dx} \tag{2.65}$$

The pressure equation relaxation should always be of the form of equation 2.64, and no relaxation should be used in the update of the face velocities and mass fluxes. Unlike the transport equation, the pressure equation is always diagonally dominant and does not require the under-relaxation of the diagonal. By avoiding the relaxation of the face velocity updates, a mass conserving flux field is calculated, which ensures the conservation of enthalpy, momentum and other properties. It can also be noted that if a relaxation of the form of equation 2.65 is used for the momentum equations, then a non-relaxed value of a_P should be used in the pressure correction and velocity interpolation operations.

To model a transient problem the iterative process outlined in Figure 2.1 is carried out at every time step, using the velocity, pressure and scalar fields from the previous time step as the initial guess for the values at the new time step. This can be quite time consuming and more efficient time stepping procedures, which will not be discussed here, are used instead [28].

For steady state problems, the SIMPLE coupling scheme can be considered as a pseudo-transient process, with an implicit calculation of the momentum equations being corrected via an explicit pressure correction process, each iteration of the scheme corresponding to a pseudo time step. When modeling a transient flow, each time step comprises a number of pseudo-transient time steps to obtain the converged solution for the physically real time step.

2.6.3. The SIP-solver

The so called SIP-solver is used in the FASTEST-3D code to solve the matrix equations in the given form:

$$[\mathbf{A}]_\mathbf{h}\{\mathbf{\Phi}\}_\mathbf{h} = \{\mathbf{S}\}_\mathbf{h} \tag{2.66}$$

resulting from an iteration step of the SIMPLE algorithm. $[\mathbf{A}]_\mathbf{h}$ is a $n \times n$ matrix, $\mathbf{\Phi_h}$ and $\mathbf{S_h}$ represent n-dimensional vectors. $\mathbf{S_h}$ contains the source terms of the discretized partial differential equations and $\mathbf{\Phi_h}$ represents the (exact) solution of the matrix equation.

The SIP-solver involves an iterative procedure, computes a series of solutions $\mathbf{\Phi_h^1}$, $\mathbf{\Phi_h^2}$, $\mathbf{\Phi_h^3}$,... from an estimated initial approximation $\mathbf{\Phi_h^0}$.

According to [90], the solution of the linear set of equations after each iterative step can be described through:

$$\{\mathbf{\Phi}\}_\mathbf{h}^{\mathbf{i+1}} = (\mathbf{II} - [\mathbf{B}]^{-1}[\mathbf{A}]_\mathbf{h})\{\mathbf{\Phi}\}_\mathbf{h}^\mathbf{i} + [\mathbf{B}]^{-1}\{\mathbf{S}\}_\mathbf{h} \tag{2.67}$$

Here $\mathbf{II}$ represents the unit matrix. $\mathbf{B}$ is a freely selectable regular matrix. It should be as similar and so easy invertible as matrix $\mathbf{A}$ as possible.

The SIP-solver is based on the principle of the LU decomposition, that is, an approximate LU decomposition is introduced instead of the matrix $[\mathbf{A}]_\mathbf{h}$:

$$[\mathbf{L}]_\mathbf{h}[\mathbf{U}]_\mathbf{h} = [\mathbf{A}]_\mathbf{h} + [\mathbf{E}]_\mathbf{h}, \tag{2.68}$$

where $\mathbf{L_h}$ is a lower and $\mathbf{U_h}$ is an upper triangle matrix. The matrices $\mathbf{L_h}$ and $\mathbf{U_h}$ are particularly set up for the matrices resulting from the discretization of the Navier Stokes equations. Their exact form can be found in [28]. The matrices $\mathbf{L_h}$ and $\mathbf{U_h}$ depend on a parameter α, which is set equal to 0.92.

2.6.4. Rhie-Chow Velocity Interpolation

The key to the shift from a staggered to a collocated mesh is the interpolation of the velocity field to the cell faces. A naïve linear interpolation of the cell center velocities can lead to a pressure chequer-boarding process, where the pressures on odd and even numbered cells are uncoupled from each other [122].

The Rhie-Chow interpolation method [80] interpolates in a form consistent with the velocity correction equation 2.59 as follows. The equation for the axis component of momentum can be written as

$$u_P - \frac{A_x}{a_P}\frac{dp}{dx} = \frac{S_x}{a_P} - \frac{1}{a_P}\sum_{n=nb} a_n u_n \tag{2.69}$$

Writing equation 2.69 for the P and E cells as

$$\begin{aligned} u_P - \left(\frac{A_x}{a_P}\right)\left(\frac{dp}{dx}\right)_P &= \left(\frac{S_x}{a_P}\right)_P - \left(\sum_{n=nb} a_n u_n\right)_P, \\ u_E - \left(\frac{A_x}{a_P}\right)\left(\frac{dp}{dx}\right)_E &= \left(\frac{S_x}{a_P}\right)_E - \left(\sum_{n=nb} a_n u_n\right)_E, \end{aligned} \tag{2.70}$$

and assuming that a similar equation can be written for the velocity at the east face of the cell gives:

$$u_e - \left(\frac{A_x}{a_P}\right)\left(\frac{dp}{dx}\right)_e = \left(\frac{S_x}{a_P}\right)_e - \left(\sum_{n=nb} a_n u_n\right)_e \tag{2.71}$$

This equation is then approximated by a linear interpolation of the equations for the centers of the E and P cells given in equation 2.70. Performing such an interpolation for the left hand side of equation 2.71 gives:

$$\begin{gathered} u_e - \left(\frac{A_x}{a_P}\right)_e \left(\frac{dp}{dx}\right)_e = \\ \frac{1}{2}\left(u_P - \left(\frac{A_x}{a_P}\right)_P \left(\frac{dp}{dx}\right)_P + u_E - \left(\frac{A_x}{a_P}\right)_E \left(\frac{dp}{dx}\right)_E\right) \end{gathered} \tag{2.72}$$

which can be rewritten as an expression for u_e:

$$\begin{gathered} u_e = \frac{u_P + u_E}{2} + \\ \left(\frac{A_x}{a_P}\right)_e \left(\frac{dp}{dx}\right)_e - \frac{1}{2}\left(\left(\frac{A_x}{a_P}\right)_P \left(\frac{dp}{dx}\right)_P + \left(\frac{A_x}{a_P}\right)_E \left(\frac{dp}{dx}\right)_E\right) \end{gathered} \tag{2.73}$$

The pressure gradients can be approximated by centered differences as:

$$\begin{aligned} \left(\frac{dp}{dx}\right)_e &= \frac{p_E - p_P}{\delta x_e}, \\ \left(\frac{dp}{dx}\right)_P &= \frac{p_E - p_W}{\delta x_e + \delta x_w}, \\ \left(\frac{dp}{dx}\right)_E &= \frac{p_{EE} - p_P}{\delta x_{ee} + \delta x_e}, \end{aligned} \tag{2.74}$$

The approximation of the $(A_x/a_P)_e$ term by a linear interpolation

$$\left(\frac{A_x}{a_P}\right)_e = \frac{1}{2}\left(\left(\frac{A_x}{a_P}\right)_E + \left(\frac{A_x}{a_P}\right)_P\right) \tag{2.75}$$

gives a complete interpolation formula for u_e

$$u_e = \overline{u_e} + \overline{\left(\frac{A_x}{a_P}\right)_e}\left(\frac{dp}{dx}\right)_e - \overline{\left(\frac{A_x}{a_P}\right)_e \left(\frac{dp}{dx}\right)_e} \tag{2.76}$$

where an overbar $\overline{()}_e$ signifies a linear interpolation of the values at the P and E cell centers. Similar expressions can be obtained for the u_n and u_t face velocities, and the face mass fluxes m can be calculated by multiplying by the density and the area of the relevant cell face.

2.6.5. Solution methods for chemical kinetics problems

There has been a significant amount of work undertaken for transient chemical kinetics problems and stiff ordinary differential equations for zero and 1D flows. This work has implications for the approach implemented here, and the important aspects are therefore summarized below. The successful solution methods have the following characteristics:

- Implicit: These methods are stable and damp out perturbations due to rapid transients. The usual methods adopted are based upon Backward Difference Methods (BDF), and are included in many popular calculation packages such as CHEMKIN and FACSIMILE. Other implicit methods, such as implicit Runge-Kutta methods are generally not as popular.

- Newton methods for the non-linear equation systems which arise at each time step. Conventional predictor-corrector iterative strategies will not converge on stiff problems. Segregated solution methods are effectively predictor-corrector methods and, therefore, will only converge if the time step is comparable with the shortest time scales in the problem. A Newton method increases the radius of convergence, but it still requires a good initial guess to achieve convergence. When the solution is changing rapidly, e.g. in an initial transient, it is necessary to restrict the time step for convergence and not just for accuracy. When the solution is not changing very rapidly, then large steps may be taken. However, if the time steps are small, there is no advantage to be gained in using a Newton method, with its higher computational overheads.

- The Operator-Splitting or Fractional Step methods, where specialized chemical kinetics software is used for the stiff chemistry part and a conventional flow algorithm used for the flow. In this case, inconsistent discretization methods may be used in the different steps. It is desirable in the case of CFD algorithms, that methods are used, where the solution is consistent between the flow and chemistry and independent of the algorithm adopted, particularly for a steady state solution. This is the method implemented in the CFD-code FASTEST-3D as a part of the present work and it will be explained in more detail in section 2.6.6

- Higher order BDF methods enable larger time steps to be taken. However, it is necessary that the solution be smooth for higher order methods to work. In any time-split method the flow step will inject discontinuities into the chemical step, and prevent the use of higher order BDF methods. For a Newton approach to be beneficial, it is necessary to use an adaptive time step, or false time step. This will be small when the solution changes rapidly and increase as convergence becomes easier. Steady state problems are therefore one of the cases which benefit the most from this approach.

2.6.6. The Operator-Splitting method

Operator-splitting methods are powerful and efficient numerical methods designed for resolving sharp gradients. These methods are analogously applied nowadays to complex microphysical problems and multiphase chemical processes in clouds. Operator-splitting means that the spatial differential operator appearing in the equations is split into a sum of different sub-operators having simpler forms, and the corresponding equations can be solved easier. The sub-operators are usually chosen regarding the different physical processes or geometric directions. Then instead of the original problem, a sequence of sub-models is solved, which gives rise to the splitting error that will be discussed in detail in section 2.6.6.2.

2.6.6.1. Operator-Splitting procedures

There are generally two types of fractional-steps methods. Schemes such as ADI (Alternative Direction Implicit) employ a formulation where one or more terms are evaluated implicitly and all of the others are evaluated explicitly for a fraction of the step; then, in the next fractional step, another set of terms is taken implicitly, and an explicit combination of the remaining terms is used. The step is divided into as many fractions as there are terms to be differenced implicitly. This type of splitting is said to have absolute consistency, since each term of the differential equation is in some way represented during each fractional step [69].

The other class of methods allows one or more terms to be considered alone during each fractional step, while the remaining terms are ignored. These methods, called *majorant splitting*, are more appropriate for chemically reacting flow problems. This method, however, produces consistency only after all fractional steps are completed and not during each fractional step. Consider the following problem:

$$\left.\begin{aligned} &\frac{du(t)}{dt} = \mathbf{L}u(t) = (\mathbf{L}_1 + \mathbf{L}_2)u(t), \qquad t\epsilon(0,T] \\ &u(0) = u_0 \end{aligned}\right\} \tag{2.77}$$

where u is the unknown function, u_0 is a given element and $\mathbf{L}$, $\mathbf{L}_1$ and $\mathbf{L}_2$ are operators.

There exist several majorant splitting procedures. The simplest one is the *sequential splitting*, defined by the following sequence of sub-problems:

$$\left.\begin{aligned} &\frac{du_1(t)}{dt} = \mathbf{L}_1 u_1(t), \qquad t\epsilon((k-1)\tau, k\tau] \\ &u_1((k-1)\tau) = u_{spl}((k-1)\tau) \end{aligned}\right\}$$

$$\left.\begin{aligned} &\frac{du_2(t)}{dt} = \mathbf{L}_2 u_2(t), \qquad t\epsilon((k-1)\tau, k\tau] \\ &u_2((k-1)\tau) = u_1(k\tau) \end{aligned}\right\} \tag{2.78}$$

$$u_{spl}(k\tau) := u_2(k\tau)$$

with $k = 1, ..., m$ and $u_{spl}(0) = u_0$, where $u_{spl}(k\tau)$ is the solution of the split problem defined on the mesh $k\tau, k = 0, 1, ..., m$, $\tau = T/m$

Another splitting technique is the *Strang − Marchuk splitting* (see [91], [53]), where for one splitting timestep three sub-problems must be solved:

$$\left.\begin{aligned} &\frac{du_1(t)}{dt} = \mathbf{L}_1 u_1(t), \qquad t\epsilon((k-1)\tau, (k-\frac{1}{2})\tau] \\ &u_1((k-1)\tau) = u_{spl}((k-1)\tau) \end{aligned}\right\}$$

$$\left.\begin{aligned} &\frac{du_2(t)}{dt} = \mathbf{L}_2 u_2(t), \qquad t\epsilon((k-1)\tau, k\tau] \\ &u_2((k-1)\tau) = u_1(k\tau) \end{aligned}\right\} \tag{2.79}$$

$$\left.\begin{aligned} &\frac{du_3(t)}{dt} = \mathbf{L}_1 u_3(t), \qquad t\epsilon((k-\frac{1}{2})\tau, k\tau] \\ &u_3((k-1)\tau) = u_2(k\tau) \end{aligned}\right\}$$

$$u_{spl}(k\tau) := u_3(k\tau)$$

This procedure has been represented graphically in figure 2.2 with the y-axis representing the simulation time and the x-axis representing the chronological order of the steps of the method.

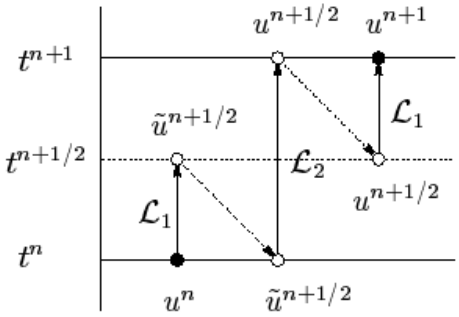

Figure 2.2.: Operator-Splitting Scheme

Strang splitting is second-order accurate and unconditionally stable if the discrete counterparts of $\mathbf{L}_1$ and $\mathbf{L}_2$ are positive definite matrices. Time-stepping of (at least) second-order is mandatory for all subproblems. In the cases where there are more than two operators in equation 2.77, these can be grouped in different ways, e.g. as follows:

$$\mathbf{L} = \mathbf{L}_1 + \mathbf{L}_2 + \mathbf{L}_3 = (\mathbf{L}_1 + \mathbf{L}_2) + \mathbf{L}_3 = \mathbf{L}_1 + (\mathbf{L}_2 + \mathbf{L}_3) = \mathcal{F}_1 + \mathcal{F}_2$$

The *weighted splitting* can be obtained by using two sequential splittings, once with the

order of operators $\mathbf{L}_1 \rightarrow \mathbf{L}_2$, and once with $\mathbf{L}_2 \rightarrow \mathbf{L}_1$. At time $t = k\tau$ the numerical solution is computed as a weighted average of the solutions obtained by the two sequential splitting steps

$$u_{spl}(k\tau) = \Theta u_{spl,\mathbf{L}_1\mathbf{L}_2} + (1-\Theta)u_{spl,\mathbf{L}_2\mathbf{L}_1}, \tag{2.80}$$

where $\Theta\epsilon[0,1]$ is a given weight parameter and $u_{spl,\mathbf{L}_1\mathbf{L}_2}(k\tau)$ and $u_{spl,\mathbf{L}_2\mathbf{L}_1}(k\tau)$ are the solutions of the two sequential splittings at time $k\tau$ respectively. The case $\Theta = \frac{1}{2}$ is called *symmetrically weighted splitting.*

In this work, the transport equations for the different species involved in the chemical reactions taking place are decoupled in two steps. First an explicit chemistry step is applied:

$$\frac{dx_k}{dt} = \dot{\omega_k} \tag{2.81}$$

and finally an implicit flow step takes place, which is given by the equation 2.13 where the source terms have been removed. Since equation 2.81 contains no spatial derivatives and there are no chemical source terms in the species transport equations, the set of equations is a system of $K+1$ ordinary differential equations at each node j.

It has been shown by previous investigators ([91], [19], [82]) that a symmetric splitting can lead to improved accuracy and efficiency of a numerical method. Although the improvement can be proved for certain operators, this is not the case in the present work, where the chemistry operator is a multistep variable algorithm. Even so, it is reasonable to expect that some advantage will be gained by using a symmetric operator. Moreover, we realize computational savings from the symmetric operator in addition to any potential gain in convergence rate.

Let us consider two operators which, when applied twice, advance the solution from t_i to t_{i+1}. We represent this procedure with a transport and a chemistry operator in the following expression:

$$f_{t+1} = L_T L_C L_C L_T f_t \tag{2.82}$$

The first L_T operator provides a predicted value of $f'_{t+1/2}$, then the first L_C operator does a correction of that first step. Then, since the sequence does not repeat with another $L_T L_C$ operation, the chemistry operator continues on to $t+1$, the L_C forming the predictor and and L_T the corrector.

It is preferable to restart the stiff ordinary differential equation integrator code as infrequently as possible, since there is some overhead associated with the startup algorithms. Specifically, the integrator begins with low-order methods and uses a small step size to obtain the required accuracy. Then, as the integration progresses, the history of the solution can be used to form higher-order difference approximations and allow so larger step sizes. Thus, proceeding from t to $t+1$ without interrupting the integrator permits a more efficient

utilization of the variable step size and order features of the ordinary differential equation solver. The result of the second chemistry operator is a predicted solution at $t + 1$, which the transport operator then uses as initial conditions to complete the step.

2.6.6.2. Errors of the method

The obvious disadvantages of operator-splitting methods are the temporal splitting errors. The order of the splitting error can be estimated theoretically [27]. In practice, splitting procedures are associated with different numerical methods for solving the sub-problems, which also cause a certain amount of error. This can usually lead to interaction between the two types of errors: the splitting error and the numerical error. If the numerical method is not properly chosen for the splitting procedure, order reduction may occur. The choices of the step size of the numerical method and the time parameter of the splitting procedure play an important role too.

It is also recommended by many authors ([37], [93], [48]) to introduce local grid refinement where the concentration gradients are very high to avoid qualitatively wrong behavior.

3. 1-D Simulations

It seems natural, when performing any kind of implementation in a CFD code or any other type of software, to start calculating simple problems before attempting more complex ones. The time and effort required for a calculation is shorter and the results can be more easily verified with available 1D tools. This way, the first step in order to achieve the coupling of the CFD-solver and the CHEMKIN-package has been the simulation of 1D configurations assuming constant properties of the gas (constant density and viscosity), and neglecting the species diffusion and heat transfer in order to reproduce the perfectly stirred reactor model in a one-dimensional simulation.

By means of the program SENKIN, we have obtained the solution for Y_k and T from the following system of differential equations:

$$\begin{aligned} \rho \frac{dY_k}{dt} &= \dot{\omega}_k \\ \rho c_{p_k} \frac{dT}{dt} &= -\sum_k \dot{\omega}_k h_k \end{aligned} \tag{3.1}$$

applied to the combustion mechanisms of hydrogen and methane. These equations represent a particular case of the species (2.13) and energy (2.4) transport equation in which all components of the velocity vector are equal to zero in the whole domain. They correspond to the definition of a perfectly stirred reactor, whose description has been given in section 1.4.2.3. The solutions given by the 1D tool SENKIN will be used to verify the results obtained by means of the operator-splitting scheme implemented in FASTEST-3D for a 1D configuration.

A second step in order to verify the validity of the implementation is the calculation of hydrogen and methane combustion in a plug-flow reactor (PFR). This model considers following assumptions:

- Axial flow
- Perfect mixing in radial direction but no mixing in axial direction
- Constant density
- Steady state

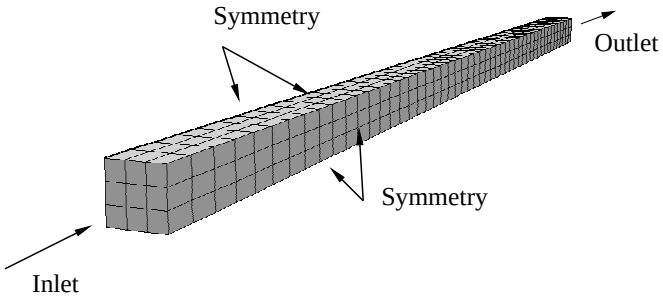

Figure 3.1.: Linear reactor used for H_2 and CH_4 1D combustion

The species and energy transport equations for the plug-flow reactor (with $D_k,\ \lambda = 0$) can be simplified to:

$$\begin{aligned} \rho u \frac{\partial Y_k}{\partial x} &= \dot{\omega}_k \\ \rho u c_{p_k} \frac{\partial T}{\partial x} &= -\sum_{k=1}^{N} h_k \dot{\omega}_k \end{aligned} \tag{3.2}$$

By forcing the velocity to be $u = 1$ in the whole domain, equations 3.2 are equivalent to equations 3.1 where the variable t has been substituted by the spatial variable x.

The computational geometry has been represented in figure 3.1. It consists of a cartesian grid with all the cells having equal dimensions and with a much larger number of them along the flow direction (50 for hydrogen and 500 for methane), while the cross section is divided in 3×3 cells. The boundary conditions used in the calculation have been presented in the same figure.

It is well known that mesh size and time step have a very big impact on errors associated to the operator-splitting scheme ([37], [93] and [48]). Several simulations have been performed for different values of these parameters, as well as for different temporal discretization schemes, in order to achieve the required knowledge to be applyed latter in more complex 2D configurations. Since the operator-splitting scheme is applied usually to unsteady calculations (even in the case of steady processes), the temporal discretization of the problem is supposed to influence the accuracy of the method, even if not as critically as the spatial discretization [40].

By scaling the grid we can observe the influence of the spacing on the final solution. The time step of the splitting corresponds to twice the time step of the CFD-solver and, thus,

the scheme provides a Strang-type cycle:

$$\Delta t_{cfd} + 2 \times \Delta t_{chem} + \Delta t_{cfd}$$

This expression is equivalent to equations 2.79. All 1D and 3D simulations shown in this work make use of the same approach and, therefore, no description of chemical or mechanical time step will be made in following sections.

To determine the influence of the grid spacing and the time step in the results, the two parametrical analysis presented in the next sections have been performed. They show the solution of the PFR-problem for stoichiometric mixtures of fuel and air for different values of grid spacing and time step.

The results are given as a function of the temporal discretization (Δt), spatial discretization (Δx) constant all along the reactor, and of the $Courant - Friedrich - Lewis$ (CFL) number, which is the ratio of a time step to the cell residence time:

$$CFL = \frac{u\Delta t}{\Delta x} \tag{3.3}$$

The convergence criterion for the simulations performed with the code FASTEST-3D has been selected to be equal to 10^{-3}. This value is kept as well for the 2D simulations presented in the next chapter.

3.1. Stoichiometric — $H_2 - air$ combustion

Hydrogen will likely become the primary energy carrier in the future. On one hand, hydrogen has the potential for cutting greenhouse gas emissions as well as reducing rural, urban and regional air pollution. Besides, there is presently considerable interest worldwide in promoting hydrogen as a fuel for transport. As oil becomes more expensive, hydrogen may eventually replace it as a transport fuel and in other applications. This development becomes more likely as fuel cells are developed, with hydrogen as the preferred fuel, though storage at vehicle scale is a major challenge. Meanwhile hydrogen can be used in internal combustion engines [35]. The simplicity of some combustion mechanisms, which reproduce with reasonable accuracy the reactions taking place in hydrogen combustion, makes it a very attractive topic for computational analysis.

For the case of hydrogen combustion, a stoichiometric mixture of fuel and air evolves according to the species and temperature profiles shown in figure 3.2 and 3.3. These are the results provided by the SENKIN code that will be used as reference for the verification of the 1D results given by FASTEST-3D.

The initial temperature is set to 1400K. The fuel-air mixture is stoichiometric: $Y_{H_2} = 0.028$, $Y_{O_2} = 0.226$ and $Y_{N_2} = 0.745$ and the time step amounts to $1 \times 10^{-6} s$. Ignition starts

after $2 \times 10^{-5}s$. The temperature reaches 2800K after $2 \times 10^{-4}s$.

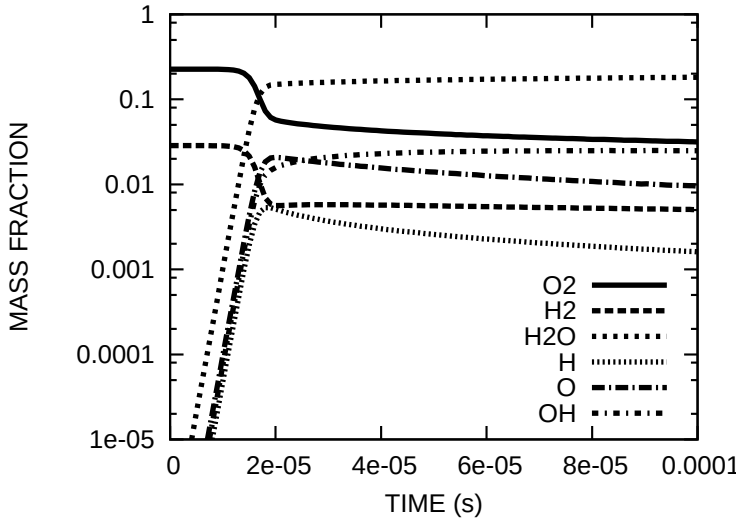

Figure 3.2.: Species evolution in stoichiometric H_2 combustion given by SENKIN

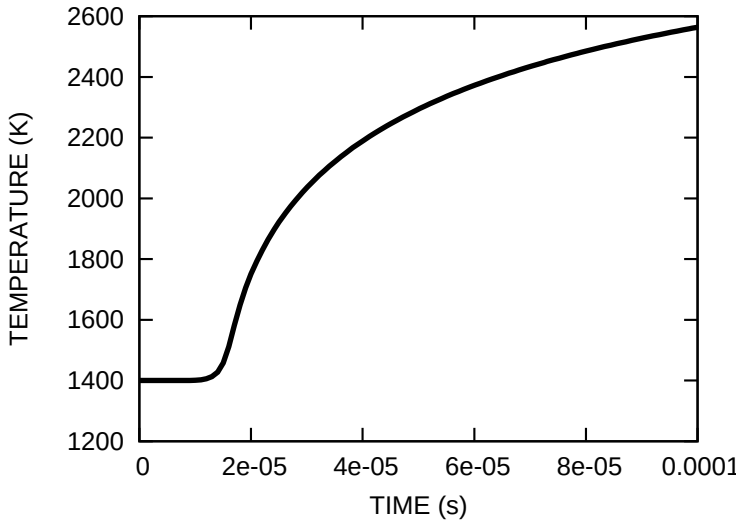

Figure 3.3.: Temperature evolution in stoichiometric H_2 combustion given by SENKIN

The resulting species mass fractions (Y_k) and temperature (T) time evolutions have been compared with the ones resulting from the CFD simulations in two cases:

- Closed system where time is the only independent variable (PSR)
- Reacting flow with constant properties and no diffusion of species (PFR)

In both cases, the equations solved by FASTEST-3D are equivalent to the ones solved in the SENKIN code (equations 3.1). The equivalence between the perfectly stirred reactor and

the plug-flow reactor with constant properties is achieved through the change of variable $x = u \cdot t$ and eliminating the spatial diffusion of species and temperature. The density and the velocity are constant along the reactor. As $u = 1$ in the whole burner, the evolutions in time for the PSR and in space for the PFR have to be coincident. A first-order fully implicit algorithm has been chosen for the time integration.

3.1.1. Simulation of the perfectly stirred reactor configuration

The results of the FASTEST-3D calculation can be seen in figures 3.4 and 3.5.

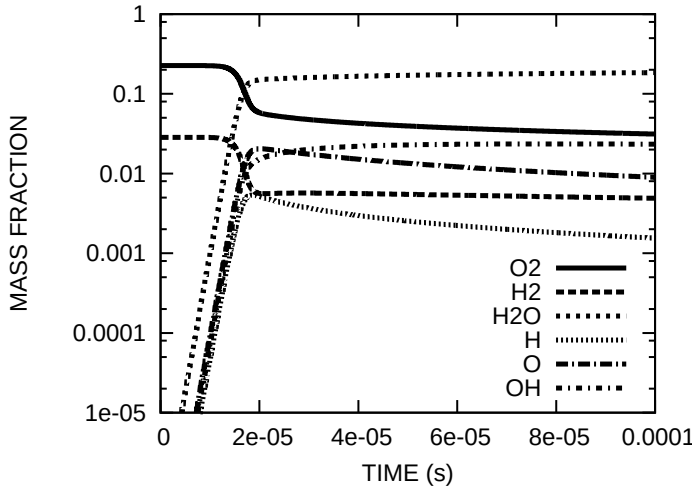

Figure 3.4.: Species evolution in stoichiometric H_2 combustion given by FASTEST-3D for the perfect stirred reactor configuration

These figures show almost identical profiles to the ones given by the reference calculation (figures 3.2 and 3.3). The temperature given by the FASTEST-3D calculation after $10^{-4}s$ (2501K) reproduces with very good accuracy the value obtained from the SENKIN calculation (2564K). The same can be said about the mass fractions of the main species. This proves the validity of the implementation for the calculation of a simple geometry like the perfectly stirred reactor.

3.1.2. Simulation of the plug-flow reactor configuration

The configuration in this case corresponds to the definition of the plug-flow reactor.

Table 3.1 shows the different configurations that have been simulated to evaluate the influence of the CFL number in the simulation of the plug-flow reactor. The results can be seen in Figures 3.6 to 3.11, where the species concentrations along the reactor, as well as the temperature profiles have been plotted.

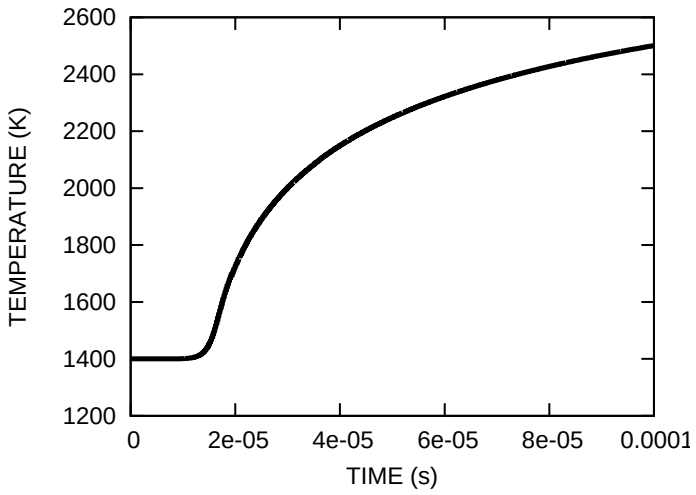

Figure 3.5.: Temperature evolution in stoichiometric H_2 combustion given by FASTEST-3D for the perfect stirred reactor configuration

Table 3.1.: Parameters for the study of CFL influence in the H_2-mechanism

	1	2	3	4	5
Δt $(\times 10^{-6})$ s	10	2	1	0.1	0.1
Δx $(\times 10^{-6})$ m	2	2	2	0.4	1
CFL	5	1	0.5	0.25	0.1

It has been previously mentioned that the reference profiles are represented in figures 3.2 and 3.3, which show the evolution in a perfectly stirred reactor configuration given by the SENKIN code.

One can observe in figures 3.6 to 3.10, that in all cases ignition starts earlier than in the reference simulation, and that the reactions are slower (closer to the reference) for smaller scaling factors. Only in the case of configurations 4 and 5 (figures 3.9 and 3.10) the species profiles separate from the origin in a similar way to the curves in the reference simulation. These configurations happen to be the finest ones and so, it can be concluded that the grid size has a bigger influence than the CFL number in the accuracy of the results.

One can see in figures 3.9 and 3.10, that the profiles do not reach the right limit of the x-axis, where $x = 1 \times 10^{-4} m$. The scaling factors in these two cases are smaller than in the other six configurations and the size of the computational domain in flow direction corresponds to $x = 2 \times 10^{-5} m$ for figure 3.9 and $x = 5 \times 10^{-5} m$ in the case of figure 3.10. However, the axis scale has been kept the same to simplify the comparison with the reference curves and the other simulations.

Figure 3.11 shows the temperature evolution along the reactor for all the 5 configurations

under study as well as the reference calculation. Curves 4 and 5 show the best agreement with the reference curve. These are also the simulations with the finest meshes. Curves 2 and 3 show very similar behaviour. Both present the largest slopes ($\Delta T/\Delta x$) at the origin and remain above the reference curve all along the reactor. Curve 1, on the other hand, shows a lower initial slope and crosses the reference curve to remain below it until the end of the computational domain. All curves seem to tend asimptotically to the reference temperature profile.

The results have shown that the finest grid resolutions give the best agreement with the reference profiles. When the spacial discretization is kept constant, the size of the time step influences the speed at which species are formed or consumed, as it can be seen by comparing figures 3.6, 3.7 and 3.8.

The next step is the evaluation of the influence of the temporal discretization scheme on the results. This will be shown in section 3.2.

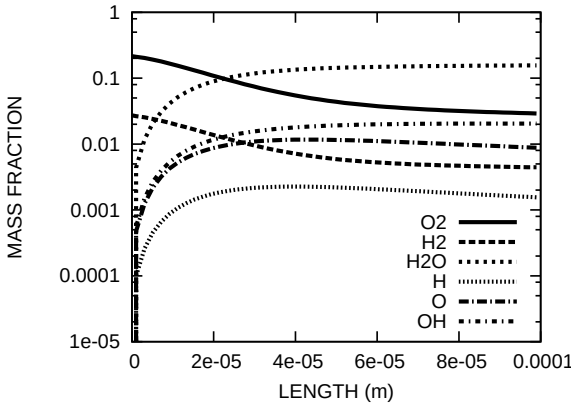

Figure 3.6.: 1D-Simulation of H_2 combustion. Species concentration along reactor length. Configuration 1: CFL = 5

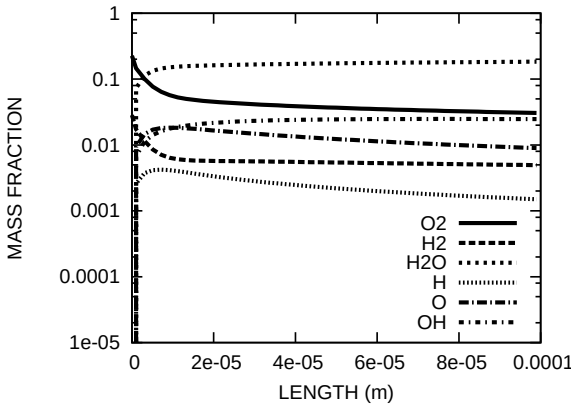

Figure 3.7.: 1D-Simulation of H_2 combustion. Species concentration along reactor length. Configuration 2: CFL = 1

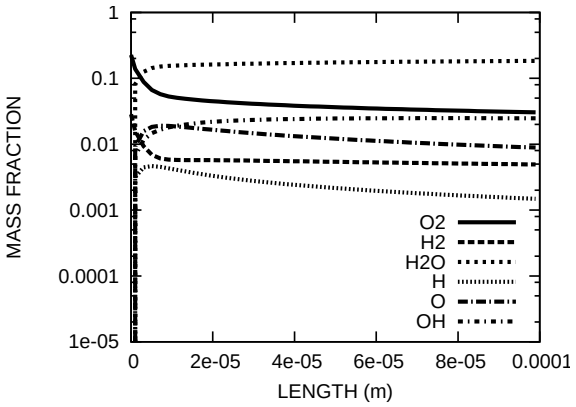

Figure 3.8.: 1D-Simulation of H_2 combustion. Species concentration along reactor length. Configuration 3: CFL = 0.5

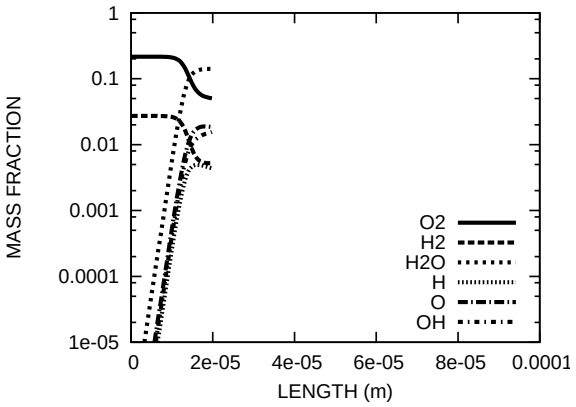

Figure 3.9.: 1D-Simulation of H_2 combustion. Species concentration along reactor length. Configuration 4: CFL = 0.25

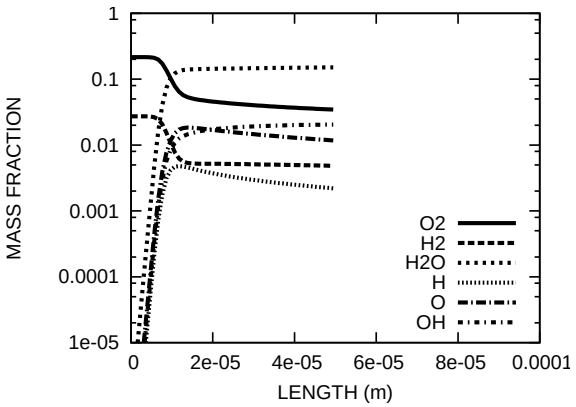

Figure 3.10.: 1D-Simulation of H_2 combustion. Species concentration along reactor length. Configuration 5: CFL = 0.1

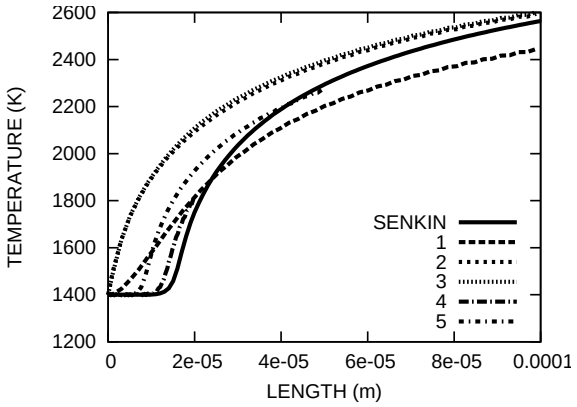

Figure 3.11.: 1D-Simulation of H_2 combustion. Temperature along reactor length for all 5 variants and reference profile

3.2. Stoichiometric — $CH_4 - air$ combustion

Methane is important for electrical generation by burning it as a fuel in a gas turbine or steam boiler. Compared to other hydrocarbon fuels, burning methane produces less carbon dioxide for each unit of heat released. At about 891 kJ/mol, methane's combustion heat is lower than any other hydrocarbon; but a ratio with the molecular mass (16.0 g/mol) divided by the heat of combustion (891 kJ/mol) shows that methane, being the simplest hydrocarbon, produces more heat per mass unit than other complex hydrocarbons.

Methane is the main component of natural gas. This is one of the most popular fuels for residential heating and is currently piped in many countries for domestic heating and cooking purposes. According to the AGA [1], 51 percent of heated homes in the U.S. (or 49.1 million households), used natural gas heating in 2000. Natural gas is considered to have an energy content of $39MJ/m^3$.

Regarding the simulation of methane combustion, there are numerous kinetic mechanisms available in the literature, which accurately describe the combustion of the mixture methane-air. One of the most famous among them is the Gri-Mech mechanism, consisting of 53 species and 325 reversible reactions.

Methane-air combustion has thus been included in the present work because of its importance as fuel and particularly for heating purposes, the availability of kinetic data and the abundance of experimental and computational data.

The simulation of methane combustion has been performed by feeding the methane-air mechanism (see Appendix A.2) in the SENKIN code. The results for species and temperature evolution in time can be seen in figures 3.12 and 3.13.

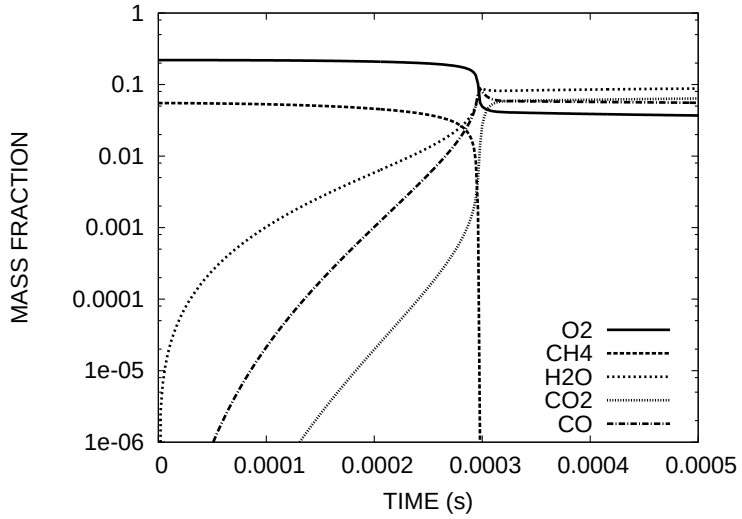

Figure 3.12.: Species evolution in stoichiometric CH_4 combustion given by SENKIN

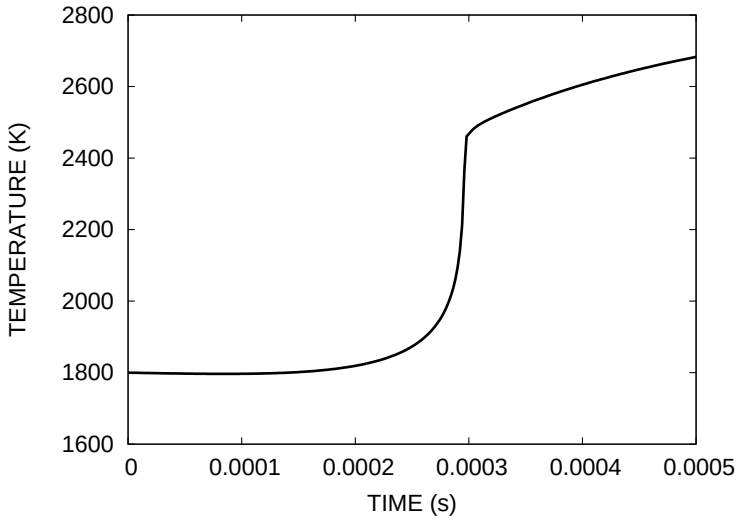

Figure 3.13.: Temperature evolution in stoichiometric CH_4 combustion given by SENKIN

In this case, the initial mixture presents stoichiometric concentrations, $Y_{CH_4} = 0.055$, $Y_{O_2} = 0.220$ and $Y_{N_2} = 0.725$ and ignition is achieved by setting the temperature at 1800K. Ignition starts after approximately $2.8 \times 10^{-4}s$ and the final temperature after $2 \times 10^{-4}s$ is approximately 2800K, which is a very high value. It must be considered, however, that this is not a real flame but an ideal stoichiometric combustion where time is the only variable, where no heat transfer to the surroundings is present, obviously without any coflow and where the initial temperature is 1800K

3.2.1. Simulation of the plug-flow reactor configuration

These results have been compared with the ones obtained by using the coupling of FASTEST-3D and CHEMKIN for the one-dimensional case of methane combustion in a plug-flow reactor. In these simulations, like in the ones described previously for H_2 combustion, the density of the mixture is kept constant and the diffusion coefficients of the different species and temperature conductivity are set to zero.

Different temporal discretizations have been tested in this case. They can be seen in table 3.2.1 together with the grid spacing for each simulation. The initials in the table correspond to:

- First-order fully implicit — fofi
- Crank - Nicolson — crni
- Second-order fully implicit — sofi

The condition for the CFL number has been fixed for all the five cases: $CFL = 1$. Velocity remains as well constant all along the reactor ($u = 1$), and this way the time step of each simulation has the same value as the grid spacing.

Table 3.2.: Parameters for the study of influence of the time discretization and grid spacing in the CH_4-mechanism

	1	2	3	4	5
$\Delta x[m]$	1×10^{-6}	1×10^{-6}	1×10^{-6}	1×10^{-5}	1×10^{-5}
Discretization	fofi	crni	sofi	fofi	crni

Figures 3.14, 3.15 and 3.16 show the concentrations of the main species along the burner for different discretization schemes. The reference profiles for these calculations are represented in figures 3.12 and 3.13, which show the evolution in time in a perfectly stirred reactor given by the SENKIN code.

From the observation of these results (3.14, 3.15 and 3.16) and comparison with the reference figures, it can be seen that the first-order implicit and the Crank-Nicolson discretizations (figures 3.14 and 3.15) match the reference curves with very good agreement.

Figure 3.17 shows the evolution of the temperature along the reactor for all three discretization schemes and for the reference calculation. As in the case of the species concentrations, the second-order implicit discretization shows the largest deviation from the reference among all three. The temperature curves corresponding to the first order implicit and the Crank-Nicolson discretizations are almost coincident with the reference curve, showing the accuracy of the implementation when a very fine mesh is used.

To find out the influence of the grid spacing in the simulation of $CH_4 - air$ combustion, the scaling factor and the time step have been increased. The CFL nummber is still equal to 1 but the resolution is ten times lower than in the previous configuration.

The results can be seen in figures 3.18 and 3.19. Again both schemes yield almost identical evolution of the main species along the reactor. However, the deviation from the reference profiles is in this case larger. Ignition starts earlier and the reactions are slower. This effect could be observed as well in section 3.1.2 in the case of $H_2 - air$ combustion in a plug-flow rector.

These simulations together with those of H_2 combustion show the feasibility of simulating 1-dimensional reacting flows with a 3-dimensional code like FASTEST-3D. The influence of temporal discretization, grid spacing and CFL number has been studied. The species concentrations at the end of the reactor reproduce very closely those from the reference simulation even for the cases where the deviation with the reference solution is very large. That means that, in the worst case, this approach is as accurate as the equilibrium model.

Three different temporal discretization schemes have been compared. First-order implicit and Crank-Nicolson schemes provide the results that better match the reference calculations and any of both can be used for calculation of the 2D configurations shown in the next section.

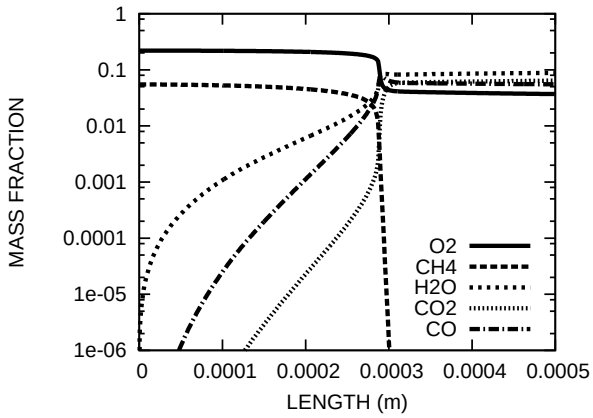

Figure 3.14.: 1D-Simulation of CH_4 combustion. Species concentration along reactor length. Configuration 1: First-order implicit discretization. $\Delta x = 1 \times 10^{-6} m$

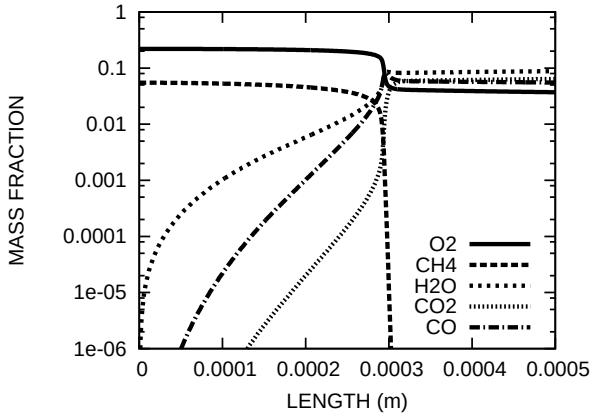

Figure 3.15.: 1D-Simulation of CH_4 combustion. Species concentration along reactor length. Configuration 2: Crank-Nicolson implicit discretization. $\Delta x = 1 \times 10^{-6} m$

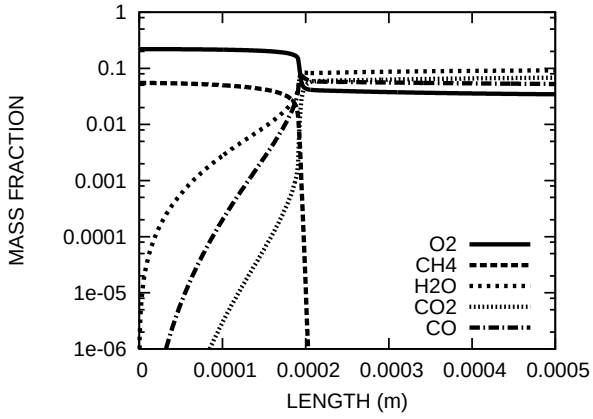

Figure 3.16.: 1D-Simulation of CH_4 combustion. Species concentration along reactor length. Configuration 3: Second-order implicit discretization. $\Delta x = 1 \times 10^{-6} m$

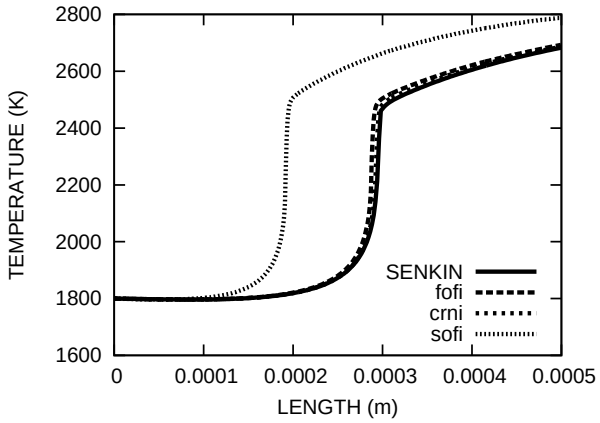

Figure 3.17.: 1D-Simulation of CH_4 combustion. Temperature of the mixture along reactor length. Configuration 3: Crank-Nicolson discretization. $\Delta x = 1 \times 10^{-6} m$

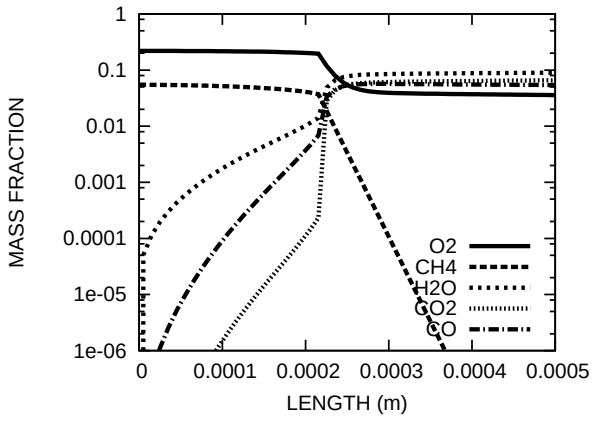

Figure 3.18.: 1D-Simulation of CH_4 combustion. Species concentration along reactor length. Configuration 4: First-order implicit discretization. $\Delta x = 1 \times 10^{-5} m$

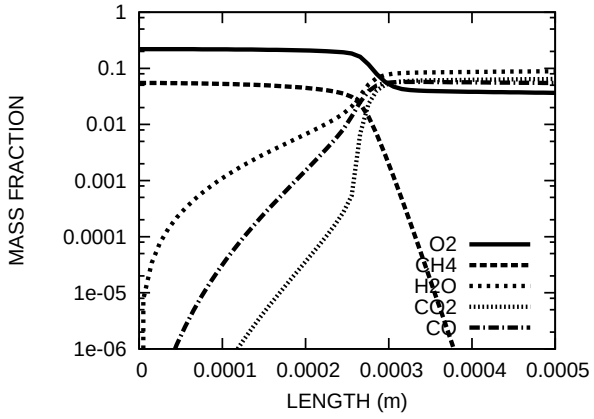

Figure 3.19.: 1D-Simulation of CH_4 combustion. Species concentration along reactor length. Configuration 5: Crank-Nicolson discretization. $\Delta x = 1 \times 10^{-5}$

4. 2D-Simulations

The following configurations represent real burners in which 2D or 2D axisymmetrical assumption can be made. These include laminar jets, burners and micro-burners. For the sake of simplicity and to ensure a faster and easier convergence of the simulation, the density has been kept constant in the first three cases. Because of this, results can be only qualitatively compared with the experimental measurements made in field or with the literature. Other variables like thermal conductivity, viscosity or diffusion coefficients are temperature dependent in these 2D simulations.

For the simulation shown in section 4.3.1, density changes have been allowed according to the ideal gas equation (2.8), but with an underrelaxation factor in order to allow only small variations of the density after each iteration. This has been done in order to enhance the stability of the code. The density in one control volume corresponds this way to the temperature in the cell only several time steps after this has reached its final value, i.e. all variables in the cell are in steady state.

The transport model is a simple one that considers each of the species dissolved only in the carrier gas (N_2). The diffusion coefficients D_k are expressed as functions of the temperature (T) and the absolute pressure (P) in the form:

$$D_k = f(T) = (a_1 + a_2 T + a_3 T^2 + a_4/T)\frac{1}{P} \tag{4.1}$$

where the coefficients a_{kj} are obtained from the CHEMKIN transport database using the subroutine package TRANS and the CHEMKIN properties library.

For verification purposes, the same configurations have been simulated with the comercial code FLUENT. These simulations have been performed on computational models with similar number of elements and boundary conditions, and with the same chemical mechanisms than the ones performed with FASTEST-3D / CHEMKIN.

FLUENT's stiff chemistry solver has been used to calculate species reaction rate through the CHEMKIN reaction mechanism. Unfortunatelly, this model can only be used when the ideal gas model is activated and, therefore, differences may arise with simulations performed under constant density assumption.

4.1. Hydrogen Combustion

The chemical scheme for $H_2 - air$ combustion is the one by Miller et al. [46] and can be found in appendix A1. It includes 9 species: H_2, H, O_2, O, OH, HO_2, H_2O_2, H_2O, N_2 and 18 reactions. The chemical mechanism provides, for each reaction, the stoichiometric coefficient of each species involved and the Arrhenius coefficients: A_j (cgs units), β_j and E_j (cal/mole). The following configurations have been simulated to verify the results provided by FASTEST-3D with this mechanism when simulating two dimensional geometries.

4.1.1. H_2 Micro-Combustor

This micro-combustion reactor has been developed and calculated at the Nagoya University by Y. Nakamura and A. Kubota [60]. The purpose of this simulation is to verify the capability of the coupling FASTEST-3D / CHEMKIN to simulate a 2D axisymmetric diffusion flame under simplified conditions. These are:

- Symmetric configuration
- Adiabatic conditions
- Reduced $H_2 - air$ combustion mechanism (see appendix A1) and species transport mechanism (as described in section 2.3)
- Constant material properties (density and viscosity) of the gas mixture

4.1.1.1. Configuration under study

The geometry and boundary conditions can be seen in figure 4.1. The grid resolution and boundary conditions of the model are presented in more detail in table 4.1, where Nx and Ny represent the number of grid points in radial and axial direction respectively.

Since all the transport and chemical phenomena are symmetric respect to the burner center axis, the numerical domain is considered to be 2-D axisymmetric. A nozzle, whose inner and outer diameters are $0.3mm$ and $0.8mm$ respectively ejects hydrogen upward (against the gravity vector). Inside the nozzle, the radial distribution of the axial velocity corresponds to a fully developed laminar profile with a peak velocity of $2.0m/s$. A micro-diffusion flame is established over the burner steadily with a few millimeters flame height. The burner is kept at room temperature to introduce some heat loss in the system and avoid any catalytic effect at the walls. It can be seen in figure 4.1 that the interior of the burner has been included in the numerical domain so that "back diffusion" of the species inside the burner is possible.

The ordinary set of the conservation equations (mass, momentum, energy, species) and the equation of state are solved numerically by the finite volume method. The evolution of temperature and species mass fractions is calculated by the chemical kinetic code. Thermal

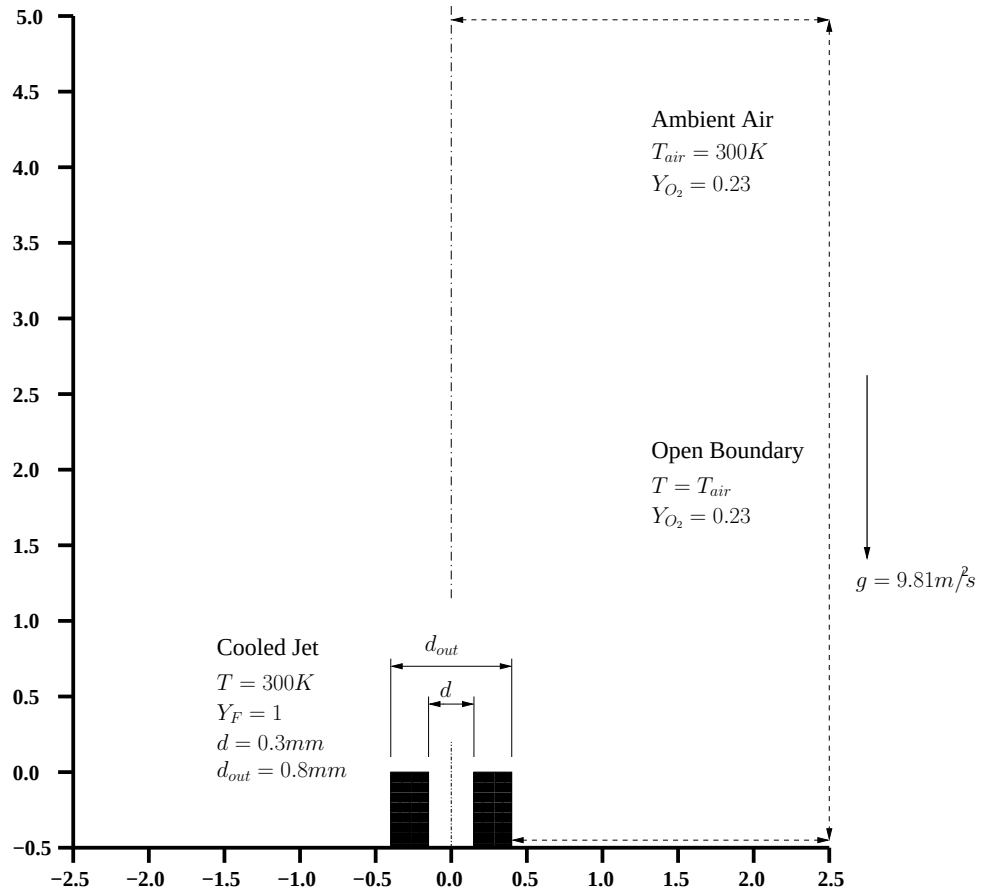

Figure 4.1.: Configuration of the micro-combustor (units in millimeters). Because of symmetry reasons, the computational model includes one half of this configuration.

and transport properties are given by the CHEMKIN database. Open boundary conditions are imposed at the boundaries except for the center axis (symmetry). The non-slip boundary condition is applied at the burner surface.

The velocity in the nozzle corresponds to a fully developed laminar profile with a peak velocity of $2m/s$. The Reynolds number is equal to 3.6 and the flow is thus laminar.

Both geometrical models (the one for FASTEST-3D and the one for FLUENT) have identical number of cells and the similar boundary conditions. However, Fluent solves 2D-axisymmetric equations whereas FASTEST-3D solves 3D cartesian equations. This may be the cause of some small deviation in the results.

4.1.1.2. Simulation results

Figures 4.2 to 4.8 show the results obtained for velocity, temperature and some relevant species concentration from the simulations of this configuration.

The results of the FASTEST-3D simulation can be seen at the top of the page while the

Table 4.1.: Boundary conditions and grid resolution for Nagoya configuration

	u_{max} (m/s)	p_{rel} (Pa)	T (K)	Y_i	Grid Points
INLET	2.0	-	300	$Y_{H_2} = 1.0$	Nx = 6
OUTLET [1]	-	0.0	300	$Y_{O_2} = 0.23$ $Y_{N_2} = 0.77$	Nx = 51 Ny = 87
NOZZLE	-	-	300	-	Ny = 12
SYMMETRY	-	-	-	-	Ny = 87

results of the FLUENT calculation are at the bottom. The nozzle is in both cases at the bottom and the symmetry axis at the left hand side of the picture.

The figures show some differences between both simulations. The mechanical behaviour of the jet is similar in both cases, as it is shown by 4.3. The peak velocity is slightly higher in the case of Fluent, which is due to the effect of the density variation with the temperature.

Figure 4.2 shows a comparison between the results obtained from FLUENT and FASTEST-3D for the temperature profile along the symmetry axis. FASTEST-3D does not reproduce the temperature peak that can also be found in the literature [60] while FLUENT does capture it.

These differences are more evident in Figure 4.4, which shows the temperature profiles for both calculations. The species concentration profiles show also large differences in the distribution of the main species, although there is a certain qualitative agreement and the species mass fraction values are mostly in the same order of magnitude for both calculations.

[1] The boundary conditions for temperature and species concentration apply only to reverse flow

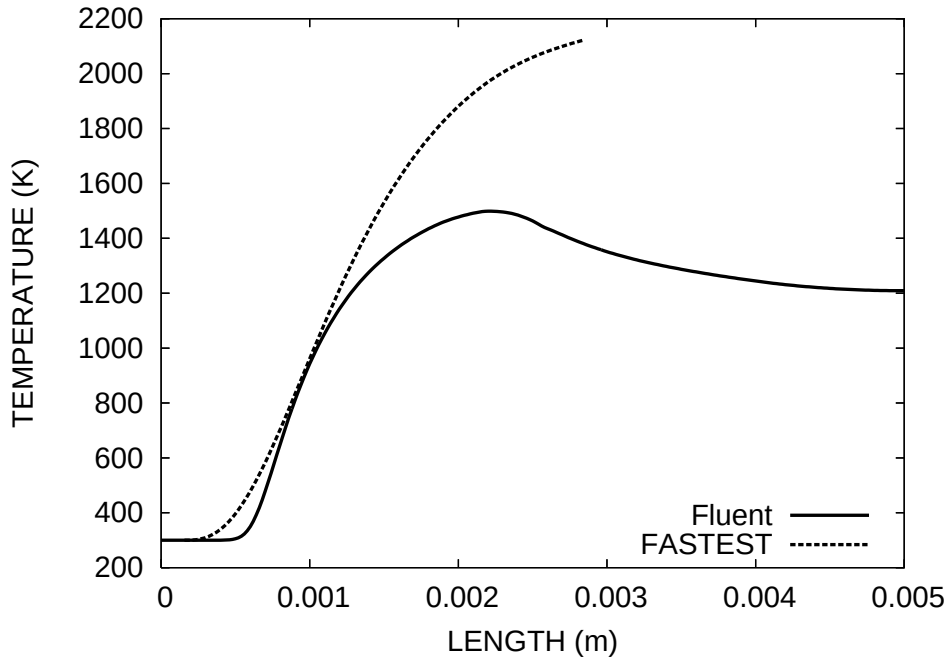

Figure 4.2.: Nagoya Micro-Combustor configuration. Temperature plots along the axis for FLUENT and FASTEST-3D simulations

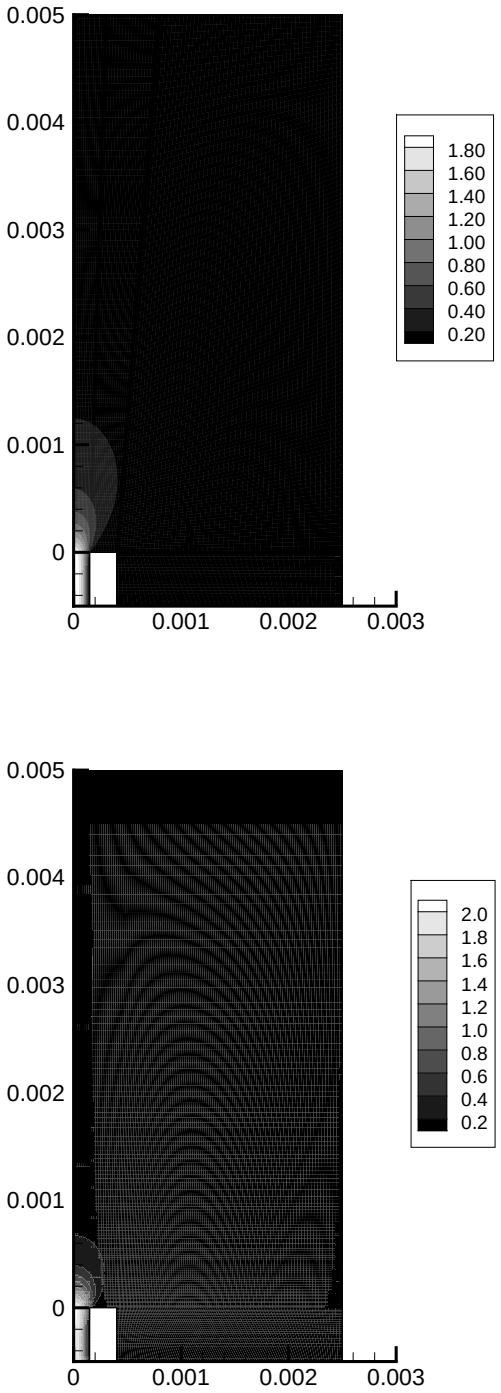

Figure 4.3.: Nagoya Micro-Combustor configuration. Velocity fields provided by FASTEST-3D at the top and FLUENT at the bottom

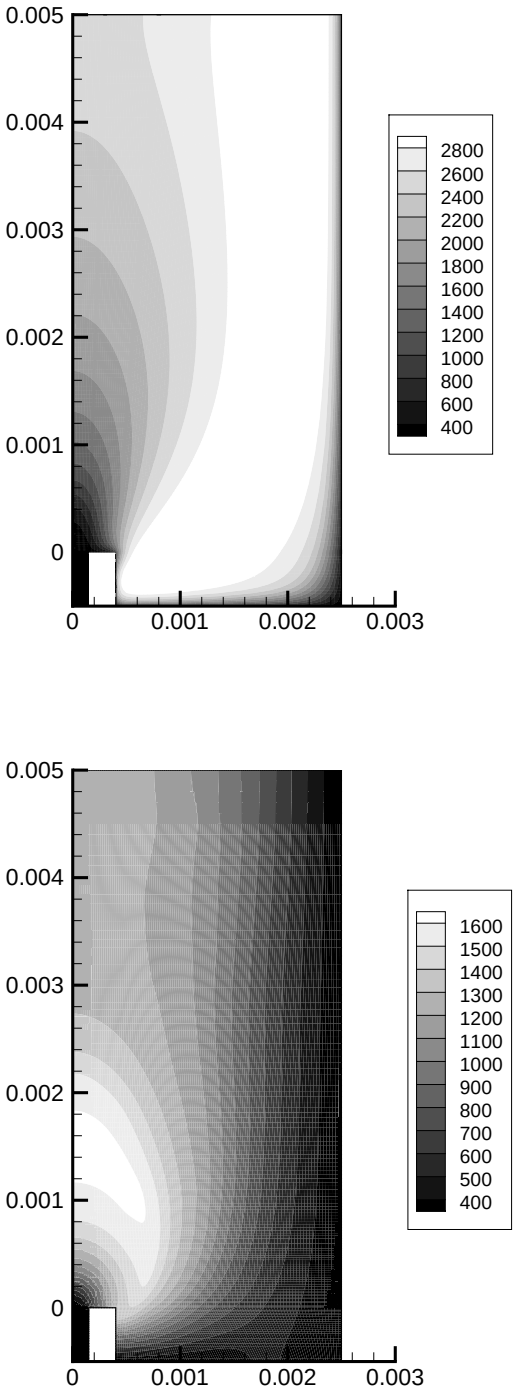

Figure 4.4.: Nagoya Micro-Combustor configuration. Temperature fields provided by FASTEST-3D at the top and FLUENT at the bottom

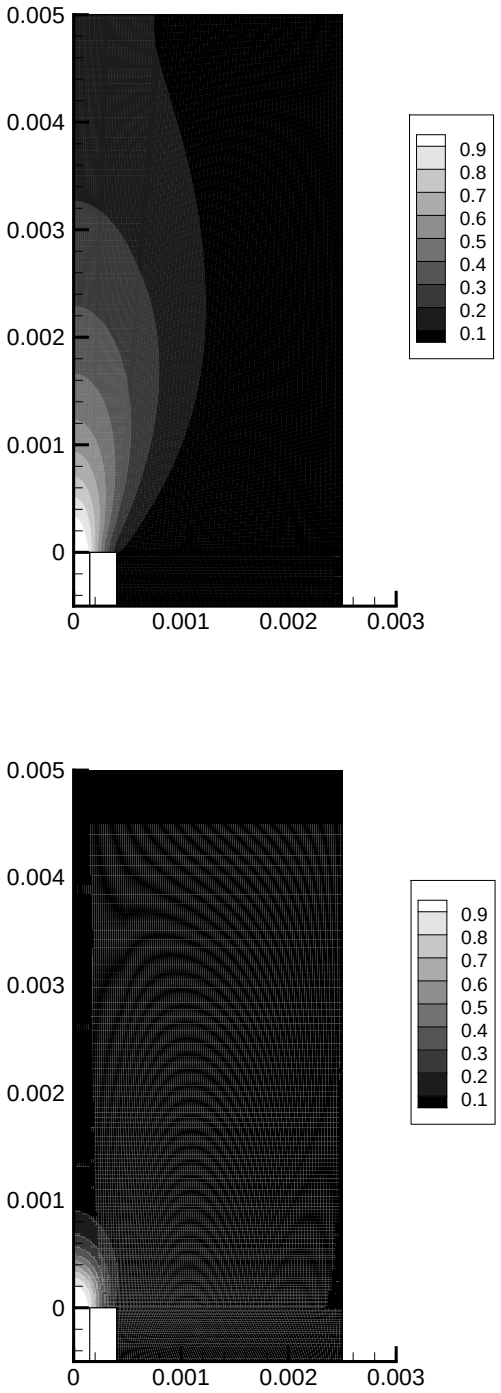

Figure 4.5.: Nagoya Micro-Combustor configuration. H_2 mass fraction fields provided by FASTEST-3D at the top and FLUENT at the bottom

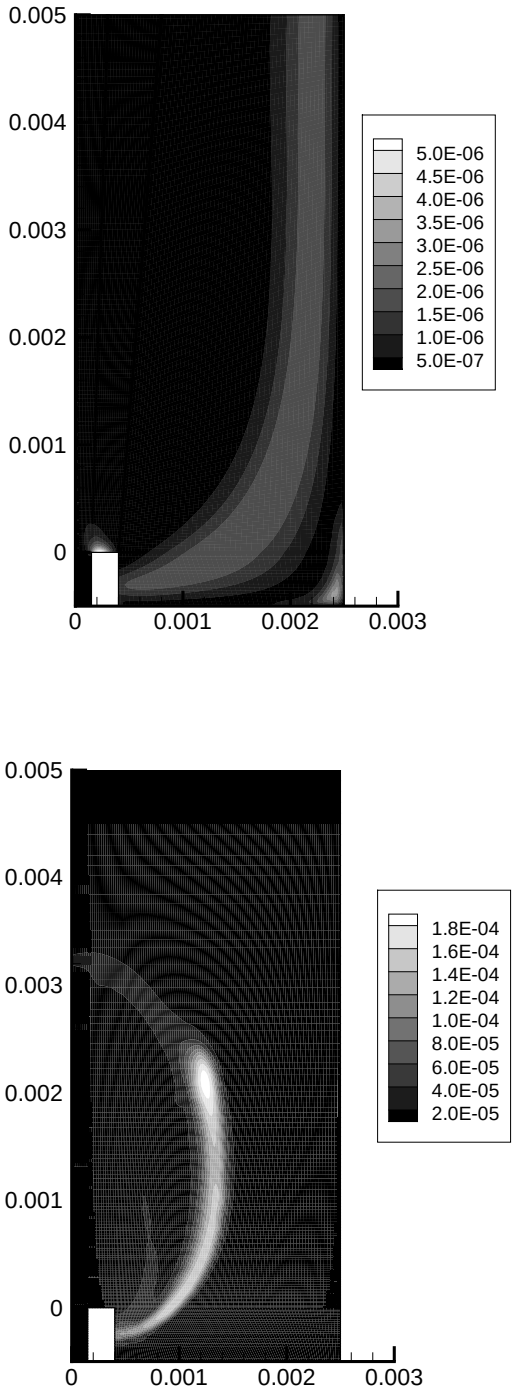

Figure 4.6.: Nagoya Micro-Combustor configuration. H_2O_2 mass fraction fields provided by FASTEST-3D at the top and FLUENT at the bottom

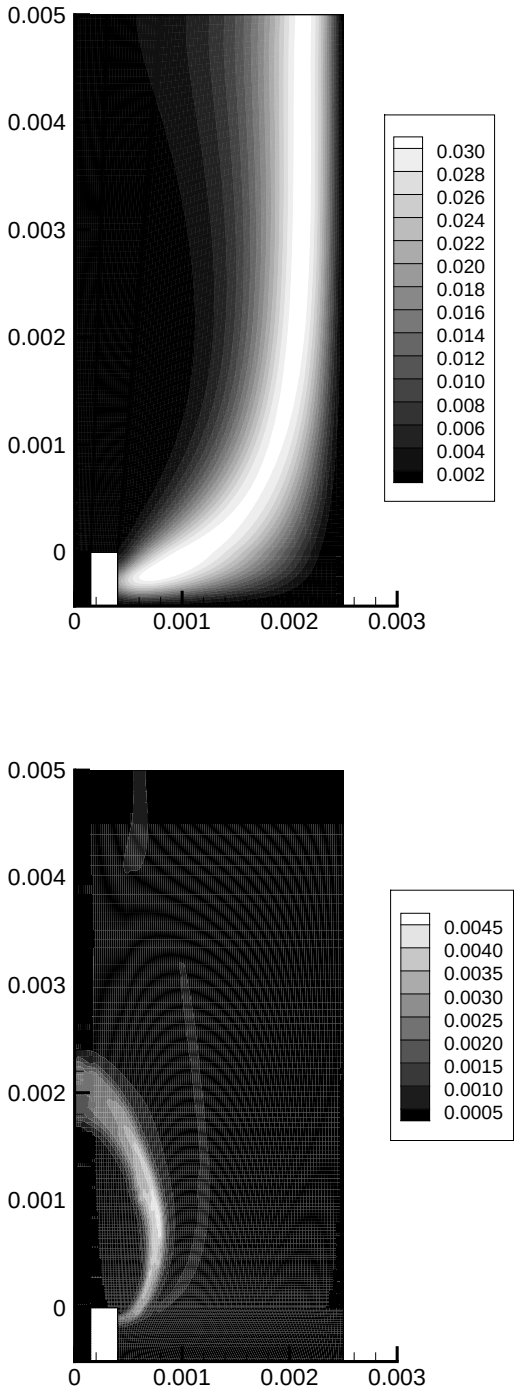

Figure 4.7.: Nagoya Micro-Combustor configuration. OH mass fraction fields provided by FASTEST-3D at the top and FLUENT at the bottom

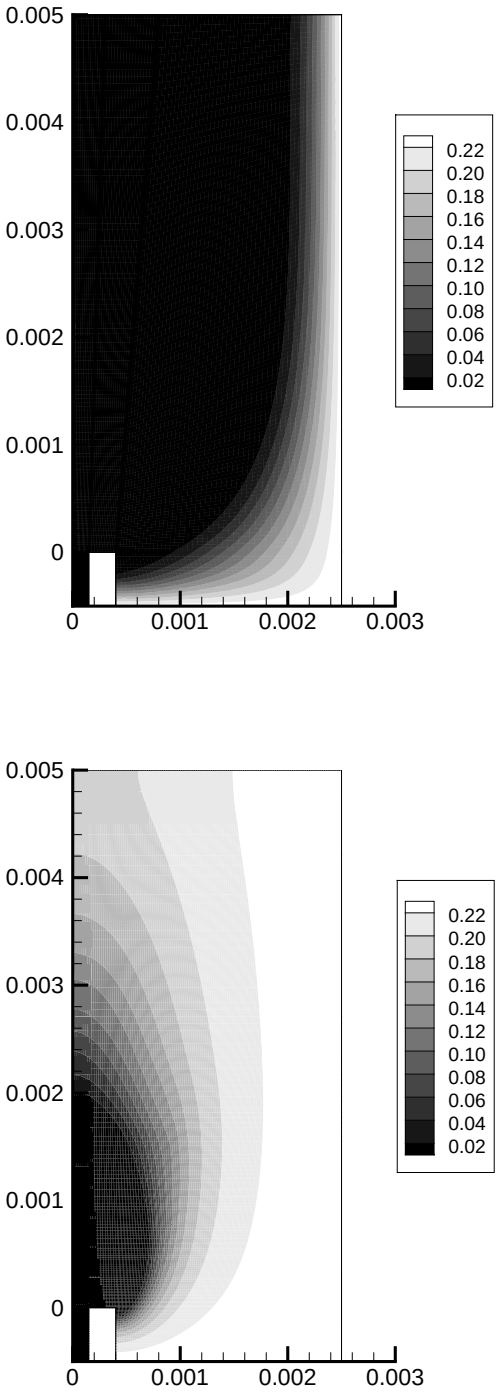

Figure 4.8.: Nagoya Micro-Combustor configuration. O_2 mass fraction fields provided by FASTEST-3D at the top and FLUENT at the bottom

4.1.2. H_2 Bunsen Burner

A second experimental configuration for $H_2 - air$ combustion included in the present work is the H_2-Bunsen burner simulated by Ern and Giovangigli in [23]. This configuration has been chosen because of its simplicity and the abundant information available in the literature regarding temperature and species distribution. The comparison between literature and calculation results will help validate the coupling of the chemical kinetic package CHEMKIN and the CFD code FASTEST-3D.

4.1.2.1. Configuration under study

The dimensions of the nozzle and the geometrical boundary conditions have been described in figure 4.9.

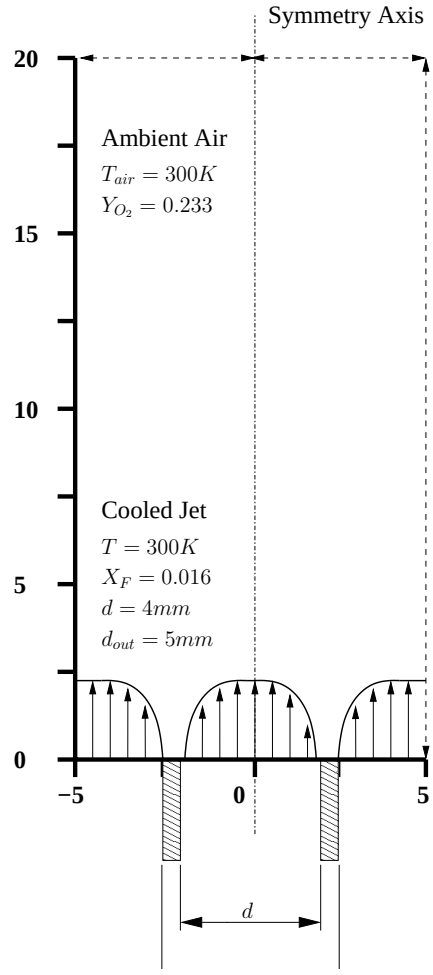

Figure 4.9.: Configuration of the Bunsen burner. Because of symmetry reasons, only half of the real geometry has been considered in the computational model.

The flame is obtained by letting a lean mixture of hydrogen and air flow into the domain represented in the same figure. The volumetric concentration of hydrogen amounts to 20%, the temperature of the mixture is 300K and the burner operates at atmospheric pressure. The combustion mechanism for $H_2 - air$ combustion and the transport scheme are the same ones used in the previous configuration.

The flow is of plug type and the flame is surrounded by a coflow of air. The bulk velocity in both flows is $u_{inj} = 3m/s$. These values correspond to a Reynolds number of approximately 700 for the present configuration and the flow is, thus, laminar.

More specifically, denoting by $r_0 = r_i + \omega$ the outer diameter of the nozzle, the inflow velocity is equal to:

$$u^{in}(r)/u_{inj} = 1 - \exp(-(r_i - r)/\delta) \text{ for } 0 \leq r \leq r_i,$$

$$u^{in}(r)/u_{inj} = 0 \text{ for } r_i \leq r \leq r_o$$

and

$$u^{in}(r)/u_{inj} = 1 - \exp(-(r - r_0)/\delta) \text{ for } r_0 \leq r,$$

where δ is the gradient parameter chosen to be $\delta = 0.5mm$. These boundary conditions together with the grid resolution are summarized in table 4.2 where Nx and Ny represent the number of grid points in radial and axial direction.

4.1.2.2. Simulation results

The results obtained in this case can be seen in figures 4.10 to 4.16. At the top of the page one can find the results of the FASTEST-3D simulation and, at the bottom, the ones from the FLUENT simulation. The nozzle is located, in both cases, at the bottom of the figure while the symmetry axis is represented by the vertical edge at the left hand side of the figure.

In this case the results show much better agreement with literature values than in the previous configuration. Velocity, temperature and species concentration fields are very close in both simulations and also when compared with the results found in the literature (see [23]).

Some of the differences can be explained by the fact that the simulation in FASTEST-3D was performed under a condition of constant density. This leads to the lower velocity peak and the higher temperature maximum which, in this case, exceeds "only" by around one hundred degrees Celsius the maximum temperature predicted by FLUENT. The flame length obtained from the FASTEST-3D simualtion is shorter than the length provided by the FLUENT calculation. This can be due to the fact, that FASTEST-3D calculates with constant density but also to the errors from the splitting algorithm. We have observed in

[2]The boundary conditions for temperature and species concentration apply only to reverse flow

Table 4.2.: Boundary conditions and grid resolution for Bunsen burner configuration

	$u\ (m/s)$	$p_{rel}\ (Pa)$	$T\ (K)$	Y_i	Grid Points
INLET	$u^{in}(r)$	-	300	$Y_{H_2} = 0.017$ $Y_{O_2} = 0.229$ $Y_{N_2} = 0.754$	Nx = 50
COFLOW	$u^{in}(r)$	-	300	$Y_{O_2} = 0.233$ $Y_{N_2} = 0.767$	Nx = 28
OUTLET [2]	-	0.0	300	$Y_{O_2} = 0.233$ $Y_{N_2} = 0.767$	Nx = 93 Ny = 150
NOZZLE	-	-	300	-	Nx = 15
SYMMETRY	-	-	-	-	Ny = 150

section 3.1 how the reactions start earlier downstream when grids are coarser.

The temperature peak reaches 2100K in the FASTEST-3D simulation, while in the one performed with the code FLUENT it goes up to 1920K. The value given in the literature [23] is 1732K, which is quite far below the other two.

In the case of intermediate species FASTEST-3D shows a better agreement with the literature values. In the case of H_2O_2, for example, the molar fraction goes up to 5.5×10^{-5}, FLUENT gives 1.23×10^{-4} and in [23] we find a value of 4.01×10^{-5}. OH concentrations 4.15 are very similar in all the three simulations.

It can be seen in figures 4.13 to 4.16 that species diffusions are apparently larger in the FASTEST-3D simulation. This can only be due to differences in the diffusion coefficients used by both programs. FLUENT uses Fick's law for the species diffusion and its own transport library while FASTEST-3D takes the polynomial coefficients for the diffusion terms from the CHEMKIN transport database.

Figure 4.10 shows a comparison between the results obtained from FLUENT, the ones obtained from FASTEST-3D and the literature results [23] for the temperature profile along the symmetry axis. The FLUENT simulation shows a late ignition and very fast temperature increase to reach the highest temperature (almost 2000K). After this temperature peak, located $5mm$ downstream from the nozzle, the temperature slowly approaches the other two curves. The FASTEST-3D simulation shows the earliest ignition, probably due to the splitting errors (because of faster reactions when using coarse grids) but then behaves in a similar way to the curve given by the literature (Ern & al.) and the equilibrium values are very close for all three curves (specially FASTEST-3D and Ern & al.).

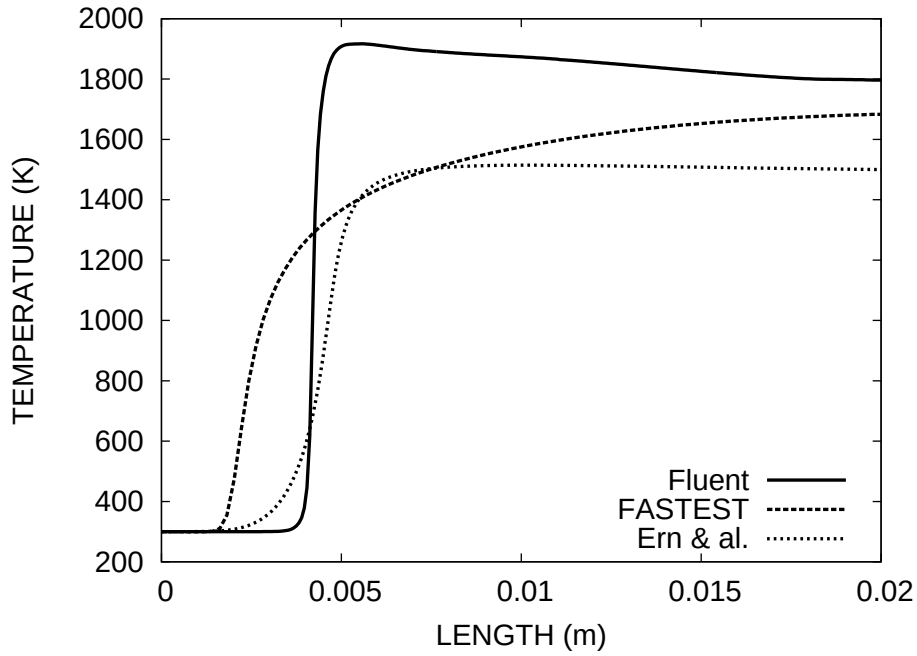

Figure 4.10.: Bunser burner configuration. Temperature plots along the axis for FLUENT and FASTEST-3D simulations

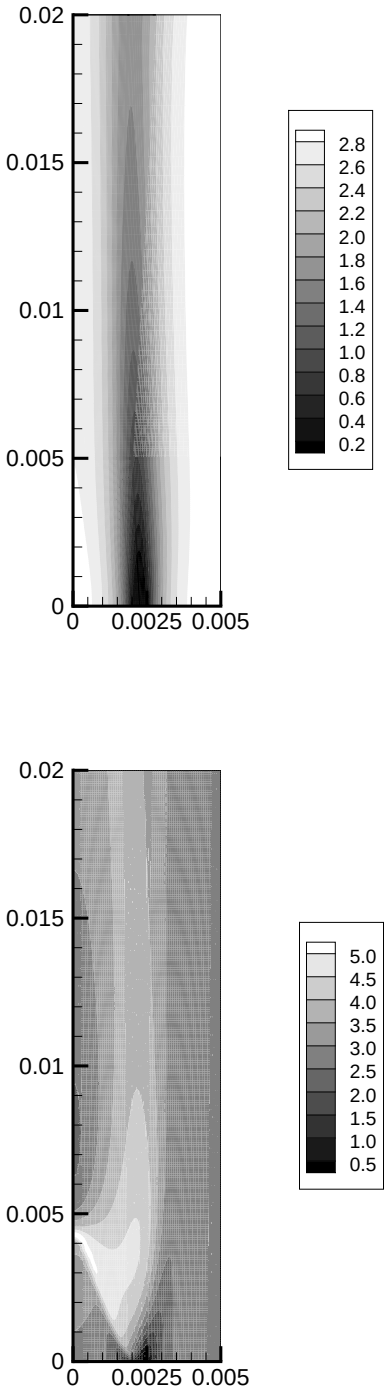

Figure 4.11.: Bunsen Burner configuration.
Velocity fields provided by FASTEST-3D at the top and FLUENT at the bottom

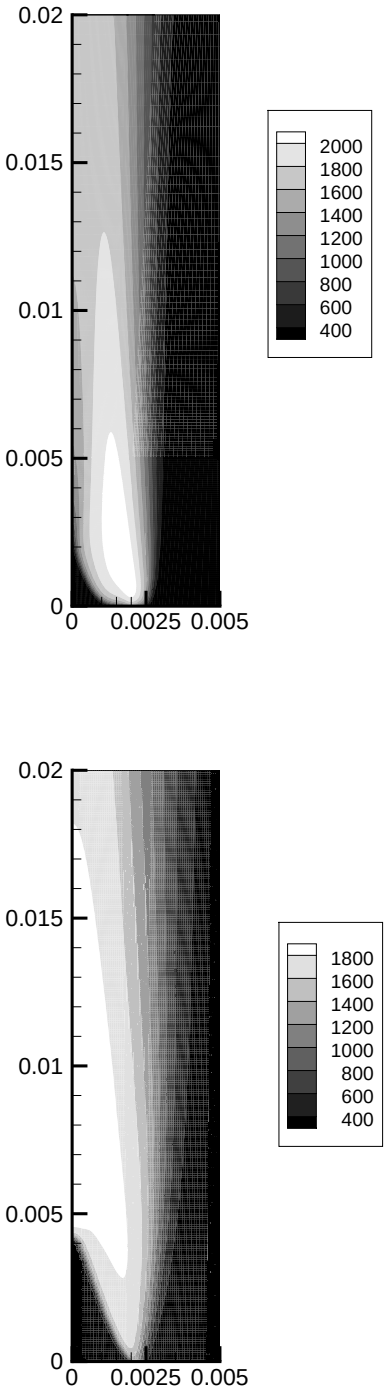

Figure 4.12.: Bunsen Burner configuration.
Temperature fields provided by FASTEST-3D at the top and FLUENT at the bottom

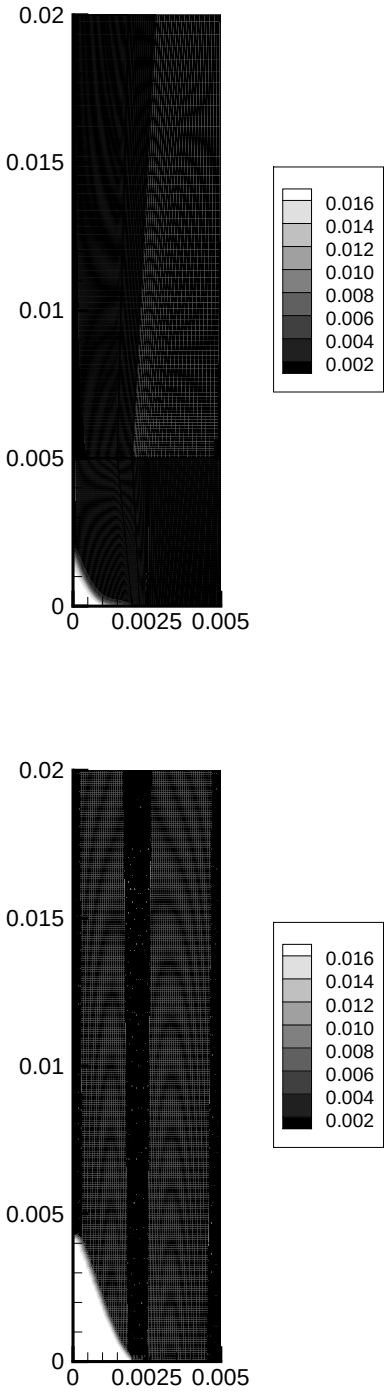

Figure 4.13.: Bunsen Burner configuration.
H_2 molar fraction fields provided by FASTEST-3D at the top and FLUENT at the bottom

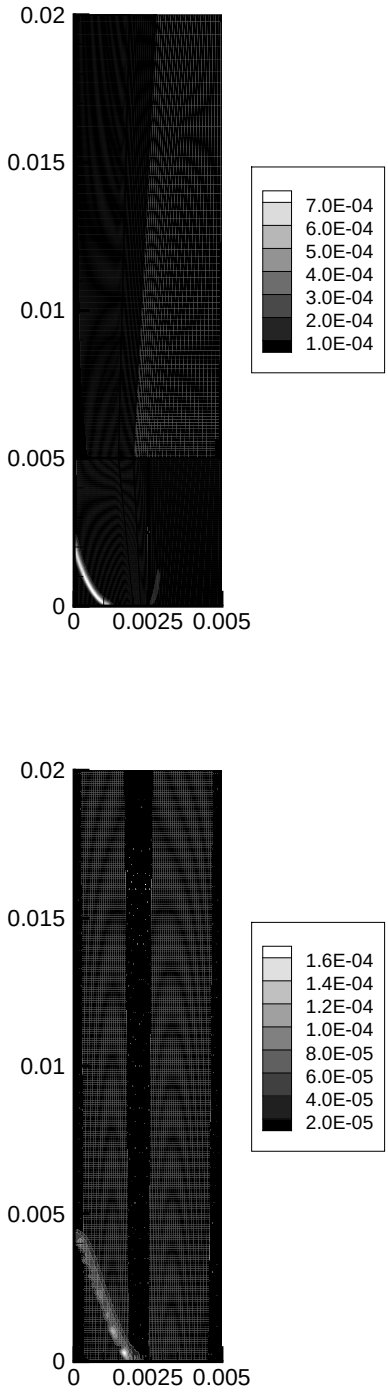

Figure 4.14.: Bunsen Burner configuration.
H_2O_2 molar fraction fields provided by FASTEST-3D at the top and FLUENT at the bottom

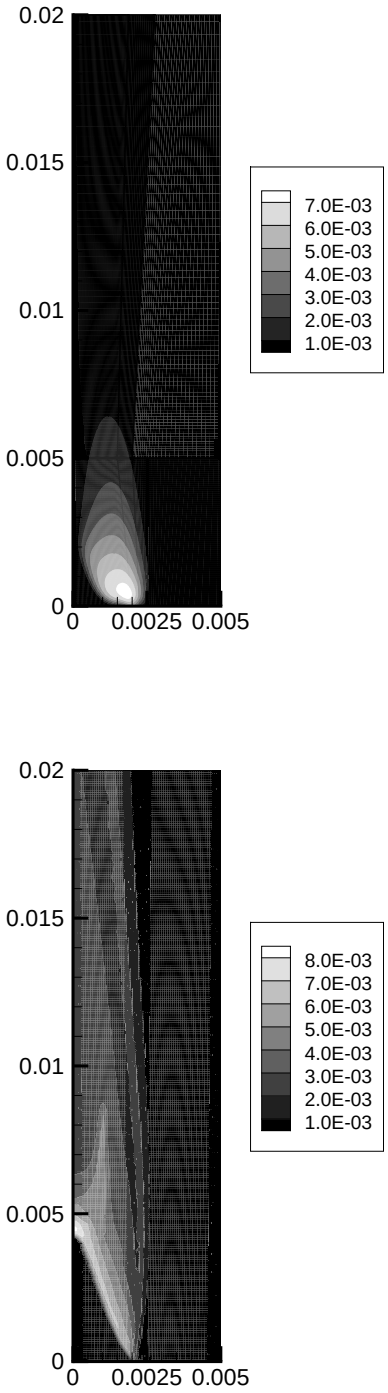

Figure 4.15.: Bunsen Burner configuration.
OH molar fraction fields provided by FASTEST-3D at the top and FLUENT at the bottom

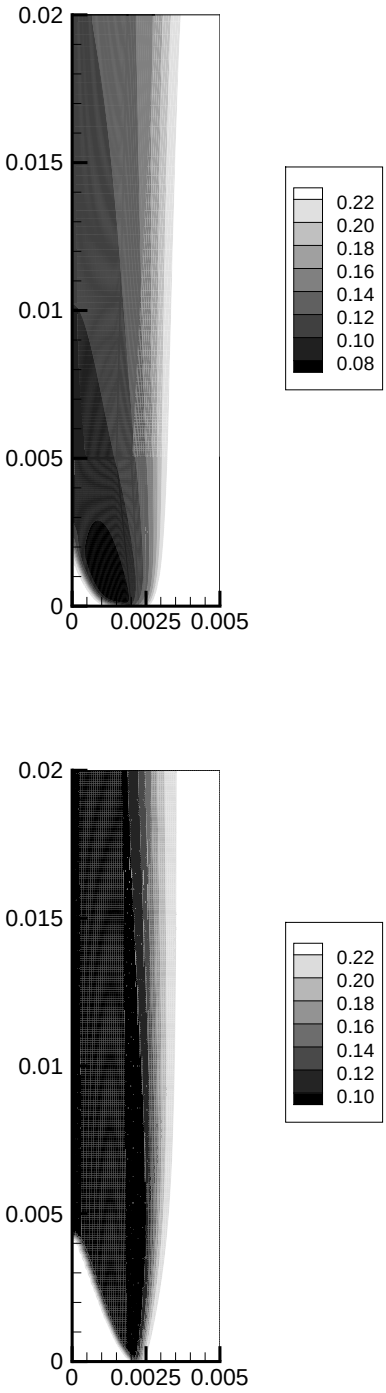

Figure 4.16.: Bunsen Burner configuration.
O_2 molar fraction fields provided by FASTEST-3D at the top and FLUENT at the bottom

4.2. Methane Combustion

In the former experiments we have assumed adiabatic conditions at the burner walls. In the following case we consider the effect of heat loss through the boundary walls. The importance of heat loss in the stabilization of a laminar flame in a burner can be therefore demonstrated. This experiment has already been numerically studied by Somers and De Goey [86], S. Paxion [68] and R. Baron [3].

4.2.1. Cold Wall Stabilized Methane Flame

4.2.1.1. Configuration under study

The configuration can be seen in figure 4.17. It consists of a burner fed with a stoichiometric mixture of air and methane and without any secondary flow.

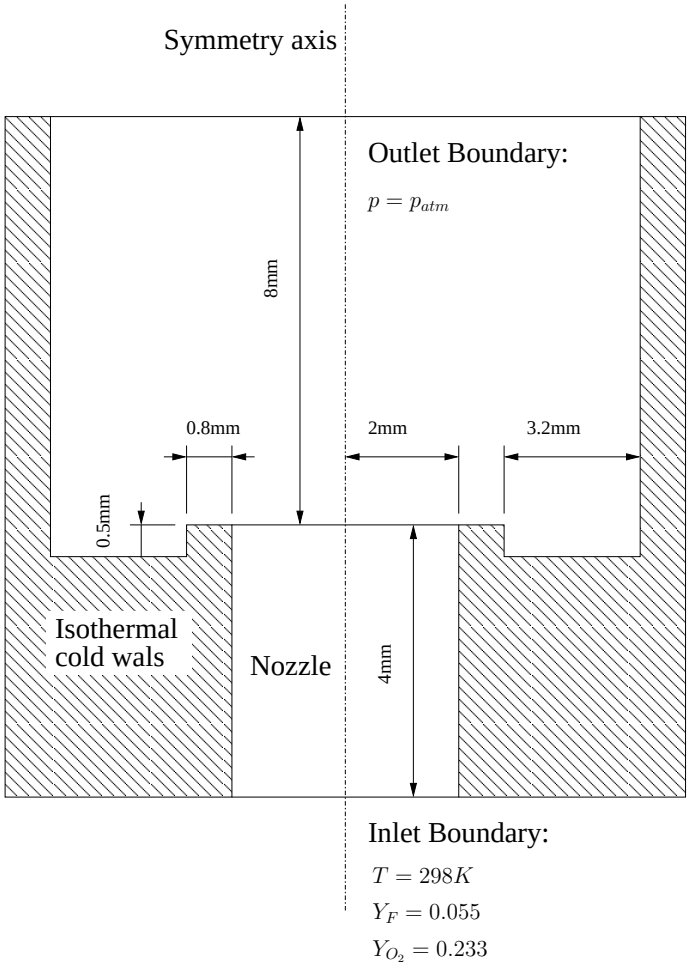

Figure 4.17.: 2D-Configuration used to analyze the importance of heat losses at the walls in the flame stabilization mechanism. Because of symmetry reasons, only the right half of the real geometry has been considered in the computational domain

Table 4.3.: Boundary conditions and grid resolution for the cold wall methane configuration

	$v\ (m/s)$	$p_{rel}\ (Pa)$	$T\ (K)$	Y_i	Grid Points
INLET	1.0	-	298	$Y_{CH_4} = 0.055$ $Y_{O_2} = 0.220$ $Y_{N_2} = 0.725$	Nx = 50
OUTLET[3]	-	0.0	298	$Y_{O_2} = 0.233$ $Y_{N_2} = 0.767$	Nx = 120
NOZZLE	-	-	298	-	Ny = 32
WALL	0.0	-	298	-	Nx = 70 Ny = 132
AXIS	-	-	-	-	Ny = 132

The heat losses at the injector walls produce a "fixing-effect", that prevents the flame from moving upstream close to the injector. The results obtained in complex chemistry with this configuration reproduce this situation by showing a completely detached flame.

The grid resolution and boundary conditions of the model can be seen in table 4.3. The velocity profile at the inlet is parabolic with a peak value of $1m/s$. This corresponds to a Reynolds number of approximately 150 and the flow is thus laminar. The walls are assumed to be at a constant temperature of 298K, which is as well the temperature of the mixture at the inlet.

4.2.1.2. Simulation results

Results for this configuration can be seen in figures 4.18 to 4.24. The ones obtained from FASTEST-3D are again at the top of the page, with the axis at the left of the picture while the profiles obtained from the FLUENT simulation can be seen at the bottom, with the symmetry axis also at the left hand side of the picture. The fuel in this case is CH_4 and the mechanism fed into CHEMKIN and FLUENT is the one by Smooke and Ern [24] including 16 species and 46 reactions. This mechanism has been presented in appendix A2.

There were big difficulties to simulate this case using FLUENT and the results do not show as good agreement as the ones obtained from the FASTEST-3D simulation when compared with the literature [3]. For the simulation with FLUENT a 2D axisymmetric solver has been chosen instead of the 3D grid used in the simulation with FASTEST-3D.

Even though the qualitative comparison of the results reveals little coincidence between

[3]The boundary conditions for temperature and species concentration apply only to reverse flow

both simulations, the order of magnitude of species, velocity and temperature is very similar.

The temperature peak differs only in approximately 180K (see fig. 4.20). 2000K in the case of FASTEST-3D, 2180K FLUENT and 2100K in the literature. In the case of CO_2 and H_2O (see fig. 4.22 and 4.23) the highest values are almost equal and in the same order of magnitude as the ones predicted by R. Baron [3]. In the case of CH_2O, the maximum value predicted by FASTEST-3D lies around 0.001 while FLUENT shows a value of 0.0039 which is almost four times higher, in the literature we see a value of 0.002 that does not exactly match the previous results but is in the same order of magnitude.

This geometry was simulated in FASTEST-3D using a constant density value for the mixture. Any attempt of density variation would lead to instabilities and to the extinction of the flame.

Because of the successful simulation of a H_2 flame with variable density presented in the next section, one can think that it is the reduced mechanism what leads to difficulties when trying to converge the case using FLUENT or FASTEST-3D with variable density. The use of a different mechanism to solve this configuration remains an objective for future work.

Figure 4.18 compares the results from FLUENT, FASTEST-3D, and those from the literature [3] for the temperature profile along the symmetry axis. It can be seen how all curves show the same behaviour and the temperature peaks are also at a similar level. FLUENT again shows the latest ignition of all ($5mm$ downstream the nozzle) and the highest temperature peak. The FASTEST-3D curve is similar but ignition happens earlier ($1mm$ downstream the nozzle) and the peak temperature is the lowest ($1900K$).

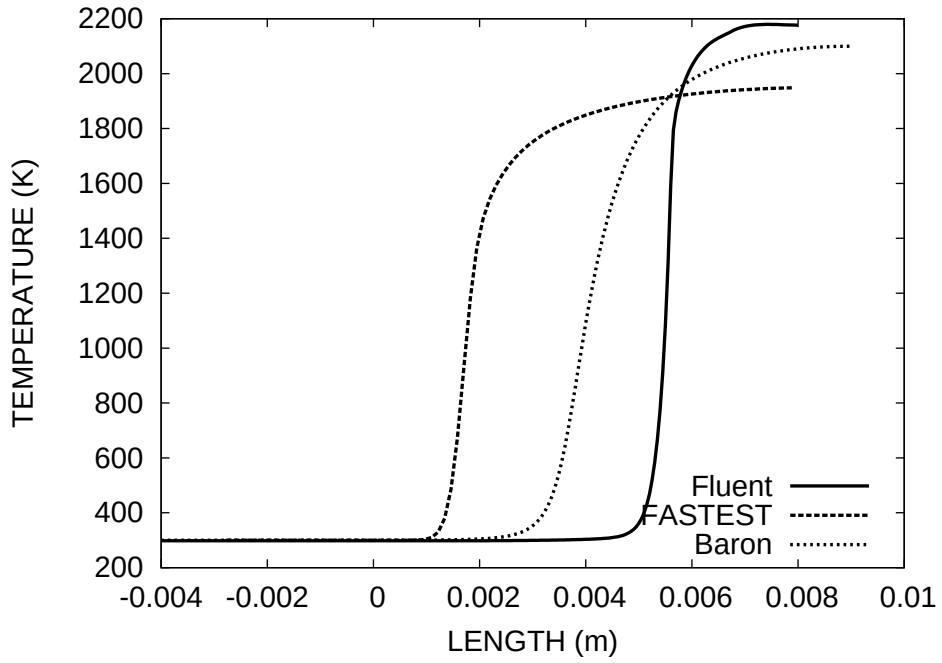

Figure 4.18.: Methane burner configuration. Temperature plots along the axis for FLUENT, FASTEST-3D and literature simulations

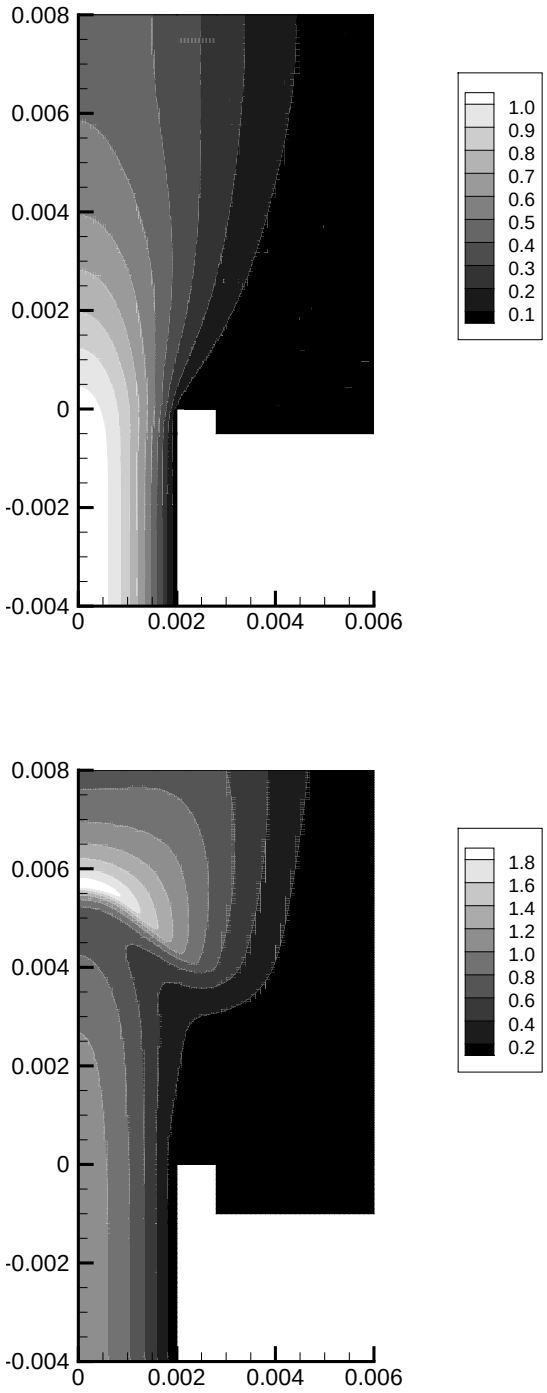

Figure 4.19.: Cold wall configuration for $CH_4 - air$ combustion.
Velocity fields provided by FASTEST-3D at the top and FLUENT at the bottom

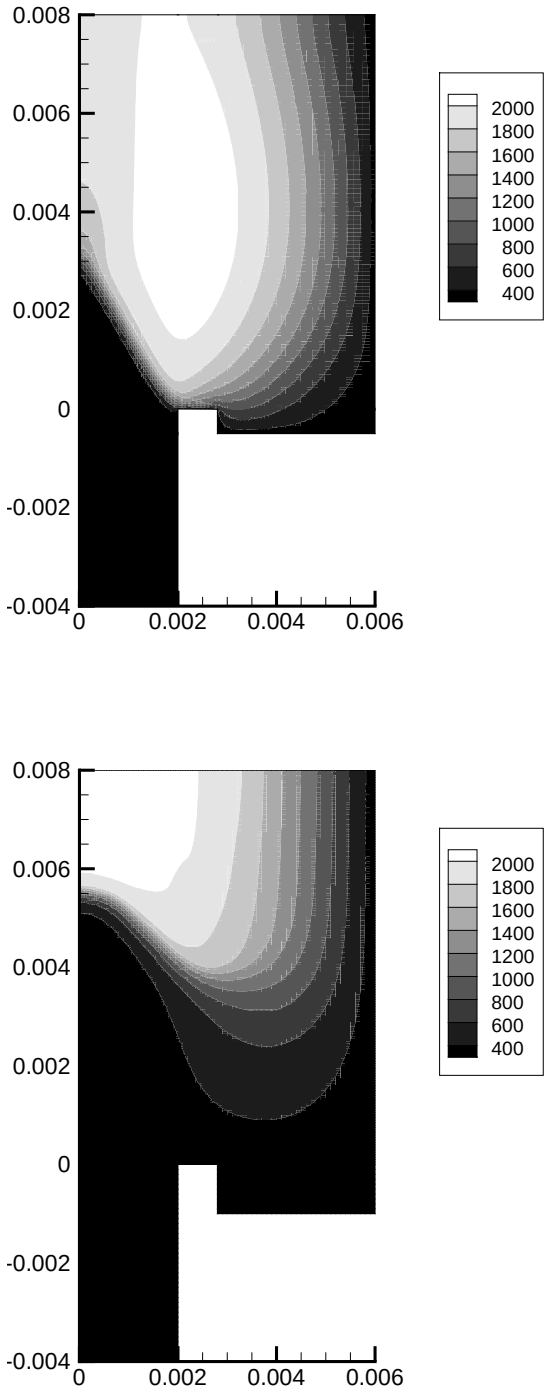

Figure 4.20.: Cold wall configuration for $CH_4 - air$ combustion.
Temperature fields provided by FASTEST-3D at the top and FLUENT at the bottom

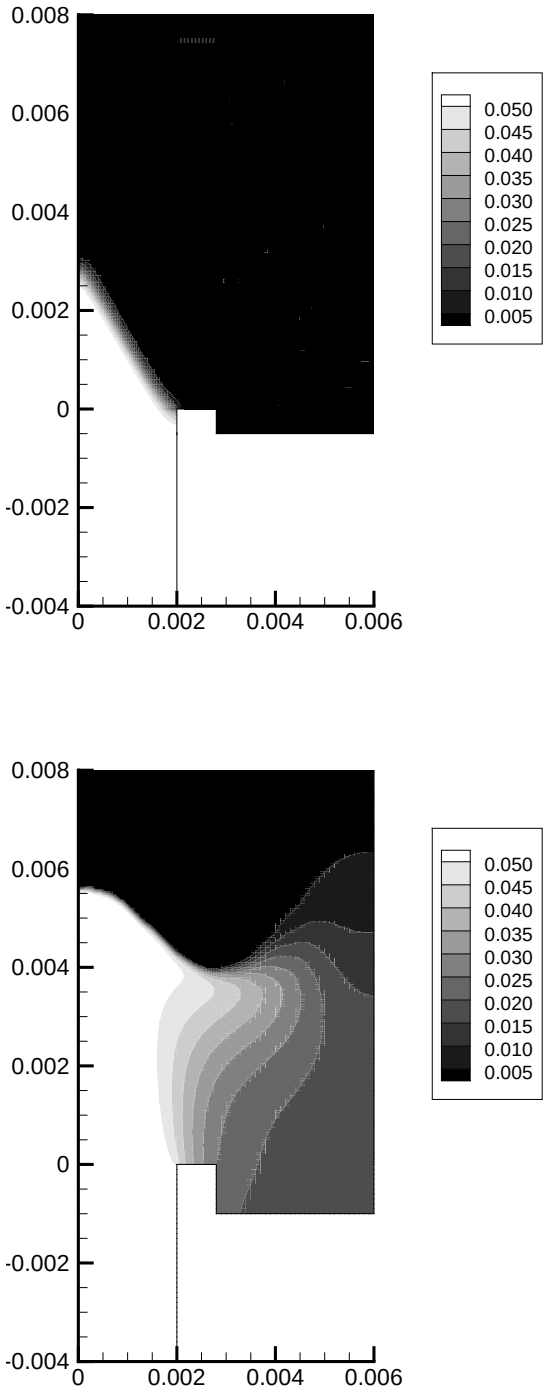

Figure 4.21.: Cold wall configuration for $CH_4 - air$ combustion.
CH_4 mass fraction fields provided by FASTEST-3D at the top and FLUENT at the bottom

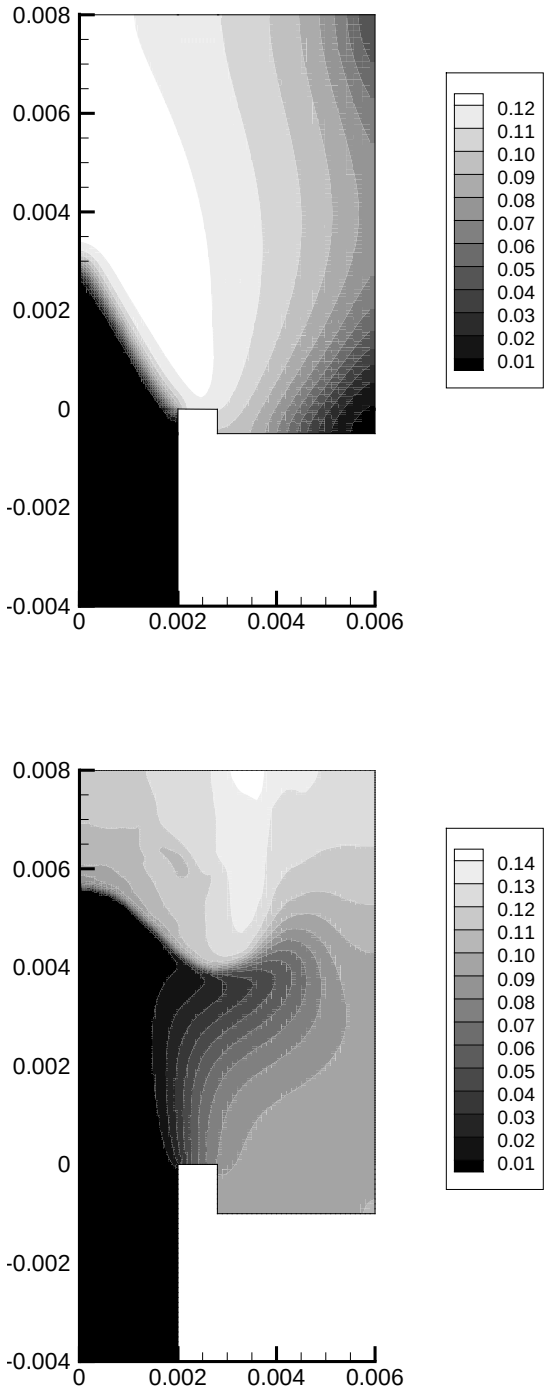

Figure 4.22.: Cold wall configuration for $CH_4 - air$ combustion.
CO_2 mass fraction fields provided by FASTEST-3D at the top and FLUENT at the bottom

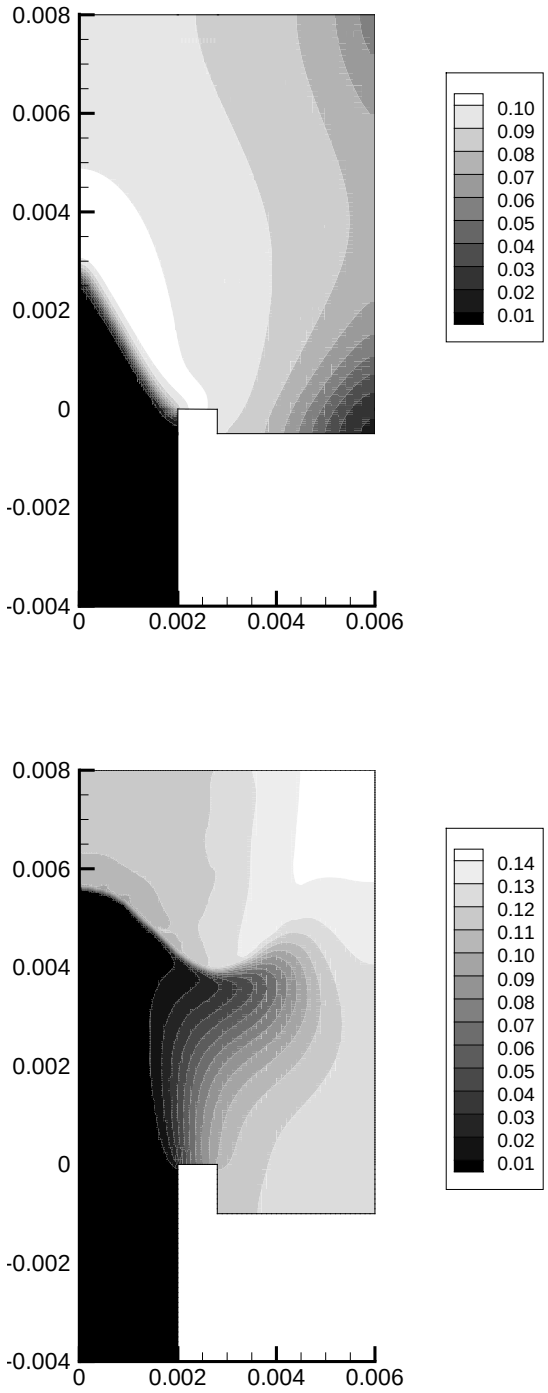

Figure 4.23.: Cold wall configuration for $CH_4 - air$ combustion.
H_2O mass fraction fields provided by FASTEST-3D at the top and FLUENT at the bottom

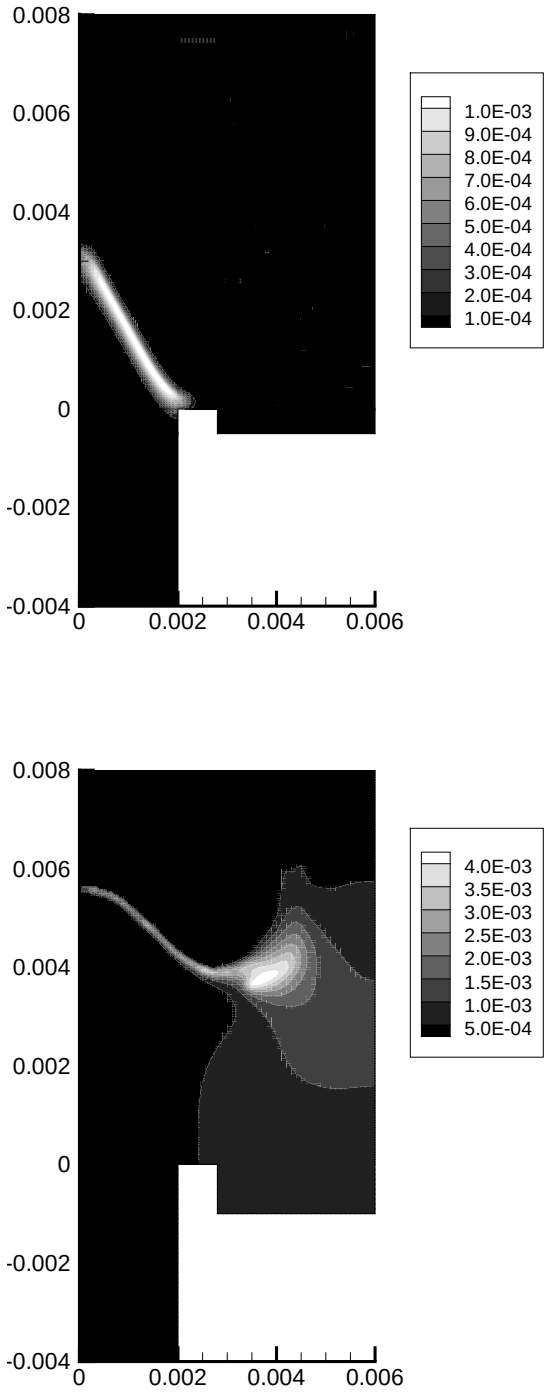

Figure 4.24.: Cold wall configuration for $CH_4 - air$ combustion.
CH_2O mass fraction fields provided by FASTEST-3D at the top and FLUENT at the bottom

4.3. Flames with variable density

4.3.1. EKT Standard Burner

The last configuration which has been included in the present work is the standard burner located in the TU-Darmstadt—EKT laboratories.

This simulation has been performed to show the capability of the coupling FASTEST-3D / CHEMKIN to simulate laminar flames with variable properties (density, viscosity and diffusion).

4.3.1.1. Configuration under study

The geometrical parameters can be seen in figure 4.25. For this simulation the grid consists of one orthogonal block with 50x100 grid points, a nozzle where a mixture of hydrogen and air comes into the burner with a velocity equal to 1m/s (Re=500) and a coflow of air flowing at 0.2m/s.

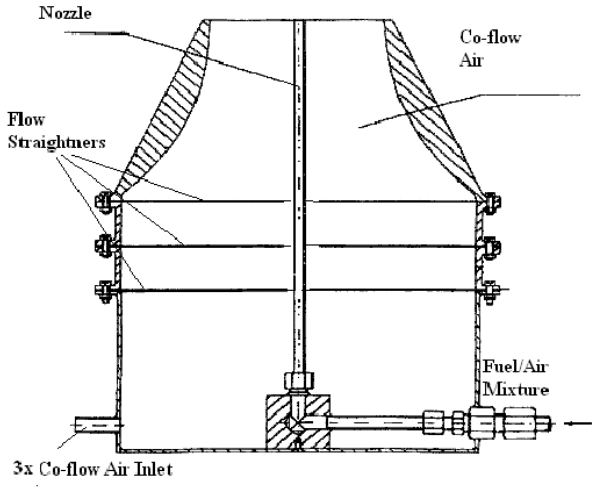

Figure 4.25.: Configuration of the EKT Standard Burner

Like in the previous cases for hydrogen combustion, the chemical scheme used is the 9 species 18 reactions mechanism from Miller et al. (see appendix A1).

Table 4.4.: Boundary Conditions for the EKT Standard Burner simulation

λ	Re	$\dot{q_{air}}$	$\dot{q}_{fuel}$	$\dot{q}_{coflow}$
4.8	500	221 l/m	19.3 l/m	4800 l/m

These values correspond to mass fractions of 0.027 for H_2, 0.216 for O_2 and 0.756 for N_2 at the nozzle. The inlet temperature of the gas is equal to $300K$.

4.3.1.2. Simulation results

The results can be seen in figures 4.26 to 4.32. Again the FASTEST-3D simulation results are at the top of the page while the FLUENT simulation results lie at the bottom. The symmetry axis is located at the left hand side of the picture in both cases.

The agreement between FASTEST-3D and FLUENT is in this case better than in any of the other configurations. The species concentrations lie in the same order of magnitude and the temperature peak difference is less than 100K.

FLUENT shows a higher amount of some intermediate species like H_2O_2 (see fig. 4.32), which may be due to the highest maximum temperature calculated by this code, but also to the inaccuracy of both CFD codes when solving very high gradients in the flame front where the resolution of the grid is very poor.

In the case of H_2O (fig. 4.31) both programs yield a very similar mass fraction distribution. FASTEST-3D gives a peak mass fraction of 0.222 against the 0.241 given by FLUENT, showing very good agreement between both codes. FASTEST-3D predicts a higher diffusion along the burner as well as a higher H_2O production rate at the exit of the nozzle. This can be due to the effect mentioned in section 3.1, that reactions start earlier when grids are too coarse. Both effects, the differences in species distributions on the one hand and the higher reaction rates calculated by FASTEST-3D) on the other have been seen previously in the simulation of the H_2-Bunsen burner (section 4.1.2).

Again in this case, the different species diffusion in both simulations is due to the different diffusion coefficients used by FLUENT and FASTEST. The higher reaction rates in the FASTEST-3D simulation can be due to the splitting errors when using a very coarse grid, as seen in section 3.1. This latter effect can also be seen in the reactants profiles (fig. 4.29 and 4.30), where the concentrations decrease faster after the nozzle because of the higher reaction rates.

A finer grid would certainly serve to improve the results given by both programs but the computational cost, especially in the case of FASTEST-3D, would be too high at the present moment.

Figure 4.26 shows a comparison of the results from FLUENT and FASTEST for the temperature profile along the symmetry axis. Both curves show the same behaviour and the temperature peaks are very close. The ignition takes place very soon after the nozzle, but the coarse grid does not allow a better definition of the ignition process.

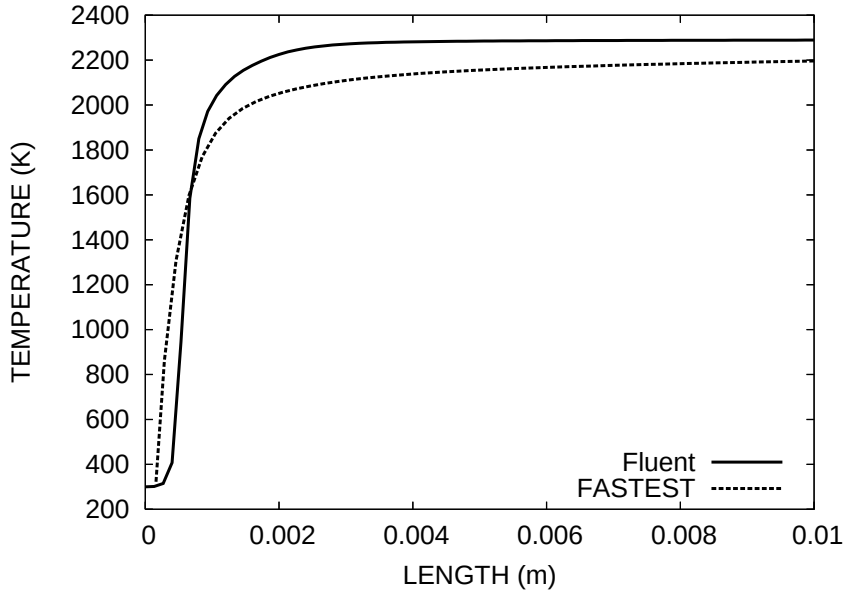

Figure 4.26.: EKT standard burner configuration. Temperature plots along the axis for FLUENT and FASTEST

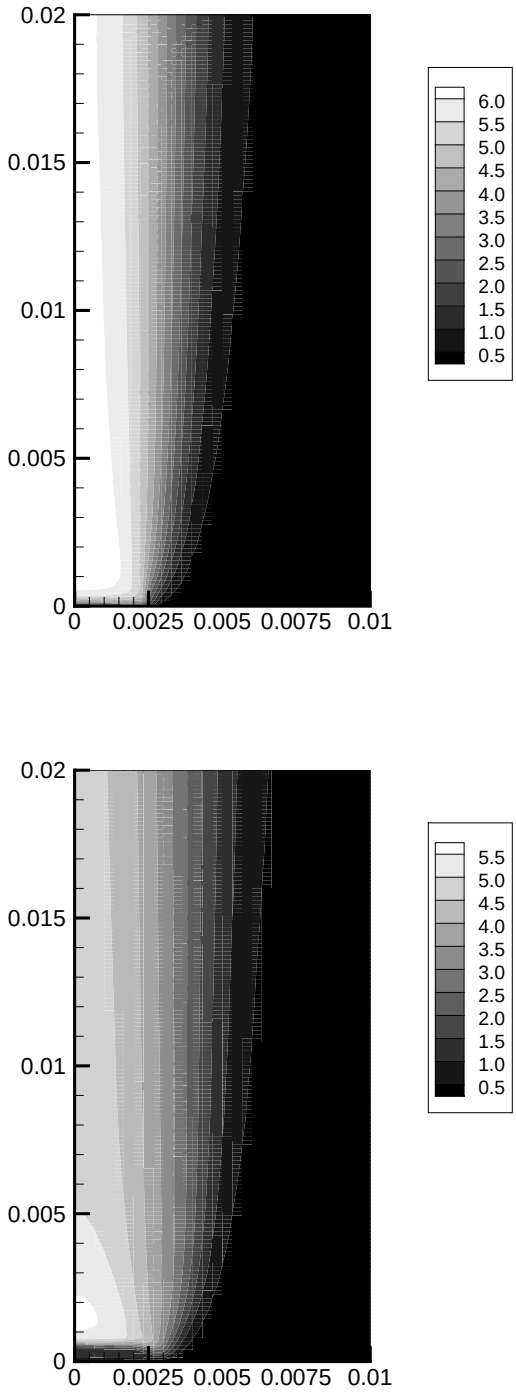

Figure 4.27.: EKT Standard Burner
Velocity fields provided by FASTEST-3D at the top and FLUENT at the bottom

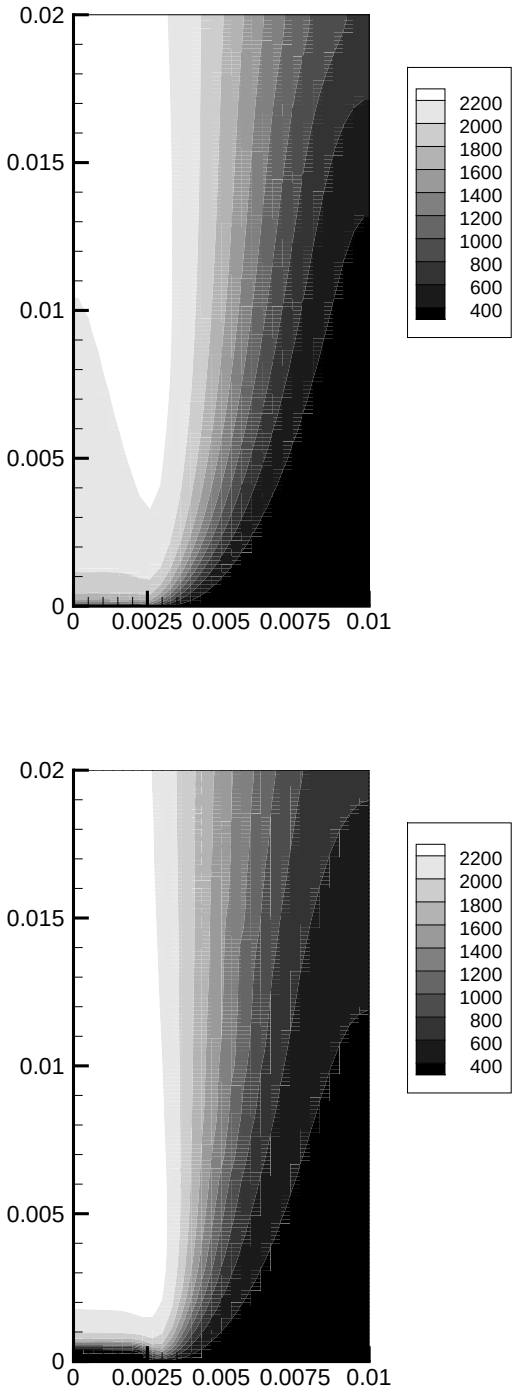

Figure 4.28.: EKT Standard Burner
Temperature fields provided by FASTEST-3D at the top and FLUENT at the bottom

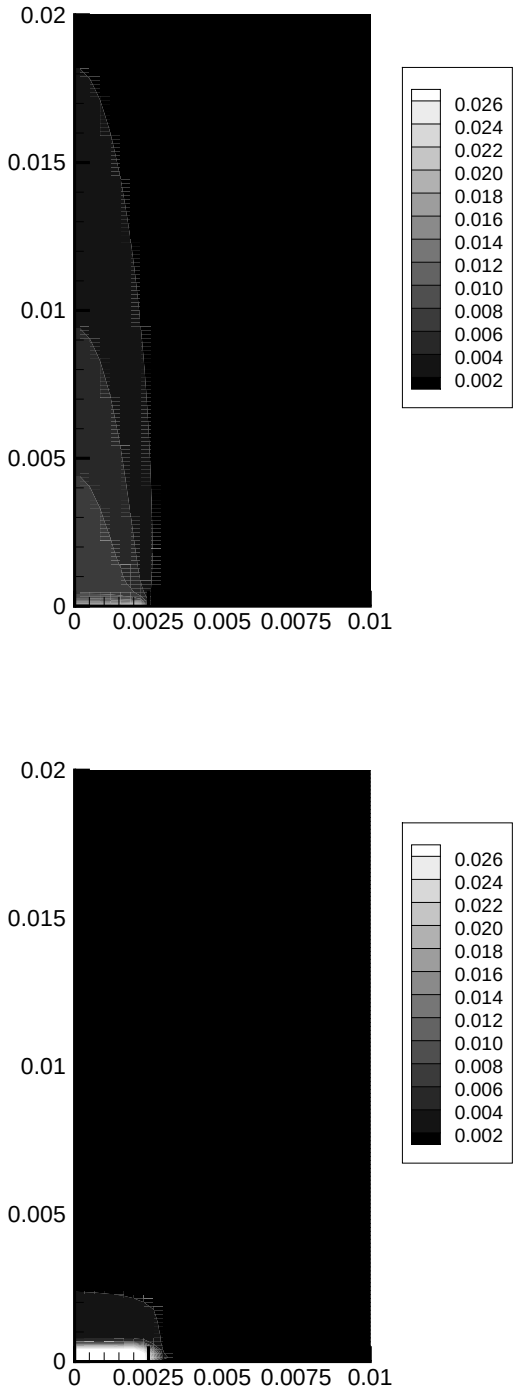

Figure 4.29.: EKT Standard Burner
H_2 mass fraction fields provided by FASTEST-3D at the top and FLUENT at the bottom

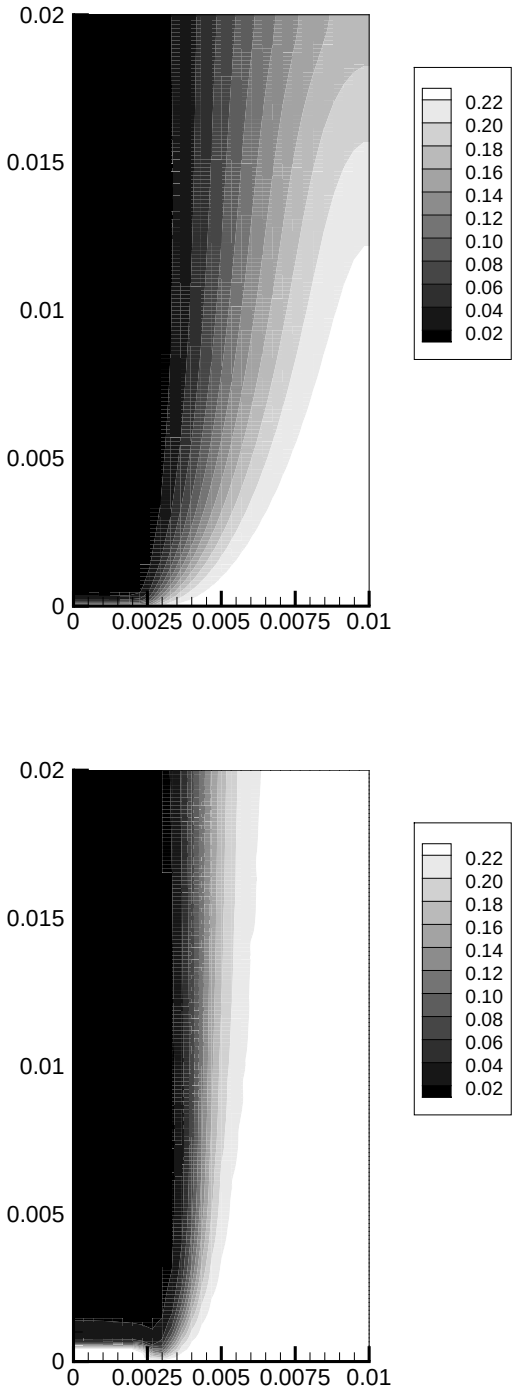

Figure 4.30.: EKT Standard Burner
O_2 mass fraction fields provided by FASTEST-3D at the top and FLUENT at the bottom

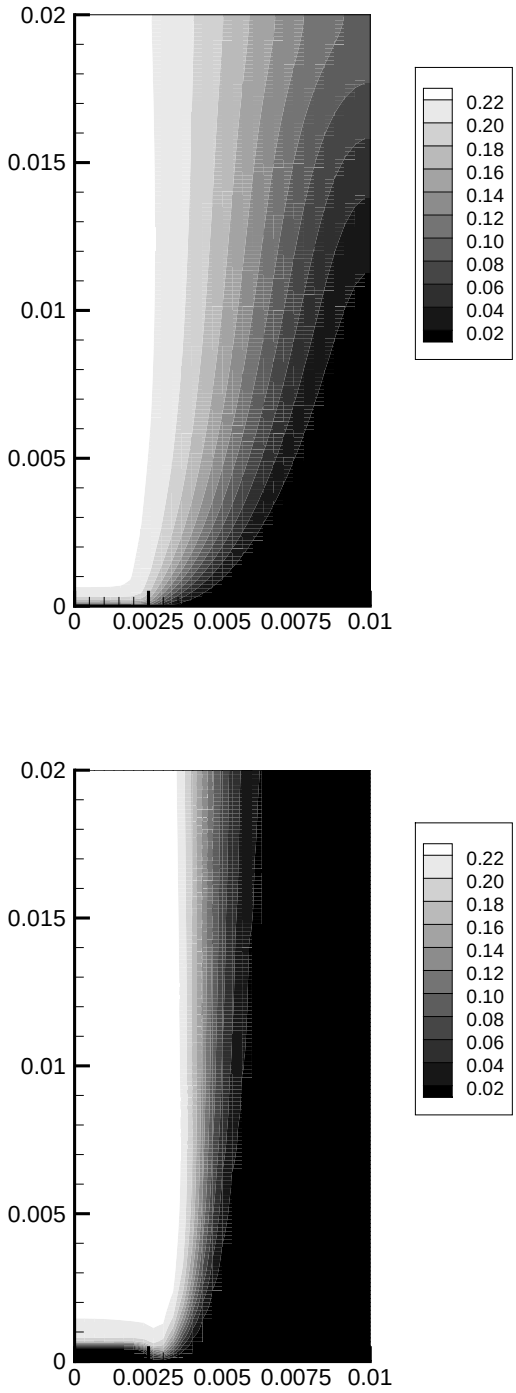

Figure 4.31.: EKT Standard Burner
H_2O mass fraction fields provided by FASTEST-3D at the top and FLUENT at the bottom

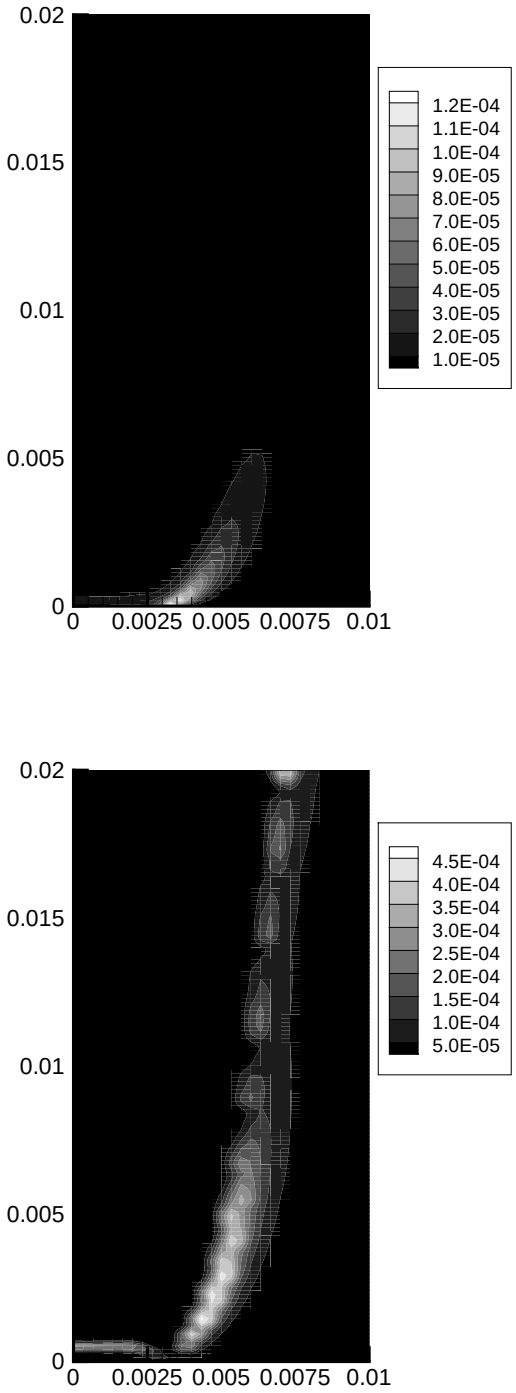

Figure 4.32.: EKT Standard Burner
H_2O_2 mass fraction fields provided by FASTEST-3D at the top and FLUENT at the bottom

5. Conclusions and Perspective

The aim of this thesis is the simulation of reacting flows with detailed chemistry under laminar conditions. This has been achieved through the coupling of an academic CFD-code (FASTEST-3D) and a chemical kinetics solver (CHEMKIN) through a Strang-like operator-splitting algorithm. For the transport of species, Fick's law has been used with temperature dependent polynomial for each species diffusion coefficient.

Several 3D simulations of 1D configurations have been performed for the cases of methane and hydrogen combustion in order to verify the implementation with a 0D-calculation code (SENKIN). Various parametrical analysis have been performed in order to study the influence of the *CFL* number, grid spacing and time discretization on the final results.

Two approaches have been tried in order to select the most accurate scheme for the operator splitting method. The steady one proposed by authors like Coehlo, Consul and Claramunt ([13], [15], [12]) has been compared with the unsteady strategy proposed by Bell or Holm-Christensen [19], [36] showing the latter better agreement with the 0D results provided by the SENKIN package. The 2D simulations have been performed using the unsteady approach with CFL numbers close to one in all cases and a Crank-Nicolson implicit scheme for the unsteady terms, which showed better accuracy than the second order scheme. The problems that arise with the introduction of variations of the density have been partially overcome through the underrelaxation of density.

Several practical configurations have been simulated using FASTEST-3D and FLUENT in order to verify the implementation. However, the fact that FLUENT solves 2D-axisymmetric equations while FASTEST-3D solves 3D cartesian equations on one side, and the use of constant density for most FASTEST-3D calculations on the other are sources of deviation that cannot be neglected. Both programs show better or worse agreement with the literature data depending on the case. The example in section 4.3.1, where density variations are allowed in both simulations, shows very good agreement between the two programs.

It is clear through the visualization of the figures that the coupling performed between FASTEST-3D and CHEMKIN correctly reproduces the effects observed in the experiments and calculates the species concentrations with acceptable accuracy. Another advantage of the implemented method is that no detailed knowledge of the chemical processes involved is needed by the user, only the chemical mechanism must be read into CHEMKIN and the boundary and initial conditions have to be set properly.

There is no reference in this report to the computational cost of the simulations performed

with the commercial code FLUENT and with FASTEST-3D. They differ by some orders of magnitude and cannot be compared. In the case of FLUENT, the simulations took from one to three days while for FASTEST-3D each simulation had to run for several weeks. In the case of the simulation of the EKT standard burner (section 4.3.1), with variable density, the program ran continuously during six weeks. The grids that have been used in both programs consist of similar number of computational nodes and the computers have quite the same characteristics:

- PC Athlon 3GHz for the simulations performed with FASTEST-3D
- PC Pentium 4 3GHz for FLUENT

Other disadvantages of the implementation are the restrictions inherent to the code FASTEST-3D. For example, the fact that the code does not allow the use of unstructured or 2D grids, which better represent the real configuration of the laminar flames under study and can help reduce the computational cost of the calculations.

The implemented algorithm allows the calculation of diffusion and premixed flames under fully premixed or partially premixed fuel-oxidizer conditions. In the case of diffusion flames only the simulation presented in section 4.1.1 has been performed. The difficulty in this case is higher because the flame is longer than in the premixed case and the size of the computational domain introduces a very high computational cost. FASTEST-3D was not able to give satisfactory results for this configuration. This shows that micro-combustion simulation requires of more advanced numerical methods as well as more accurate and robust chemical treatment than the splitting scheme used in this work.

In the case of the H_2 Bunsen-burner presented in section 4.1.2 and the cold wall stabilized methane burner shown in section 4.2.1 the simulations reproduce with good accuracy the chemical reactions that transform reactants into products and produce a temperature increment. The figures show small differences of the results in comparison to other authors [23]. From comparison of the bibliographical results with the ones given by FLUENT and FASTEST-3D it can be observed that the latter provides more realistic species and temperature profiles than FLUENT in the second configuration (see [86], [3]), while in the case of the Bunsen-burner both codes show very similar species profiles and temperature distribution along the reactor.

The results of the EKT-standard burner simulation have been presented in section 4.3.1. Velocity, temperature and species concentration in the flame can be seen in figures 4.26 to 4.32, where a comparison between the coupling FASTEST-3D/CHEMKIN and FLUENT has been done. Both simulations are qualitatively very similar and the differences of the maximum values of species concentrations and their spacial distribution are small. The temperature field is also similar and the maximum value in both simulations differs in less than $100K$. Features like acceleration of the flow inside the flame due to density changes, radicals

formation and destruction or the diffusion of the flame in radial direction are reproduced in similar way by both simulations.

Perspective

The main problem of flame simulation using splitting techniques is the long time required by CFD-codes to reach a final solution, the accuracy of the results and the robustness of the solution process.

In the first case, the stability of the code when facing density variations of many orders of magnitude in very few cells is mandatory, not only to save computational time but also to be able to reach a final solution. Another way of accelerating the computation which has been frequently used in the literature is the parallelization of the computation ([15], [19], [68], [63], [24]), which would strongly reduce the time required to reach a converged solution.

For the fully detailed simulation of laminar flames, a detailed treatment of the transport equations is required. This detailed treatment makes it necessary to solve an equation for the diffusion velocity. This introduces another set of equations that must be solved in each control volume for each time step and thus, increased computational cost. The model can be more accurate by including the Soret and Dufour effects in the transport model and the energy equation. As explained in section 2.3 these effects have been neglected in the simulations presented in this work and Fick's law has been used instead.

For the simulation of chemical reactions in micro-environments (micro combustion) a certain treatment of the reactions on walls must take place. In our case, CHEMKIN II is not in the position to provide information about surface reactions. In order to incorporate these reactions in our simulations, CHEMKIN III must be coupled with the CFD-code and this kind of information exchange between the chemistry package and FASTEST must be implemented.

No additional reaction mechanisms have been used in this project in order to include pollutants like NO_X in the simulations. In future simulations other mechanisms should be used where pollutants are included. This introduces new species in the simulation, whose generation, formation and distribution along the burner can be later obtained at the post-processing. The only drawback is the dramatic increment of the computational cost that arises with the introduction of additional species. It is also important to point out that the accuracy of any reduced reaction model is limited by the accuracy of the detailed reaction mechanism. Another option to obtain information about the pollutant generation is using a post-processing method ([97], [21]) in which the NO_X chemistry is separated from the actual flame computation.

To improve the robustness of the code one can, for example, provide an accurate initial field for a detailed chemistry computation. This could be achieved by means of other CFD

packages or even 1D computations depending on the case.

A. Reaction mechanisms

A.1. H_2 Combustion Mechanism

The reaction mechanism used in this work for hydrogen combustion is the one from Kee et al. [46] and consists of 8 species plus N_2 and 18 reactions (the species and reactions involved in NO_X formation have been eliminated from the original mechanism). The species present in the chemical mechanism can be seen in table A.1 together with their molar mass in SI units.

Table A.1.: Species involved in the reaction mechanism of H_2-combustion together with their molar mass

Species	$M_i[Kg/Kmol]$
H_2	2.02
O_2	32.00
HO_2	33.01
H_2O	18.02
OH	17.01
H	1.01
O	16.00
H_2O_2	34.01
N_2	28.01

The chemical reactions are presented in table A.2 for hydrogen and A.4 for methane combustion. In both tables A, β and E_a represent the pre-exponential factor, the temperature exponent and the activation energy as shown by the Arrhenius equation (2.22).

Table A.2.: Reactions and rate parameters for the H_2-mechanism. Units are mole, cm, s and K.

	Reaction	A	β	R_a
1	H+O2+M=HO2+M	3.61×10^{17}	-0.70	0
	H2O/18.6/ H2/2.86/			
2	H+H+M=H2+M	1.00×10^{18}	-1.0	0
3	H+H+H2=H2+H2	9.20×10^{16}	-0.6	0
4	H+H+H2O=H2+H2O	6.00×10^{19}	-1.25	0
5	H+OH+M=H2O+M	1.60×10^{22}	-2.0	0
	H2O/5/			
6	H+O+M=OH+M	6.20×10^{16}	-0.6	0
	H2O/5/			
7	O+O+M=O2+M	1.89×10^{13}	0.0	-1788
8	H2O2+M=OH+OH+M	1.30×10^{17}	0.0	45500
9	H2+O2=2OH	1.70×10^{13}	0.0	47780
10	OH+H2=H2O+H	1.17×10^{9}	1.3	3626
11	O+OH=O2+H	3.61×10^{14}	-0.5	0
12	O+H2=OH+H	5.04×10^{4}	2.67	6290
13	OH+HO2=H2O+O2	7.50×10^{12}	0.0	0
14	H+HO2=2OH	1.40×10^{14}	0.0	1073
15	O+HO2=O2+OH	1.40×10^{13}	0.0	1073
16	2OH=O+H2O	6.00×10^{8}	1.3	0
17	H+HO2=H2+O2	1.25×10^{13}	0.0	0
18	HO2+HO2=H2O2+O2	2.00×10^{12}	0.0	0

A.2. CH_4 Combustion Mechanism

In the case of methane combustion the mechanism that has been used corresponds to a 46 reactions mechanism by M.D. Smooke and A. Ern [24] including 15 species plus N_2. The species involved in this mechanism are the ones presented previously for the H_2 mechanism plus the species including carbon. In table A.3 these species can be seen together with their molar masses.

Table A.3.: Species involved in the reaction mechanism of CH_4- combustion together with their molar mass

Species	$M_i[Kg/Kmol]$
CH_4	16.04
CH_2O	30.03
HCO	29.02
CO_2	44.01
CH_3	15.03
CH_3O	31.03
CO	28.01

In both cases units are mole, cm, s and K according to the conventions used in standard literature on combustion.

In some reactions a third molecule is involved which does not react, this is called "third body". The concentration of this third molecule is given by

$$[M] = \sum_{k}^{N_s} \xi_k [M_k] \tag{A.1}$$

where ξ_i are the collision or third body efficiencies. They appear described for each of the species involved as third bodies, below the corresponding reaction.

Table A.4.: Reactions and rate parameters for the CH_4-combustion mechanism

	Reaction	A	β	E_a
1	CH3+H=CH4	1.90×10^{36}	-7.00	9050
2	CH4+O2=CH3+HO2	7.90×10^{13}	0.00	56000
3	CH4+H=CH3+H2	2.20×10^{4}	3.00	8750
4	CH4+O=CH3+OH	1.60×10^{6}	2.36	7400
5	CH4+OH=CH3+H2O	1.60×10^{6}	2.10	2460
6	CH2O+OH=HCO+H2O	7.53×10^{12}	0.00	167
7	CH2O+H=HCO+H2	3.31×10^{14}	0.00	10500
8	CH2O+M=HCO+H+M	3.31×10^{16}	0.00	81000
9	CH2O+O=HCO+OH	1.81×10^{13}	0.00	3082
10	HCO+OH=CO+H2O	5.00×10^{12}	0.00	0
11	HCO+M=H+CO+M	1.60×10^{14}	0.00	14700
12	HCO+H=CO+H2	4.00×10^{13}	0.00	0
13	HCO+O=OH+CO	1.00×10^{13}	0.00	0
14	HCO+O2=HO2+CO	3.00×10^{12}	0.00	0
15	CO+O+M=CO2+M	3.20×10^{13}	0.00	-4200
16	CO+OH=CO2+H	1.51×10^{7}	1.30	-758
17	CO+O2=CO2+O	1.60×10^{13}	0.00	41000
18	CH3+O2=CH3O+O	7.00×10^{12}	0.00	25652
19	CH3O+M=CH2O+H+M	2.40×10^{13}	0.00	28812
20	CH3O+H=CH2O+H2	2.00×10^{13}	0.00	0
21	CH3O+OH=CH2O+H2O	1.00×10^{13}	0.00	0
22	CH3O+O=CH2O+OH	1.00×10^{13}	0.00	0
23	CH3O+O2=CH2O+HO2	6.30×10^{10}	0.00	2600
24	CH3+O2=CH2O+OH	5.20×10^{13}	0.00	34574
25	CH3+O=CH2O+H	6.80×10^{13}	0.00	0
26	CH3+OH=CH2O+H2	7.50×10^{12}	0.00	0
27	HO2+CO=CO2+OH	5.80×10^{13}	0.00	22934
28	H2+O2=2OH	1.70×10^{13}	0.00	47780
29	OH+H2=H2O+H	1.17×10^{9}	1.30	3626

	Reaction	A	β	E_a
30	H+O2=OH+O	2.00×10^{14}	0.00	16800
31	O+H2=OH+H	1.80×10^{10}	1.00	8826
32	H+O2+M=HO2+M	2.10×10^{18}	-1.00	0
	H2O/21/ CO2/5/ H2/3.3/ CO/2/ N2/0/ O2/0/			
33	H+O2+O2=HO2+O2	6.70×10^{19}	-1.42	0
34	H+O2+N2=HO2+N2	6.70×10^{19}	-1.42	0
35	OH+HO2=H2O+O2	5.00×10^{13}	0.00	1000
36	H+HO2=2OH	2.50×10^{14}	0.00	1900
37	O+HO2=O2+OH	4.80×10^{13}	0.00	1000
38	2OH=O+H2O	6.00×10^{8}	1.30	0
39	H2+M=H+H+M	2.23×10^{12}	0.50	92600
	H2O/6/ H/2/ H2/3/			
40	O2+M=O+O+M	1.85×10^{11}	0.50	95560
41	H+OH+M=H2O+M	7.50×10^{23}	-2.60	0
42	H+HO2=H2+O2	2.50×10^{13}	0.00	700
43	HO2+HO2=H2O2+O2	2.00×10^{12}	0.00	0
44	H2O2+M=OH+OH+M	1.30×10^{17}	0.00	45500
45	H2O2+H=HO2 + H2	1.60×10^{12}	0.00	3800
46	H2O2+OH=H2O+HO2	1.00×10^{13}	0.00	1800

Bibliography

[1] American Gas Association *http://www.aga.org/*

[2] Barlow R.S., Karpetis A.N. and Frank J.H. *Scalar profiles and NO formation in Laminar Opposed-Flow Partially Premixed Methane/Air Flames* Combust. Flame, 2001

[3] Baron R. *Calcul et optimisation de brûleurs industriels*, Ph.D. Thesis, Ecole Centrale Paris, 2002

[4] Batchelor G.K. *An Introduction to Fluid Dynamics*, University Press Cambridge, 2000

[5] Bell J., Colella P., and Howell L., *An efficient second-order projection method for viscous incompressible flow*, 10th AIAA CFD Conference, 1991.

[6] Bennett B.A., McEnally C.S., et al. *Computational and experimental study of axissymmetric co-flow partially premixed methane/air flames.* Comb. and Flame, 2000.

[7] Bennett B.A., McEnally C.S. et al. *Local rectangular refinement with application to axisymmetric laminar flames.* Combustion Theory and Modelling, 1998.

[8] Bird R.B., Stewart W.E. and Lightfoodt E. *Transport Phenomena.* Wiley-VCH, 2001

[9] Borup R.L., Davey J.R. et al.*PEM fuel cell electrocatalyst durability measurements*, Journal of power sources, 2006, vol. 163

[10] Caracotsios M. and Stewart W.E. *Sensitivity analysis on initial value problems with mixed ODEs and algebraic equations.* Comput. Chem. Eng. 9(4), 1985

[11] Caracotsios M. and Stewart W.E. *Sensitivity analysis on initial-boundary value problems with mixed PDEs and algebraic equations.* Comput. Chem. Eng. 19(9), 1995

[12] Claramunt K., R. Cónsul et al. *Multidimensional mathematical modeling and numerical investigation of co-flow partially premixed methane/air laminar flames*, Combust. and Flame, 2004.

[13] Coelho P.J. and Pereira J.C.F. *Calculation of a Confined Axisymmetric Laminar Diffusion Flame Using a Local Grid Refinement Technique*, Combust. Sci. and Tech., 1993

[14] Contreras J. Sadiki, A. and Janicka, J. *Towards 3D Simulation of Gas Phase Reactions involved in the Deposition of* $\alpha - Al_2O_3$, CVD XVI and EUROCVD 14 Meeting, 2003

[15] Consul R. Perez-Segarra et al. *Detailed numerical simulation of laminar flames by a parallel multiblock algorithm using loosely coupled computers*, Combust. Theory Modelling, 2003

[16] Csomós P. and Faragó I. *Error analysis of the numerical solution of split differential equations*, Submited to Elsevier Science, 2006

[17] Davidson L. *Numerical Methods for Turbulent Flow*, http://www.tfd.chalmers.se/gr-kurs/MTF071

[18] De Witt M.J., Dooling D.J. and Broadbelt L.J. *Computer generation of reaction mechanisms using quantitative rate information.* Ind. & Chem. Research 39, 2000

[19] Day M.S. and Bell J.B. *Numerical Simulation of Laminar Reacting Flows with Complex Chemistry*, Combust. Theory Modelling, 2000

[20] Durst F. and Schaefer M. *A Parallel Blockstructured Multigrid Method for the Prediction of Incompressible Flow.* Int. J. Numer. Methods in Fluids, 1996

[21] Eggels R.L.G.M. *Modeling of Combustion Processes and NO formation with Reduced Reaction Mechanisms,* Ph.D Thesis, Eindhoven University of Technology, 1996

[22] Ern A. and Giovangigli V. *Multicomponent transport algorithms*, Lecture Notes in Physics, Vol.24, 1994

[23] Ern A. and Giovangigli V. *Thermal diffusion effects in hydrogen-air and methane air flames*, Combust. Theory Modelling, 1998

[24] Ern A., Douglas C.C. and Smooke M.D. *Detailed chemistry modeling of laminar diffusion flames on parallel computers*, Int. J. Supercomput. Appl., 1995

[25] *Fastest-3D Reference Guide*, 2004

[26] Glaude P.A. Battin-Leclerc F. et al. *Construction and simplification of a model for the oxidation of alkanes.* 2000

[27] Faragó I. and Havasi Á *On the convergence and local error of different splitting schemes*, Progress in CFD, 2005

[28] Ferziger J. and Perić M. *Computational Methods for Fluid Dynamics.* Springer, 1996

[29] Fleischer T. and Oertel D. *Fuel cells. Impact and consequences of fuel cells technology on sustainable development*, Institut für Technikfolgenabschätzung und Systemanalyse, ITAS, march 2003

[30] Geiser J. *Operator Splitting Methods I: Introduction and a flexible Iterative Solver*, 10th lecture: PDE: Error-Analysis, Doscretization and Solver Methods, 2006

[31] Ghilani M. and LARROUTUROU B. *Upwind computation of steady planar flames with complex chemistry*, Mod. Math. et Anal. Num., 1991

[32] Glaborg P., Kee R.J., Grcar J.F. and Miller J.A. *RSR: A FORTRAN Program for modeling Well-Stirred Reactors.* Sandia Rep. SAND 86-8209, 1986

[33] Heywood J.B. *Internal Combustion Engine Fundamentals* McGraw-Hill, 1988

[34] Hirschfelder J.O., Curtiss C.F. and Bird R.B. *The molecular theory of gases and liquids.* John Wiley & Sons, 1964

[35] Holden E. *Achieving Sustainable Mobility: Everyday and Leisure-time Travel in the EU.* Ashgate Publishing, Ltd., 2007

[36] Holm-Christensen and Jones I.P. *The solution of coupled flow and chemistry problems*, Progress in Computational Fluid Dynamics, 2001

[37] Hundsdorfer W. and Verwer J.G. *A note on splitting errors for advection-reaction equations*, Appl. Numer. Math, 1994

[38] Hunziker W. Graf G.M. *Computational Fluid Dynamics*, ETH Zürich, 1999

[39] Issa R.I. *The computation of compressible and incompressible recirculating flows by a non- iterative implicit scheme.* Journal of Computational Physics, 1986.

[40] Jacques D., Simunek J. et al. *Operator-splitting errors in coupled reactive transport codes for transient variably saturated flow and contaminant transport in layered soil profiles.* Journal of contaminant hydrology, 2006, vol. 88.

[41] Janicka J. and Kollmann W. *A two variables formalism for the treatment of chemical reactions of turbulent H_2-air diffusion flames*, 17th Symposium on Combustion, 1978

[42] Karlsen K.H., Lie K.A. et al. *Operator Splitting Methods for Systems of Convection-Diffustion Equations: Nonlinear Error Mechanisms and Correction Strategies*, J. Comp. Physics, 2001

[43] Karlsen K.H. and Risebro N.H. *Corrected operator splitting for nonlinear parabolic equations*, SIAM J. Numer. Anal., 2000

[44] Katta V.R and Roquemore W.M. *Simulation of dynamic methane jet difusion flames using finite rate chemistry models.* AIAA Journal, 1998.

[45] Katta V.R., Goss L.P., and Roquemore W.M. *Effect of nonunity lewis number and finite-rate chemistry on the dynamics of a hydrogen-air jet difusion flame.* Comb. and Flame, 1994.

[46] Kee R.J, Rupley F.M. et al. *Chemkin-II: A Fortran Chemical Kinetics Package for the Analysis of Gas-Phase Chemical Kinetics*, Sandia Report SAND89-8009

[47] Kee R.J., Rupley F.M. and Miller J.A. *The Chemkin Thermodynamic Data Base*, Sandia Report SAND87-8215

[48] LeVeque R.J. and Yee H.C. *A study of numerical methods for hyperbolic conservation laws with stiff source terms.* J. of Comput. Phys.,1990

[49] Lindstedt P. *Modelling the chemical complexities of flames*, Proc. Comb. Inst., 1998

[50] Lutz A.E., Kee R. et al. *SENKIN: A Fortran Program for Predicting Homogeneous Gas Phase Chemical Kinetics with Sensitivity Analysys*, Sandia National Laboratories, 1988

[51] Maas U. and Pope S.B. *Simplifying chemical kinetics: Intrinsic low-dimensional manifolds in composition space*, Combust. Flame, 1992

[52] Maas U. and Pope S.B. *Implementation of simplified chemical kinetics based on intrinsic low-dimensional manifolds,* Proc. Comb. Inst., 1992

[53] Marchuk G.I. *Methods of Splitting*, Nauka, Moscow, 1988

[54] Markov A.A. and Sadiki A. *The Splitting Technique in Numerical Simulation of Two-phase Reacting Flows in a Tube*, 5th World Congress on Computat. Mechanics, 2002

[55] Miller J.A. and Kee R. J. *Chemikal kinetics and combustion modeling*, Annu. Rev. Phys. Chem., 1990

[56] R.E. Mitchell, Sarofim, and L.A. Clomburg. *Experimental and numerical investigation of confined laminar difusion flames.* Comb. and Flame, 1980.

[57] Najm H.N., Knio O.M., et al. *Operator-Splitting in Reacting Flow Modeling*, 18th ICDERS, 2001

[58] Najm H.N., Wyckoff P.S. and Knio O.M. *A Semi-implicit Numerical Scheme for Reacting Flow*, J. Computat. Physics, 1998

[59] Najm H.N., Wyckoff P.S. and Knio O.M. *A Semi-implicit Numerical Scheme for Reacting Flow. II Stiff reactions, operator splitting formulation*, J. Computat. Physics, 2000

[60] Nakamura Y., Kubota A. et al. *Numerical Study on Methane Micro-Diffusion Flamesel*, 19th ICDERS, 2003

[61] Nitodas F. and Sotirchos V. *Development and Validation of a Mathematical Model for the Chemical Vapour Deposition of Alumina from Mixtures of Aluminium Trichoride, Carbon Dioxide and Hydrogen*, J. Electrochem. Soc., 2002

[62] Nguyen Q.V., Dibble R.W. et al. *Raman-LIF measurements of temperature, major species, OH, and NO in a methane-air bunsen flame*, Comb. and Flame, 1996

[63] Northrup S.A. and Groth C.P.T. *Solution of Laminar Diusion Flames Using a Parallel Adaptive Mesh Renement Algorithm*, 43rd AIAA Aerospace Sciences Meeting and Exhibit, 2005

[64] Oran E.S. and Boris J.P. *Numerical Simulation of Reactive Flow*, Cambridge University Press, 2001

[65] Parmentier S, Braack M, et al. *Modeling of combustion in a lamella burner.* Combust. Sci. Tech., 2003

[66] Patankar S. V. *Numerical Heat Transfer and Fluid Flow.* Hemisphere Publishing Corporation, 1980

[67] Patankar S. V. and Spalding D.B. *A calculation procedure for heat, mass and momentum transfer in three-dimensional parabolic flows.* International Journal of Heat and Mass Transfer,1972.

[68] Paxion S., Baron R. et al. *Development of a Parallel Unstructured Multigrid Solver for Laminar Flame Simulations with Detailed Chemistry and Transport*, Notes on Numerical Fluid Mechanics, 2001

[69] Peaceman D.W., Rachford H.H., *The numerical solution of parabolic and elliptic differential equations*, J. Soc. Indust. Appl. Math. 3 (1), 1955

[70] Pember R.B., Howell L.H. et al. *An adaptative projection method for unsteady, low-Mach number combustion.* Combust. Schi. and Tech., 1998

[71] Perić M. *A Finite Volume Method for the Prediction of Three-Dimensional Fluid Flow in Complex Ducts.* PhD thesis, Imperial College, 1985

[72] Peters N. *Turbulent combustion.* Cambridge University Press, 2000

[73] Peters N. and Williams F.A. *The asymptotic structure of stoichiometric methane-air flames,* Comb. and Flame, 1987

[74] Poinsot T. and Veynante D. *Theoretical and numerical combustion*, Edwards, 2001

[75] Pope S.B. *Computationally efficient implementation of combustion chemistry using in situ adaptive tabulation*, Combust. Theory Modelling, 1997

[76] Pucheng P., Wu Yanga and Ping Li. *Numerical prediction on an automotive fuel cell driving system*, International Journal of Hydrogen Energy, Volume 31, Issue 3, March 2006

[77] Rehm R.G. and Baum H.R. *The equations of motion for thermally driven buoyant flows.* N.B.S.J.Res. 83, 1978

[78] Reynolds W.C. *The element potential method for Chemical Equilibrium Analysis: Implementation in the interactive program STANJAN Version 3.* Dept of Mech. Eng., Stanford Univ., 1986

[79] Raithby G.D. and Schneider G.E. *Elliptic systems: Finite-difference method II*, Handbook of Numerical Heat Transfer, Wiley, 1988.

[80] Rhie C.M., Chow W.L. *A numerical study of the flow past an isolated airfoil with separation.* AIAA-82-0988, 1982

[81] Schwer D. A., Lu P., et al. *A consistent-splitting approach to computing stiff steady-state reacting flows with adaptive chemistry*, Combust. Theory Modelling, 2003

[82] Singer M.A. and Pope S.B. *Exploiting ISAT to Solve the Equations of Reacting Flow*, Comb. Theory Modelling, 2003.

[83] Smooke M.D., Lin P et al. *Computational and Experimental Study on a laminar Axisymmetric Methane-Air Diffusion Flame*, 23 Symposium on Combustion, 1990

[84] Smooke M.D., McEnally C.S., and L.D. Pfefferle. *Computational and experimental study of soot formation in a co-flow, laminar difusion flame.* Comb. and Flame, 1999.

[85] Smooke M.D., Xu Y. et al. *Computational and experimental study of OH and CH radicals in axisymmetric laminar difusion flame.* International Symposium on Combustion, 1992.

[86] Somers L.M.T. and De Goey L.P.H. *A numerical study of a premixed flame on a slit burner*, Combust. Sci. Tech., 1995

[87] Somers L.M.T., *The simulation of flat flames with detailed and reduced chemical models,* Ph.D. Thesis, Eindhoven University of Technology, 1994

[88] Somers L.M.T., *Modelling Approaches to Chemical and Transport Processes*, Eindhoven University of Technology, 2003

[89] Spurk J. *Strömungslehre*. Springer Verlag, 1996

[90] Stoer J. and Bulirsch R. *Introduction to Numerical Analysis*. Springer Verlag, 1980

[91] Strang G. *On the construction and comparison of difference schemes*, SIAM J. Num. Anal., 1968.

[92] Thiart G.D. *Improved finite-difference scheme for the solution of convection-diffusion problems with the SIMPLEN algorithm*, Num. Heat Transfer, 1990

[93] Trompert R.A. and Verwer J.G. *A static-regridding method for two-dimensional parabolic partial differential equations*, Applied Numerical Mathematics, 1991

[94] Van Doormaal J.P. and Raithby G.D. *Enhancement of the SIMPLE method for predicting incompressible fluid flows*. Numerical Heat Transfer, 1984.

[95] van Oijen J. *Flamelet-Generated Manifolds: Development and Application to Premixed Laminar Flames*, Ph.D. Thesis, Eindhoven University of Technology, 2002

[96] Veinante D. and Candel S. *Combustion et milieux réactifs*, Rapport scientifique - IDRIS, 20031

[97] Wachter E.M. *Anwendung der Instationären Flamelet-Methode auf Diffusionsflammen im Post-Processing-Modus*, Ph.D Thesis, TU-Darmstadt, 2005

[98] Warnatz J. Maas U. and Dibble R.W. *Verbrennung*, Vol.:2, Springer, 1997